DISSERTATIONES
CHIMICAE
UNIVERSITATIS
TARTUENSIS
232

KAAREL KISAND

Resorcinol-derived carbon-based catalysts for polymer electrolyte fuel cell cathodes

DISSERTATIONES CHIMICAE UNIVERSITATIS TARTUENSIS
232

DISSERTATIONES CHIMICAE UNIVERSITATIS TARTUENSIS
232

KAAREL KISAND

Resorcinol-derived carbon-based catalysts for polymer electrolyte fuel cell cathodes

UNIVERSITY OF TARTU
Press
1632

Institute of Chemistry, Faculty of Science and Technology, University of Tartu, Estonia

The dissertation is accepted for the commencement of the degree of *Doctor Philosophiae* in Chemistry on June 11th, 2024 by the Council of Institute of Chemistry, Faculty of Science and Technology, University of Tartu.

Supervisors: Associate professor Ave Sarapuu
Institute of Chemistry, University of Tartu, Estonia

Professor Kaido Tammeveski
Institute of Chemistry, University of Tartu, Estonia

Opponent: Dr. Justus Masa
Max Planck Institute for Chemical Energy Conversion, Germany

Commencement: 29 August 2024 at 12:15 Ravila 14A, Tartu (Chemicum)

This work has been partially supported by ASTRA project PER ASPERA Graduate School of Functional Materials and Technologies receiving funding from the European Regional Development Fund under project in University of Tartu, Estonia

ISSN 1406-0299 (print)
ISBN 978-9916-27-574-0 (print)
ISSN 2806-2159 (pdf)
ISBN 978-9916-27-575-7 (pdf)

University of Tartu Press
www.tyk.ee

TABLE OF CONTENTS

1. LIST OF ORIGINAL PUBLICATIONS

This thesis consists of six original articles listed below. The articles are referred to by Roman numerals I–VI.

[I] K. Kisand, A. Sarapuu, A.-L. Peikolainen, H. Seemen, M. Kook, M. Käärik, J. Leis, V. Sammelselg, K. Tammeveski, Oxygen reduction on Fe- and Co-containing nitrogen-doped nanocarbons, ChemElectroChem 5 (2018) 2002–2009.

[II] K. Kisand, A. Sarapuu, D. Danilian, A. Kikas, V. Kisand, M. Rähn, A. Treshchalov, M. Käärik, M. Merisalu, P. Paiste, J. Aruväli, J. Leis, V. Sammelselg, S. Holdcroft, K. Tammeveski, Transition metal-containing nitrogen-doped nanocarbon catalysts derived from 5-methylresorcinol for anion exchange membrane fuel cell application, J. Colloid Interface Sci. 584 (2021) 263–274.

[III] K. Kisand, A. Sarapuu, A. Kikas, V. Kisand, M. Rähn, A. Treshchalov, M. Käärik, H.-M. Piirsoo, J. Aruväli, P. Paiste, J. Leis, V. Sammelselg, A. Tamm, K. Tammeveski, Bifunctional multi-metallic nitrogen-doped nanocarbon catalysts derived from 5-methylresorcinol, Electrochem. Commun. 124 (2021) 106932.

[IV] K. Kisand, A. Sarapuu, J.C. Douglin, A. Kikas, A. Treshchalov, M. Käärik, H.-M. Piirsoo, P. Paiste, J. Aruväli, J. Leis, V. Kisand, A. Tamm, D.R. Dekel, K. Tammeveski, Templated nitrogen-, iron-, and cobalt-doped mesoporous nanocarbon derived from an alkylresorcinol mixture for anion-exchange membrane fuel cell application, ACS Catal. 12 (2022) 14050–14061.

[V] K. Kisand, A. Sarapuu, S. Akula, A. Kikas, A. Treshchalov, M. Käärik, J. Kozlova, J. Aruväli, J. Leis, V. Kisand, K. Kukli, F. Jaouen, K. Tammeveski, Iron and manganese co-doped mesoporous carbon-based catalysts via template-assisted synthesis for proton exchange membrane fuel cells (manuscript).

[VI] K. Kisand, A. Sarapuu, J.C. Douglin, A. Kikas, A. Treshchalov, M. Käärik, J. Kozlova, J. Aruväli, J. Leis, V. Kisand, K. Kukli, D.R. Dekel, K. Tammeveski, Hierarchically porous Fe-N-C single-atom catalysts via ionothermal synthesis for oxygen reduction reaction (manuscript).

Author's contributions:

Paper I: The author is responsible for material preparation, electrochemical testing and data analysis. The author is responsible for the interpretations of results and writing the manuscript.

Paper II: The author is responsible for material preparation, electrochemical testing and data analysis. The author is responsible for the interpretations of results and writing the manuscript.

Paper III: The author is responsible for material preparation, electrochemical testing and data analysis. The author is responsible for the interpretations of results and writing the manuscript.

Paper IV: The author is responsible for material preparation, electrochemical testing (expect for fuel cell measurements) and data analysis. The author is responsible for the interpretations of results and writing the manuscript.

Paper V: The author is responsible for material preparation and data analysis, partly responsible for electrochemical testing. The author is responsible for the interpretations of results and writing the manuscript.

Paper VI: The author is responsible for material preparation, electrochemical testing (expect for fuel cell measurements) and data analysis. The author is responsible for the interpretations of results and writing the manuscript.

2. ABBREVIATIONS AND SYMBOLS

$\%H_2O_2$	peroxide percentage yield
ΔE	potential gap defined as E_{j10}-$E_{1/2}$
5MR	5-methylresorcinol
AEI	anion exchange ionomer
AEM	anion exchange membrane
AEMFC	anion exchange membrane fuel cell
ASR	area specific resistance
BET	Brunauer-Emmett-Teller
BEV	battery electric vehicle
BF	bright field
CCL	cathode catalyst layer
CCM	catalyst coated membrane
CNS	carbon nanosphere
C_{O2}	O_2 solubility
CV	cyclic voltammogram
DCDA	dicyandiamide
DFT	density functional theory
D_{O2}	diffusion coefficient of O_2
E_0	standard potential
$E_{1/2}$	half-wave potential
E_{j10}	the potential at j_{OER} = 10 mA cm^{-2}
E_{onset}	onset potential
EDS	energy dispersive X-ray spectroscopy
EIS	electrochemical impedance spectroscopy
ETFE	ethylene-co-tetrafuoroethylene
EXAFS	extended X-ray absorption fine structure
F	Faraday constant
FA	formaldehyde
FC	fuel cell
FCEV	fuel cell electric vehicle
FWHM	full width at half-maximum
GC	glassy carbon
g–C_3N_4	graphitic carbonitride
GDE	gas diffusion electrode
GDL	gas diffusion layer
HAADF	high-angle annular dark field
HMT–PMBI	poly[2,2′-(2,2″,4,4″,6,6″-hexamethyl-p-terphenyl-3,3″-diyl)-5,5′-bibenzimidazole]
HOR	hydrogen oxidation reaction
HR–TEM	high-resolution transmission electron microscopy
ICP–MS	inductively coupled plasma mass spectrometry
I_d	disk current

I_r	ring current
j	current density
j_d	diffusion-limited current density
j_k	kinetic current density
K–L	Koutecký-Levich
LDPE	low-density polyethylene
LSV	linear sweep voltammetry
MEA	membrane electrode assembly
M–N–C	metal-nitrogen-carbon
M–N_x	metal-nitrogen coordinated site
MP-AES	microwave plasma atomic emission spectroscopy
N	collection efficiency of the Pt ring
n	electron transfer number per O_2 molecule
NLPM	normal liters per minute
OER	oxygen evolution reaction
ORR	oxygen reduction reaction
PEFC	polymer electrolyte fuel cell
PEM	proton exchange membrane
PEMFC	proton exchange membrane fuel cell
PGM	platinum-group metal
P_{max}	maximum power density
PSD	pore size distribution
PVP	polyvinylpyrrolidone
QSDFT	quenched solid density functional theory
RDE	rotating disk electrode
RHE	reversible hydrogen electrode
RRDE	rotating ring-disk electrode
S_{BET}	specific surface area
SCE	saturated calomel electrode
SD	site density
SEM	scanning electron microscopy
STEM	scanning transmission electron microscopy
SHE	standard hydrogen electrode
SLPM	standard liters per minute
TOF	turnover frequency
TPB	triple phase boundary
VKG	Viru Keemia Grupp
v	potential scan rate
V_{tot}	total pore volume
V_μ	micropore volume
XANES	X-ray absorption near edge structure
XPS	X-ray photoelectron spectroscopy
XRD	X-ray diffraction
ν	kinematic viscosity of the solution
ω	electrode rotation rate

3. INTRODUCTION

The current geopolitical landscape has prompted discussions regarding Europe's energy security. The European Commission has taken steps to diversify energy sources and proposed a strategic policy shift that aims to displace a significant portion of fossil fuels with green hydrogen [1]. This new energy policy could accelerate the establishment of green hydrogen infrastructure across Europe. Hydrogen fuel cells (FCs) offer a versatile energy solution as they can provide clean energy across many applications, including electric vehicles, residential homes, boats, and serve as backup power generators.

The focus is increasingly turning toward fuel cell electric vehicles (FCEVs) [2,3], particularly in the heavy-duty transportation sector, and over the next decade, FCEVs are projected to achieve cost competitiveness with battery electric vehicles (BEVs). FCEVs and BEVs are not competitors but rather complementary technologies capable of utilizing renewable energy [4]. Although BEVs have higher energy efficiency from a well-to-wheel perspective [5,6], FCEVs can offer higher capacity utilization rates with quicker refueling times and better tolerance to lower temperatures [7]. Thus, both BEVs and FCEVs contribute unique strengths, emphasizing the need for an encompassing approach to our clean energy future.

Despite significant progress in fuel cell design, their adoption still lags far behind other devices like batteries, partly due to the expensive Pt-based catalysts currently used in commercial fuel cells [8,9]. The scarcity of platinum will inevitably pose a critical bottleneck during scale-up. Approximately 190 tons of platinum is mined annually, and in modern fuel cells, a minimum of 0.1 g of Pt per kW is required [10]. Moreover, platinum is heavily concentrated in South Africa and Russia, raising significant geopolitical concerns [11]. Addressing these challenges is essential for large-scale fuel cell implementation. Consequently, intensive research is underway to develop alternative catalyst materials that can mitigate the issue of raw material scarcity. Platinum group metal (PGM)-free catalysts, usually prepared from organic precursors along with nitrogen and transition metals sources, could provide a suitable alternative. In 2017, Ballard's FCgen-micro-NPMC, the world's first proton exchange membrane fuel cell (PEMFC) stack utilizing a PGM-free catalyst at the cathode, was commercialized, a groundbreaking achievement in the field of fuel cells. It still employs platinum at the anode, but replacing Pt at the cathode with a PGM-free catalyst leads to an impressive 80% reduction in total PGM content for this stack compared to its PGM-based counterpart [12]. However, achieving optimal performance and durability for more demanding applications, such as automotive use, will require further research.

As such, the aim of the research presented in this PhD thesis was to develop PGM-free resorcinol-derived electrocatalysts for the oxygen reduction reaction (ORR) for use in polymer electrolyte fuel cells. The catalysts were prepared from either 5-methylresorcinol (5MR) or a mixture of alkylresorcinols (Honeyol^{TM})

obtained from Viru Keemia Grupp (Estonia). In the first part of the work, catalysts were synthesized via pyrolysis of 5MR-formaldehyde (FA) resins and doped with nitrogen and transition metals (Fe and Co) [I]. In the second part of the work, the precursor ratios were optimized to obtain the catalysts with the highest ORR activity using one-pot synthesis with 5MR as the carbon precursor [II], and in the third part the addition of Ni was investigated to obtain bifunctional catalyst materials for ORR and oxygen evolution reaction (OER) [III]. In the fourth part of the work, Honeyol was used as the carbon precursor, and the materials' nanostructure was modified using a magnesium-based template [IV and V]. In the fifth part of the work ionothermal synthesis with Honeyol in the presence of Mg nitrate was used [VI]. The prepared catalysts were characterized with various physio-chemical methods to gain insight into their active sites and morphology. The effect of different dopants and the nanostructure of the materials on the oxygen reduction activity was studied in half-cell tests via rotating disk electrode or rotating ring-disk electrode methods. The synthesized materials were also used as cathode catalysts in the anion exchange membrane fuel cell (AEMFC) and proton exchange membrane fuel cell (PEMFC).

4. LITERATURE OVERVIEW

4.1 Polymer electrolyte fuel cells

A fuel cell serves as a device that directly converts chemical energy of a fuel (such as hydrogen) and an oxidant (e.g. oxygen) into three outputs: electricity, heat, and reaction products (typically water). Among different types of fuel cells, polymer electrolyte fuel cells (PEFCs) have been widely researched. PEFCs are further divided into proton exchange membrane fuel cells (PEMFCs) and anion exchange membrane fuel cells (AEMFCs), depending upon the ionomer and polymer membrane employed (Figure 1). Although high-temperature variants of these fuel cells exist (at operating temperatures above 100 °C), the predominant research focus remains on those operating below 100 °C [13]. Due to their high efficiency, safety, and the potential for rapid start-stop cycles, they are exceptionally suitable for portable applications, including the automotive sector [14].

During FC operation, the fuel is oxidized on the anode, in the case of hydrogen fuel the reaction is called the hydrogen oxidation reaction (HOR). Simultaneously, the oxygen reduction reaction (ORR) is occurring on the cathode. In PEMFCs, protons are conducted through the membrane, while in AEMFCs, OH^- ions are conducted instead. Since the membrane acts as an electrical insulator, electrons traverse an external circuit, where they contribute to useful work. The kinetics of the HOR are quite fast. However, the ORR is more intricate, necessitating the transfer of four electrons per O_2 molecule. Additionally, the ORR involves cleaving a double oxygen-oxygen bond, further contributing to sluggish kinetics.

At low pH conditions (i.e. in PEMFCs) the ORR can follow either a 4-electron pathway [15,16]:

$$O_2 + 4H^+ + 4e^- \rightarrow 2H_2O \qquad E_0 = 1.229\ \text{V}, \tag{1}$$

or a 2-electron pathway:

$$O_2 + 2H_2 + 2e^- \rightarrow H_2O_2 \qquad E_0 = 0.67\ \text{V}, \tag{2}$$

followed by further reduction of hydrogen peroxide

$$H_2O_2 + 2H_2 + 2e^- \rightarrow 2H_2O \qquad E_0 = 1.77\ \text{V} \tag{3}$$

or disproportionation reaction

$$2H_2O_2 \rightarrow 2H_2O + O_2 \tag{4},$$

with all the standard potential (E_0) values given versus the standard hydrogen electrode (SHE) at 25 °C.

In alkaline conditions (i.e. in AEMFCs) the ORR can also proceed via two main pathways. The 4-electron pathway:

$$O_2 + 2H_2O + 4e^- \rightarrow 4OH^- \qquad E_0 = 0.401\ \text{V}, \tag{5}$$

or 2-electron pathway:

$$O_2 + H_2O + 2e^- \rightarrow HO_2^- + OH^- \qquad E_0 = -0.065\ \text{V}, \tag{6}$$

followed by further reduction of HO_2^-

$$HO_2^- + H_2O + 2e^- \rightarrow 3OH^- \qquad E_0 = 0.867\ \text{V}, \tag{7}$$

or disproportionation reaction

$$2HO_2^- \rightarrow 2OH^- + O_2 \tag{8}.$$

In fuel cells, the $4e^-$ ORR pathway is favored due to the potential risk posed by hydrogen peroxide or hydroperoxide anions, which can corrode fuel cell components if not further reduced [17].

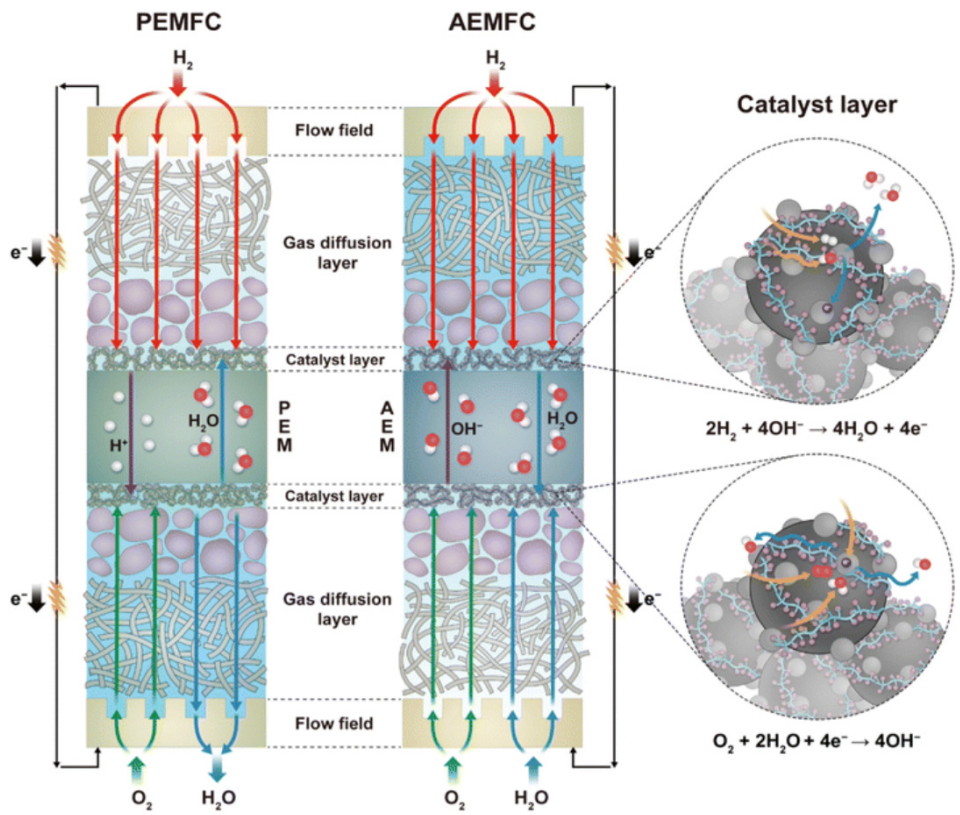

Figure 1. Schematics of a PEMFC and an AEMFC, adapted from [18].

The theoretical efficiency of PEFCs reaches 83%. However, practical realities bring this down to approximately 40%, still more than double the efficiency of today's conventional internal combustion engines [5]. This discrepancy in theoretical and practical efficiency arises from several factors, which occur during the operation of the fuel cell and cause the actual cell voltage to fall below the equilibrium potential (1.23 V). Firstly, ohmic losses, which are dominant at intermediate current densities and result from proton or OH^- anion transfer resistance within the electrolyte. Secondly, mass transport losses that stem from lower reactant concentrations at the electrode/electrolyte interfaces, which are particularly pronounced at higher current densities. Finally, the activation losses which are caused by the sluggish kinetics of the HOR and particularly the ORR. Catalysts are employed at both the anode and cathode to accelerate the reactions and reduce the activation polarization [9,19,20]. While the HOR proceeds efficiently even with minimal catalyst amounts, the ORR demands significantly larger catalyst quantities [21]. As a result, current research and development efforts heavily emphasize the study and advancement of ORR catalysts [22].

A fuel cell stack is composed of multiple single cells, referred to as membrane electrode assemblies (MEAs), which are typically tested using a single cell setup. This setup consists of monopolar flow field plates and compression hardware that interface the cell with the test station. The MEA comprises the anode and cathode catalyst layers, which are deposited either on gas diffusion layers (GDLs), known as gas diffusion electrodes (GDEs), or on both sides of the membrane, known as catalyst-coated membranes (CCMs). The GDLs, usually made of carbon fibers or carbon paper, serve to efficiently transport gases to and water from the electrodes. The catalyst material consists of catalytically active particles (usually Pt or its alloys) deposited on a carbon support along with an ionomer that provides the ionic conductivity. The ionomer composition is usually similar to the membrane to ensure compatibility. The GDEs or GDLs are then combined with the membrane or CCM pressed together to obtain an MEA. The MEA is subsequently sandwiched between flow field plates, which serve as further channels for gas and water vapor transport. These plates are made of graphite or metal coated with corrosion-resistant layers to withstand acidic conditions [23].

The polymer electrolyte membrane should exhibit high ionic conductivity, chemical and thermal stability, low gas permeability, and feasible mechanical properties, including good strength and flexibility. The balance between these factors is crucial, for example, it should be as thin as possible to ensure good ionic conductivity, but not so thin that it causes problems with gas crossover or mechanical degradation [9]. The polymer membranes are chemically functionalized to facilitate the conduction of protons or hydroxide ions. The specific functional groups present in the membrane determine the environment within the fuel cell. For instance, proton-conducting membranes typically feature sulfonic acid functional groups, resulting in an acidic environment. Nafion™, developed in the early 1970s, remains widely used in PEMFCs due to its excellent properties [24]. In contrast, hydroxide-conducting membranes have not yet reached the same technological maturity level. Initially, the primary concern with anion

exchange membranes (AEMs) centered around their OH^- conductivity, which in the early years was not able to compete with the H^+ conductivity of proton exchange membranes (PEMs). Recently, however, the best-performing AEMs have achieved ten-fold improvement in ionic conductivity, signifying substantial improvements [25]. However, low durability still remains a common issue with all AEMs [17]. Performance losses may arise from carbonation upon exposure to CO_2 and degradation of the AEM through nucleophilic attack [17]. Consequently, the selection of AEMs remains diverse, and a clear frontrunner has yet to emerge. The absence of an available AEM standard, similar to Nafion in PEMFCs, complicates performance comparisons across different catalysts. As seen from Table 1, many different membranes, ionomers and experimental conditions have been used in AEMFC tests, which makes it exceedingly difficult to compare the results against each other.

The operational environment of a fuel cell imposes stringent constraints on material selection. In PEMFCs, platinum-group metals currently dominate due to their robust stability. However, ongoing research aims to develop cost-effective alternatives to platinum. PGM-free catalysts based on nitrogen and inexpensive transition metals (Fe, Co, Mn) have shown promising performance, with the best results obtained with H_2/O_2 in PEMCFs displaying a maximum power density (P_{max}) of slightly above 1 W cm^{-2} [26,27], which is somewhat lower than the best AEMFC results (see Table 1). In addition, PGM-free catalysts face significant challenges in the harsh acidic environment, due to their low stability [28]. Thus, PGM-free catalysts may find greater success in AEMFCs, as these materials generally exhibit better stability and activity in alkaline conditions [29,30]. Different PGM-free materials and their synthesis approaches are discussed in more detail in Section 4.3.

Table 1. AEMFC performance of resorcinol-derived cathode catalysts prepared in this Thesis, compared against other transition metal based PGM-free cathode catalysts found in the literature.

Cathode catalyst	Cathode loading ($mg\,cm^{-2}$)	Anode loading ($mg_{PtRu}\,cm^{-2}$)	Membrane	Cell temp. (°C)	P_{max} ($W\,cm^{-2}$)	Ref.
FeCoNC-OP	2.0	0.60	HMT-PMBI	80	0.41	[II]
FeCoNC	0.96	0.57	LDPE	55	0.42	[IV]
FeCoNC-MgOAc	0.96	0.57	LDPE	55	0.92	[IV]
FeNC-LT	0.90	0.75	FAA-3-05-RF	80	0.25	[VI]
Fe-N-C	1.00	0.60	HDPE	80	2.05	[31]
Fe-Mn-N-C	0.8	0.40	PAP-TP-85	80	1.3	[32]
O-FeN4C-O	0.8	0.40	PAP-TP-85	80	1.2	[33]
Fe–N-PDC-HA	1.1	0.60	Xion Pention	80	1.1	[34]
CoFe/VC	2.4	0.70	LDPE	70	1.35	[35]
FeCoPc/C	0.30	0.70	LDPE	80	1.26	[36]
CoFe-N-CDC/CNT	0.75	0.74	ETFE	60	1.12	[37]
$Fe_{0.5}$-NH_3	1.5	0.90	ETFE	60	1.10	[38]
Co-N-CDC/CNT	0.75	0.74	ETFE	60	1.06	[37]
α-Mn_2O_3/$Fe_{0.5}$-NH_3	1.2	0.90	ETFE	60	1.0	[38]
Fe-N-CDC/CNT	0.71	0.74	ETFE	60	0.88	[37]
FeCoN-MWCNT	0.75	0.70	FAA-3-05-rf	60	0.69	[39]
FeCoNC(Mg)	0.62	0.75	FAA-3-05-rf	80	0.83	[40]
Fe/N/CNT	2.0	0.40	*a*QAPS-S_8	60	0.49	[41]
FeMn-N-MPC	2.0	0.80	HMT-PMBI	60	0.47	[42]
Fe-N-MPC	2.0	0.80	HMT-PMBI	60	0.46	[42]
Fe-Co-N-C	1.0	1.00	LDPE	60	0.42	[43]
FeN-SiCDC-0.5–400-wet-PVP	2	0.80	HMT-PMBI	60	0.36	[44]
Fe/IL-PAN-A1000	2.0	0.60	HMT-PMBI	60	0.29	[45]
Fe-N-Gra	2.0	0.60	HMT-PMBI	60	0.24	[46]
Fe-N-C	2.0	0.60	HMT-PMBI	60	0.22	[47]
FeCN-S-800	3.0	0.80	FAA-3	50	0.125	[48]
CoNPC-71	4.0	0.50	A201	60	0.068	[49]
SiCDC/CNT(1:3)/CoPc	0.7	0.70	ETFE	60	0.47	[50]
TiCDC/CNT(1:3)/FePc	2.0	0.80	HMT-PMBI	60	0.18	[51]
Co-N-CDC/CNT_mel	2.0	0.60	HMT-PMBI	60	0.58	[52]
FeNiN-MWCNT	2.0	0.80	Aemion+ (10 μm)	65	0.41	[53]
CoFe-N-OMC/CNT	2.0	0.40	Aemion+(10 μm)	65	0.35	[54]
MPF/Fe	1.0	0.40	Aemion+ (10 μm)	65	0.35	[55]
Fe1Co1-ZNT-900	2.0	0.80	Aemion+ (15 μm)	65	0.17	[56]
Fe@Fe–N–C	1.0	0.40	Aemion+ (15 μm)	65	0.24	[57]
FeNSC2	2.0	0.80	Aemion+ (10 μm)	65	0.16	[58]

4.2 Catalyst characterization

4.2.1 Electrochemical characterization methods

The performance evaluation of the ORR on PGM-free catalysts is typically conducted using linear sweep voltammetry (LSV) with a rotating disk electrode (RDE) or a rotating ring-disk electrode (RRDE). These methods are widely employed for screening of the ORR electrocatalytic performance of the catalysts due to their operational simplicity and cost-effectiveness [59]. The catalyst sample is initially dispersed in a homogeneous ink composed of solvent and binder. The ink is then deposited on a glassy carbon RDE, left to dry and inserted into an electrochemical measurement cell containing an acidic or alkaline electrolyte solution, to be used as a working electrode. Subsequently, the potential is scanned at a fixed rate, typically maintained below 20 mV s^{-1} to minimize the contribution from capacitive (background) currents. Simultaneously, the RDE is rotated at fixed rates to mitigate mass-transfer limitations during the ORR evaluation. The electrocatalytic activity of a material toward the ORR is generally assessed using two key parameters obtained from the polarization curve: the onset potential (E_{onset}) and the half-wave potential ($E_{1/2}$). The onset potential is defined as the potential at which O_2 reduction commences, accompanied by an increase in current density (usually −0.1 mA cm^{-2}). The half-wave potential represents the potential required to achieve a current density that is half of the value observed in the diffusion-limited region. Higher $E_{1/2}$ and E_{onset} values indicate a lower overpotential necessary to catalyze the ORR, reflecting superior electrocatalytic activity [59].

Usually, the Koutecký-Levich (K-L) analysis is used to gain information about the number of electrons (n) participating in the ORR. Polarization curves are measured at different rotation rates and several parameters can be extracted from the slope of the j^{-1} vs. $\omega^{-1/2}$ plot using the K-L equation [60]:

$$\frac{1}{j} = \frac{1}{j_k} + \frac{1}{j_d} = \frac{1}{j_k} - \frac{1}{0.62nFD_{O_2}^{2/3}\nu^{-1/6}c_{O_2}^{b}\omega^{1/2}} \tag{9}$$

where j is the measured current density, j_k and j_d are the kinetic and diffusion-limited current densities, respectively, F is the Faraday constant, ω is the electrode rotation rate (rad s^{-1}), D_{O2} is the diffusion coefficient of O_2, C_{O2} is the O_2 solubility and ν is the kinematic viscosity of the electrolyte solution.

A more direct approach to assess the number of participating electrons involves using the RRDE method. In this technique, the working electrode is encircled by a ring electrode with a separate fixed potential applied to it. Consequently, the hydrogen peroxide produced by the catalyst on the disk electrode undergoes oxidation at the ring electrode. The current response can be used to directly obtain the number of electrons involved in the ORR [59].

The RDE and RRDE methods are well-established, and often used for preliminary screening of potential electrocatalysts, however the obtained results are

not necessarily indicative of performance in a fuel cell and might lead to a misleading conclusion [61]. The transition from a double to a triple phase boundary from half-cell to MEA can impact properties such as active site utilization and mass transport limitations [62]. Additionally, degradation of catalysts is influenced by the charge passed, and rotating disk electrodes operate at least two orders of magnitude lower current densities than a FC device. Furthermore, reaction kinetics and degradation mechanisms are temperature-dependent, but most half-cell tests are conducted at room temperature rather than the higher temperatures of around 60-80°C commonly used in polymer electrolyte fuel cells [63,64]. Hence, although the RDE and RRDE methods are suitable for the initial estimation of the catalysts' ORR activity, promising catalysts must be investigated as cathodes in MEAs to assess their performance under more realistic conditions. These experiments are considerably more intricate, in large part due to the complexity of MEA preparation. Additionally, during the measurement, numerous parameters come into play that can significantly impact performance, such as cell temperature, gas flow rates, humidification, pressures and selection of cell components. The optimization of these parameters is crucial for minimizing voltage losses [19]. The successful transport of reactants and products critically relies on water management within the cell. Insufficient water content can lead to membrane and ionomer drying, increasing the internal resistance, but excessive water can flood the cell, hindering the formation of triple phase boundaries (TPBs). Precise control over water quantity and distribution within the cell remains a critical research focus, particularly in AEMFCs where water is both a reactant and product [65,66].

4.2.2 Physical characterization methods

In addition to electrochemical characterization, physical methods are required to assess the effect of the catalysts' structure and composition to their electrocatalytic performance. This is especially important yet complicated for PGM-free catalysts, because altering a single synthesis parameter (for example the pyrolysis temperature) often affects multiple properties of the materials simultaneously.

Scanning electron microscopy (SEM) can be used to study the morphology of the catalyst materials. SEM with energy dispersive X-ray spectroscopy (EDS) can also produce elemental distribution maps. However, SEM-EDS mapping does not have high enough resolution to distinguish smaller nanoscale particles. Catalyst powders and layers can be further assessed using transmission electron microscopy (TEM) coupled with EDS. These techniques offer high resolutions, and aberration-corrected TEM microscopes can even achieve atomic-level resolution [67]. As a result, the high-resolution scanning transmission electron microscope (HR-STEM) with spherical aberration correction has become one of the main tools to detect single atom sites.

X-ray photoelectron spectroscopy (XPS) enables the characterization of site coordination in metal-nitrogen-carbon (M–N–C) catalysts, providing insights into surface species and their oxidation states. One advantage of XPS is its surface

sensitivity, as depth profiling is restricted to 1–5 nm. XPS can determine both the elemental composition in the surface layers of the catalysts and the chemical states of individual elements. This compositional information is derived from XPS survey spectra through curve-fitting of core-level spectra, offering crucial insights into the presence of various moieties. Typically, core-level fitting focuses on the C 1s, O 1s and N 1s edges for lab-scale instruments due to limited signal-to-noise ratios. The N 1s spectra commonly exhibit multiple peaks representing nitrogen in different states. Similarly, 2p spectra of transition metals may reveal peaks corresponding to metallic nanoparticles, metal oxides, and M–N_x species, although due to their low concentration, peak fitting is usually avoided [68]. In addition, the detailed Fe 2p photoelectron spectra consist of multiple peaks corresponding to oxidized forms, which can be bulk oxides, but also nitrogen-coordinated metal. As such, it is not possible to precisely identify these components by XPS analysis, as there are several different overlapping metal states, consisting of multiple peaks due to multiplet splitting and charge transfer effects [69,70].

A drawback to XPS (as with other ex-situ characterization techniques) is the difficulty in distinguishing active sites from other species. Additionally, it is important to interpret these results cautiously, considering potential inconsistencies resulting from different XPS peak fitting methods [71].

Gas adsorption experiments serve as a valuable means to gather data regarding surface area, pore volume, and pore size distribution (PSD). These experiments are widely employed in characterizing micro- and mesoporous materials. Nitrogen and carbon dioxide are the most commonly utilized probe gases [72]. Different models for data analysis are used, from which the quenched solid density functional theory (QSDFT) is the most widely used for hierarchically porous materials. QSDFT takes into account the morphological specifics of different structures present in carbon materials, i.e. the chemical and geometrical heterogeneity of the pore walls [73].

Other commonly used techniques include Raman spectroscopy, X-ray diffraction (XRD) and inductively coupled plasma mass spectrometry (ICP-MS) or microwave plasma atomic emission spectroscopy (MP-AES). Raman spectroscopy allows to characterize the degree of graphitization, i.e. structural defectiveness of the carbon. Higher graphitization improves the stability and electrical conductivity of the carbon material. Typically, the I_D/I_G Raman band ratio is used, where I_D corresponds to the intensity of the amorphous carbon peak and I_G to the intensity of the scattering from sp^2 carbon. A higher I_D/I_G ratio indicates a more disordered carbon material. However, it is important to note that using the I_D/I_G ratio is problematic since in highly disordered carbon materials, the Raman peak labeled as G is a combination of the G and D2 peaks. This overlap makes the I_D/I_G ratio an unreliable indicator of structural disorder in such materials [74,75]. To assess the extent of structural disorder in the catalyst materials, the full width at half-maximum (FWHM) of the D1 and G+D2 bands, as well as the I_D/I_{G+D2} ratio is used [76]. XRD is used to investigate the crystalline phases present in the materials; these can be metal oxides, carbides or metal nanoparticles. MP-AES

or ICP-MS is used for quantitative analysis of the different metals present in the catalyst [77].

In addition, some more advanced techniques have been used to determine the active sites in PGM-free catalyst materials. The most commonly used are Mössbauer spectroscopy that allows for differentiation of ^{57}Fe species in the catalyst, providing valuable information on the nature of the active sites. As well as various synchrotron radiation-based absorption spectroscopic techniques like X-ray absorption near edge structure (XANES) or extended X-ray absorption fine structure (EXAFS) that can elucidate the chemical valence states and coordination environments of the $M–N_x$ sites [67,68].

Despite extensive research, no characterization technique has definitively revealed the origins of the ORR activity and active sites in PGM-free catalysts. A comprehensive understanding of the ORR mechanism remains essential for advancing PGM-free catalysts and ensuring their practical viability [12,78]. Progress in this area necessitates the development of additional, potentially more sophisticated characterization techniques that provide direct insights into the catalyst surface. A potential approach could be conducting operando and in situ studies at atomic resolution while simultaneously measuring the system's electrochemical response in real time [77].

4.3 PGM-free carbon-based electrocatalysts

4.3.1 Synthesis methods

In the long term, Pt-based catalysts are not a sustainable solution for PEFCs and the US Department of Energy has also shifted its focus toward PGM-free catalysts in recent years, as reflected in their roadmaps [79]. The first study for a PGM-free fuel cell catalyst was published by Jasinski in 1964 [80]. A breakthrough in PGM-free catalyst preparation occurred when Gupta et al. successfully synthesized a catalyst by pyrolyzing simple and cost-effective metal and nitrogen precursors with high surface area carbon [81]. Subsequent advancements have significantly improved the activity of PGM-free catalysts; there are now many PGM-free catalysts with high potential for commercialization [12,78,82]. While the raw material costs are significantly lower than for PGMs, manufacturing expenses at low volumes could be higher due to the substantial manufacturing setup costs [12]. Consequently, the cost savings may be minimal, at least in the short term, but PGM-free catalysts are expected to be significantly cheaper in the future. An additional advantage of PGM-free catalysts lies in their enhanced resistance to airborne contaminants, compared to PGM-based catalysts [83]. PGM-free electrocatalysts must satisfy four essential criteria. The first three encompass the electrochemical and structural factors: (i) the presence of high density of active sites enabling fast ORR kinetics, (ii) sufficient electrical conductivity, and (iii) a porous microstructure facilitating efficient mass transfer of products and reactants to and from the active sites. Additionally, the carbon-based

catalyst must be cost-effective and straightforward to be produced in large quantities. For these reasons, high-temperature pyrolysis in an inert atmosphere, such as Ar or N_2, has emerged as the most widely used synthesis method [30,84]. Pyrolysis is typically done at temperatures from 600 °C to 1000 °C; at these temperatures the reactions with the precursor, such as condensation, crosslinking, dehydration and carbonization will occur [30]. Carbon constitutes the majority of the material (by atomic percentage) and contributes to its chemical stability, electrical conductivity, porous structure, and mechanical strength. Usually, additional heteroatom precursors are introduced and volatile compounds are released during the thermal decomposition, thereby functionalizing the resulting carbons and introducing the active sites; a process known as doping [85]. Doping typically utilizes elements like nitrogen, sulfur or phosphorus with N being the most widely used dopant [86]. To enhance the ORR activity, transition metals are often introduced [87]. M–N–C catalysts consist of a combination of transition metal, nitrogen, and carbon. While various metals have been employed in M–N–C catalysts, such as Ni, Mn, or Cu, the Fe- and Co-containing catalysts have displayed greater ORR performance [35,78,87].

Previously, the M–N–C catalysts were synthesized mainly by doping of carbon materials, which involves preparing a mixture containing a pre-existing carbon carrier, a nitrogen dopant and a metal salt. The mixture is then subjected to pyrolysis to introduce the nitrogen and metal dopants into the carbon material, thereby generating active sites for ORR. The precursors are mixed in a liquid phase either by sonication or stirring; in some cases a solid phase synthesis is used (i.e. grinding or ball-milling) [88,89]. This method has the advantage of utilizing an existing carbon material with a pre-determined structure. However, these catalysts inevitably suffered from the drawback of metal species aggregation during pyrolysis, resulting in a reduced density of $M–N_x$ moieties in the catalyst [27]. More recently, another approach emerged referred to as the in-situ doping method. In this method, carbon is formed concurrently with the active sites by pyrolyzing a carbon precursor alongside nitrogen and metal sources [63,90]. This limits the aggregation of metal species and generally allows for a higher concentration of active sites compared to the previous method. However, it is more challenging to control the structure and porosity of the resulting catalyst [91]. In both cases, certain metal species generated during high-temperature pyrolysis may pose a risk to catalyst stability, as they are highly prone to dissolution in fuel cell operating conditions. The dissolved iron species, in particular, can detrimentally affect catalyst performance and also degrade the polymer membrane in the fuel cell by generating free radicals through the Fenton reaction [92]. Therefore, one or more acid leaching steps are typically necessary at the end of the catalyst synthesis process to remove undesirable metal species [93].

In conclusion, currently there are two main research directions to further improve the performance of PGM-free catalysts in fuel cells. Firstly, increasing the active site density (SD) and enhancing the turnover frequency (TOF) of the active sites [64]. As such, a better understanding of the nature of the active sites for ORR is necessary and a deeper understanding of the pyrolysis step and how

the active sites are formed during the heat-treatment is crucial [64]. Secondly, improving mass transport within the catalyst layers of PGM-free cathodes, which due to the lower volumetric activity of catalyst need to be significantly thicker, as compared to PGM-based catalysts [12]. Remaining gaps need to be addressed and a deeper understanding of how to integrate PGM-free catalysts into cathode catalyst layers (CCLs) is needed. In addition, coordinating future catalyst and CCL research is essential to streamline the development process. Identifying and comprehending potential synergies early on will significantly help to reduce the development timeline [12].

4.3.2 Active sites in PGM-free catalysts

The intrinsic electrocatalytic activity of M–N–C catalysts is linked to their constituent moieties, most importantly to various centers containing nitrogen and transition metal (Figure 2). Although a scientific consensus as to which of the sites contribute to the ORR activity has not been reached, transition metal-nitrogen coordinated ($M–N_x$) sites are generally thought to be involved [87,91], the activity of which can also be influenced by their local ligand environment [64]. Catalysts containing $Fe–N_x$ sites are the most commonly employed, but other metals such as Co, Mn, or Ni have also shown good performance [87]. Mn-doped catalysts particularly have garnered attention for their potential to mitigate the generation of reactive oxygen species via Fenton-like reactions involving hydrogen peroxide that is produced through a 2-electron ORR pathway [94,95]. These species cause oxidative processes in the catalyst layer, resulting in carbon corrosion and loss of the embedded active sites along with deterioration of other cell components like the ionomer and membrane [96]. Notably, Li et al. demonstrated that Mn-containing catalysts exhibit increased stability even in harsh oxidative environments [95]. However, generally these catalysts show comparatively lower ORR performance than their iron-containing counterparts [95]. To address the limitations inherent in single-site catalysts, specifically their insufficient activity and stability, an alternative approach involves designing catalysts that incorporate dual or multiple metal sites [32,67,97]. The advantages of this stem from tailoring the electronic structure, resulting in enhanced electrocatalytic activity and stability. These secondary metal atoms effectively modulate the electronic configuration of $Fe–N_4$ sites, optimizing the adsorption free energy of reaction intermediates and subsequently enhancing the ORR activity [98].

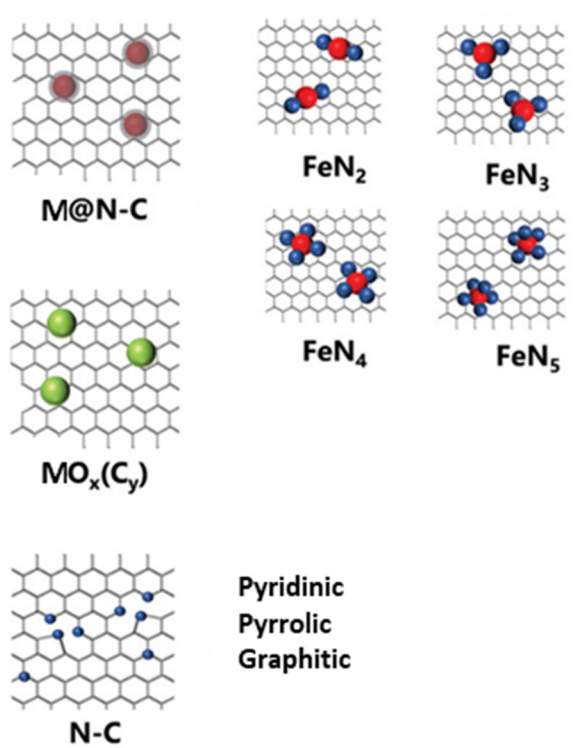

Figure 2. Different active sites of M–N–C-based catalysts for oxygen reduction reaction. Adapted from reference [99].

The biggest challenge with M–N–C catalyst materials is their relatively low site density. Despite significant advances in synthesis approaches, for example by using metal-organic framework precursors to limit the metal ion mobility and prevent agglomeration of metal, it has been noted that surpassing ~3 wt.% Fe in atomically dispersed form, poses significant challenges [100]. This is because as higher concentrations of metal precursors are utilized, condensation of metal atoms will occur. At elevated temperatures, metallic iron can also react with the carbon, leading to the formation of iron carbide [101]. Another approach to M–N–C catalyst synthesis can be done via introducing higher amounts of metal precursors. In addition to M–N_x sites, these catalysts comprise of metallic nanoparticles enveloped by a protective carbon layer, commonly referred to as metal@N-C sites (Figure 2) [102]. Typically, these sites exhibit a lower turnover frequency for the ORR when compared to M–N_x sites. However, it is feasible to achieve a higher metal loading for such catalysts, thereby compensating for the reduced TOF value [103]. Besides the transition metal containing sites, M–N–C catalysts will always include N–C active sites. These sites are widely believed to modulate the activity of the surrounding M–N_x sites, as well as directly contribute to catalytic activity in alkaline conditions, but are usually not considered as active sites in acidic environment [86,104]. Nitrogen moieties in the carbon lattice can

be in several forms, e.g. pyridinic, graphitic, pyrrolic or oxidized (NO_x) species [105]. However, the specific nitrogen sites responsible for enhancing the ORR activity remain unclear. Some researchers associate a high concentration of pyridinic-N with increased ORR activity, while others propose that pyrrolic-N species play a key role [86,106]. As mentioned in Sub-section 4.2.2, this disparity can also be due to different XPS peak fitting methods.

An emerging method to produce catalysts with high density of Fe–N_x sites is the active site imprinting strategy, proposed by Fellinger and coworkers [107], an approach that decouples the formation of the carbon matrix from the creation of the active sites. That could potentially help to overcome the limitations of current methods that rely on kinetic stabilization of metal atoms at high temperatures. This approach uses suitable imprinting metals (Zn, Ca, and Mg) that are known to form stable complexes, to promote the formation of the respective M–N_x sites in the carbon material [107]. At temperatures typically used in pyrolytic carbon preparation, the reduction of Mg^{2+} and Zn^{2+} is not thermodynamically favored. Therefore, this strategy has the ability to create M–N–C catalysts with a significantly higher concentration of M–N_x active sites by preventing unwanted side reactions. Once the Mg–N–C material is prepared, it is subjected to a low-temperature wet-chemical coordination step to replace the N-coordinated Mg^{2+} ions by an electrocatalytically active element, such as iron. However, the reaction mechanism of the trans-metalation step is as of yet unclear [108]. By decoupling the carbonization and active site formation steps, this approach can simplify the development of reliable structure-activity relationships.

4.3.3 Nanostructure of PGM-free catalysts

While PGM-free electrocatalysts have several advantages such as cost-effectiveness and enhanced resistance to contaminants, they pose a challenge due to their lower volumetric activity. Several studies have emphasized the critical importance of hierarchically porous structure of carbon-based catalyst materials for enhancing electrocatalytic performance in FCs [12,90]. An ideal catalyst should form continuous porous channels to facilitate mass transfer (Figure 3). It should be noted that not all N–C or M–N_x moieties can be considered as active sites, because their effectiveness in participating in the ORR depends on where they are situated within the catalyst layer. It has been demonstrated that only the active sites located near the external surface of the catalysts are effectively participating in the ORR, while those buried deeper within the carbon microstructure are inactive [109]. As such, increased mesoporosity of the catalyst will lead to greater utilization of the active sites, especially in fuel cells, as only the sites at the TPB can participate in the ORR [110]. Research on ways of increasing the SD of catalysts has seen a lot of focus [91,97,108]. Unfortunately, improvements in their utilization as genuine active sites have been largely overlooked, representing a significant roadblock to the enhancement of fuel cell performance [27].

Carbon materials with exceptionally high surface area and porosity can be made by deliberate structuring at the micro-, meso- and macroscale during their preparation by the use of a template or an activation step. The most common methods for producing additional porosity are physical activation by using reactive gases such as steam or CO_2 [111,112], and chemical activation [113]. Although these methods result in a high surface area, they create a mainly microporous texture. Synthetic approaches often employ templating methods to create the necessary meso- and macroporous structures. These methods can be categorized into two groups: hard templating and soft templating [114,115]. Soft templates are a variety of block-copolymers and they have been proven to create carbon materials with controlled porosity. However, they are excessively expensive and as they are vaporized during pyrolysis, cannot be recycled [115]. In hard templating, silica nanoparticles are commonly used during thermal treatment to prepare carbon materials with controlled structure. In this process, the template remains stable at high temperatures and the template particles are removed after pyrolysis via chemical etching, resulting in carbon materials with a reverse structure. However, the use of concentrated solutions of HF or NaOH for template removal poses significant limitations, hinders the scalability and raises environmental concerns [115]. In addition, the recycling of dissolved silica in these solutions has never been tried, mainly because of the expected high cost for the recycling processes.

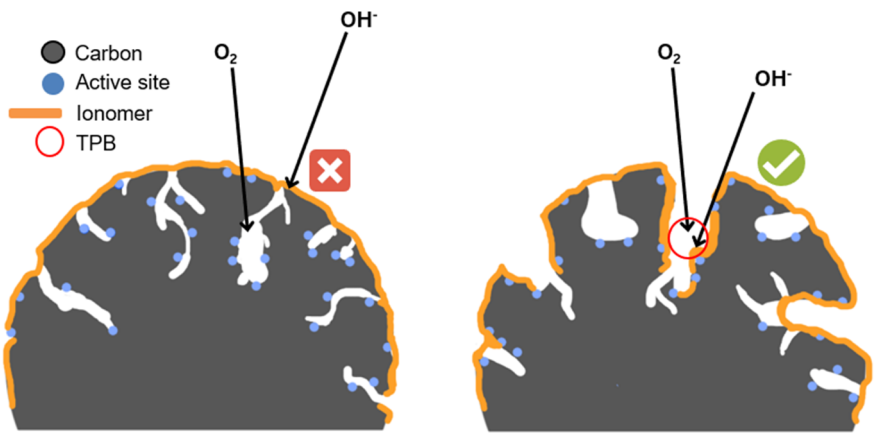

Figure 3. Illustrations of reactant access to microporous (on the left) and mesoporous (on the right) carbon catalysts.

A sustainable alternative to silica-based templates involves using inorganic particles like MgO, $CaCO_3$, ZnO, etc. The main advantage of this method is the ease of removal of the templating phase, as these nanoparticles can be etched out of the carbon material using dilute acid solutions, for example HCl. Inagaki et al. were the first to introduce a method for carbon preparation using this approach [116,117]. They synthesized these materials by pyrolyzing a carbon precursor

alongside MgO or certain thermally unstable magnesium compounds such as acetate, citrate, or gluconate, that are decomposed during pyrolysis to form MgO nanoparticles. These inorganic nanoparticles are subsequently dissolved out of the carbon matrix after carbonization, which results in the creation of mesopores (typically ranging from 2 to 20 nm in diameter). The resulting porosity can be influenced by factors such as the nature of carbon precursor, MgO precursor, and their mass ratio [118]. Another advantage is the recyclability of the Mg template that has been experimentally confirmed using acetic and citric acids [118]. Toyo Tanso Co. Ltd. has recently commercialized the production of mesoporous carbon materials using MgO-based templates under the brand name CNovel® [119].

A derivative of the above-mentioned inorganic template approach is the ionothermal carbonization that utilizes Mg or Zn salts with low melting points [120]. During the process the carbon precursor is partially or completely dissolved within the salt melt. The generation of pores occurs through two effects. First, the formation of nanodroplets of the molten salt, which act as a fluidic template inside the carbonizing precursor. Secondly, a crosslinked carbonizing phase, that encloses the in-situ formed inorganic phase (i.e. MgO or ZnO nanoparticles). After heat-treatment, the template particles are removed, resulting in a porous material. Generally, ionothermal synthesis delivers two straightforward parameters for pore tuning: the compatibility/miscibility of organic precursor phase and molten salt, and the type of salt or eutectic salt mixture that is chosen. In certain limits the porosity can be enhanced simply by increasing the salt to organic precursor ratio. Depending on the necessary carbon structure, different organic precursors can be used, but optimizing the ratio of template to carbon precursor for each combination is needed in order to achieve the demanded pore structure because of different carbon yields [121]. By selecting precursors that contain nitrogen (either in the organic precursor or the salt), it is possible to simultaneously generate $M–N_x$ (M = Mg, Zn) sites that can later be converted to ORR-active sites via the trans-metalation method mentioned in Sub-section 4.3.2.

5. EXPERIMENTAL

5.1 Preparation of PGM-free catalysts

5.1.1 Synthesis of catalysts from 5-methylresorcinol-formaldehyde resin

Nanospheres of 5-methylresorcinol-formaldehyde resin were prepared by a base catalyzed polycondensation of 5-methylresorcinol (5MR) and formaldehyde (FA) [52]. The concentrations of the precursors, given as molar ratios, were the following: 5MR/FA=0.5, 5MR/Na_2CO_3=240, H_2O/5MR=90. 5-methylresorcinol (99.9 %, VKG Oil AS, Estonia) and Na_2CO_3 (≥99.8 %, Honeywell/Fluka) were dissolved in deionized water (Milli-Q), then, the aqueous solution of formaldehyde (35 %, stabilized with ~10 % of methanol, Sigma-Aldrich) was added followed by 48 h of stirring at room temperature. The nanospheres were dried overnight at 60 °C and carbonized in N_2 flow by raising the temperature at a heating rate of 10 °C min^{-1} up to 800 °C and holding at this temperature for 2 h. After cooling down to room temperature the undoped carbon nanospheres (denoted as CNS) were collected. This material was used as a precursor for preparation of N-doped carbon nanospheres (NCNS), Co- and Fe-containing N-doped CNS (CoNCNS and FeNCNS, respectively) [I]. For this, CNSs were suspended in 2-propanol and for preparing Co- and Fe-containing materials, $CoCl_2$ or $FeCl_3$ was added at the mass ratio 1:40 of metal to CNSs. After that, dicyandiamide (DCDA, Sigma-Aldrich) and polyvinylpyrrolidone (PVP, Sigma-Aldrich) were added at the mass ratio of 20:1 and 1:10 to CNS, respectively, and sonicated for 3 h. The solvent was evaporated from the suspension by drying overnight at 70 °C and the obtained powder was pyrolyzed at 800 °C for 2 h.

The second set of N-doped catalysts was synthesized by one-step procedure, pyrolyzing the mixture of 5MR-FA resin nanospheres, DCDA, Fe/Co salt and PVP prepared by the procedure described above, except that two times higher mass of organic nanospheres than that of CNSs was employed. The spherical shape was not retained by this procedure and the porous N-doped carbon materials obtained are denoted as NC-MRFA, CoNC-MRFA and FeNC-MRFA, respectively [I]. To dissolve the possible metal nanoparticles formed during pyrolysis, all the metal-containing catalysts were treated for 8 h in the mixture of 0.5 M HNO_3 and 0.5 M H_2SO_4 at 50 °C. After the acid treatment, the materials were pyrolyzed again at 800 °C for 2 h.

5.1.2 One-pot synthesis of 5-methylresorcinol-derived catalysts

The catalysts were prepared using 5-methylresorcinol (5MR, 99.9%, VKG Oil AS, Estonia), dicyandiamide (DCDA, Sigma-Aldrich), $Co(NO_3)_2$ (98%, Sigma-Aldrich), $FeCl_3$ (97%, Sigma-Aldrich) and/or $Ni(NO_3)_2 \cdot 6H_2O$ (99.9%, Sigma-Aldrich) as the precursors (Table 2). The precursors were dissolved in a 50/50 mixture of 2-propanol and deionized water (Milli-Q, Millipore Inc.). For metal

doping, different metal salts were added at the metal-to-5MR mass ratio of 1:20 (Table 2). The solution was dried at 35 °C for 48 h and the dry powder was pyrolyzed in N_2 flow at 800 °C with a ramping rate of 10 °C min^{-1} for 2 h. After cooling down to room temperature the carbon-based catalysts were collected. The as obtained materials are denoted as: MNC-OP (M = Ni, Fe, Co) [II and III].

For comparison, a metal-free material (NC-OP) was prepared by the same procedure, but without adding metal salts. Some of the metal-containing materials were acid-treated in a mixture of 0.5 M HNO_3 and 0.5 M H_2SO_4 at 50 °C for 8 h, washed with Milli-Q water, dried and pyrolyzed again at 800 °C for 2 h to obtain the FeNC-OP-at, CoNC-OP-at, and FeCoNC-OP-at catalysts [II].

Table 2. Amounts of the precursors used in the synthesis of the catalysts.

Catalyst	5MR (g)	DCDA (g)	Fe (mg)	Co (mg)	Ni (mg)
NC-OP [II]	0.1	1	-	-	-
CoNC-OP [II]	0.1	1	-	5	-
FeNC-OP [II]	0.1	1	5	-	-
FeCoNC-OP [II]	0.1	1	2.5	2.5	-
NiFeNC-OP [III]	0.1	1	1.67	-	3.33
NiFeNC-2-OP [III]	0.1	1	3.33	-	1.67
NiCoNC-OP [III]	0.1	1	-	1.67	3.33
NiFeCoNC-OP [III]	0.1	1	1.67	1.67	1.67

Note: Roman numerals in square brackets indicate original articles.

5.1.3 Synthesis of catalysts using magnesium-based templates

The electrocatalysts were prepared using Honeyol™ (VKG Oil AS, Estonia; an alkylresorcinol fraction consisting of 100% resorcinol derivates with a 5-methylresorcinol content of at least 48 wt.%) as the carbon precursor; dicyandiamide (DCDA, Sigma-Aldrich), $Fe(NO_3)_3 \cdot 9H_2O$ (97%, Sigma-Aldrich) and/or $Co(NO_3)_2 \cdot 6H_2O$ (98%, Sigma-Aldrich) as the nitrogen and transition metal precursors and $Mg(CH_3COO)_2 \cdot 4H_2O$ (98%, Alfa Aesar) as a precursor for MgO template. Honeyol and DCDA (mass ratio 1:10) were dissolved in a mixture of Milli-Q water (Millipore Inc.) and 2-propanol, followed by the addition of magnesium acetate, after which Fe nitrate or Fe and Co nitrates (with Fe:Co mass ratio of 7:3) were added to obtain a metal-to-Honeyol mass ratio of 1:20 (Table 3). The mixture was dried at 60 °C and the obtained powder was pyrolyzed in N_2 flow at 800 °C for 2 h, with a ramping rate of 10 °C min^{-1}. The products were dispersed in 1 M hydrochloric acid (Sigma-Aldrich) for 2 h at room temperature to dissolve the MgO template. The obtained carbon materials were filtered, washed with Milli-Q water, dried and pyrolyzed again at 800 °C for 1 h. The

resulting materials are given in Table 3 [IV]. Additionally, catalysts FeNC and FeCoNC were prepared without a template, but using the same procedure as a comparison.

For work [V], the same procedure was used. The materials were prepared using Honeyol, DCDA and iron nitrate or a combination of iron nitrate and manganese acetate were added to achieve a metal-to-Honeyol mass ratio of 1:20.

Table 3. Amounts of the precursors used in the synthesis of the catalysts.

Catalyst	Honeyol (g)	DCDA (g)	Fe (mg)	Co (mg)	Mn (mg)	Mg-acetate (g)
FeNC [IV and V]	0.2	2	10	-	-	-
FeNC-MgOAc [IV]	0.2	2	10	-	-	0.2
FeNC-MgOAc-2 [IV]	0.2	2	10	-	-	0.1
FeNC-MgOAc-3 [IV]	0.2	2	10	-	-	0.05
FeCoNC [IV]	0.2	2	7	3	-	-
FeCoNC-MgOAc [IV]	0.2	2	7	3	-	0.1
FeNC-T [V]	0.2	2	10	-	-	0.2
FeMnNC-T [V]	0.2	2	7	-	3	0.2

Note: Roman numerals in square brackets indicate original articles.

5.1.4 Ionothermal synthesis of catalysts

The materials were produced by using Honeyol™, a carbon precursor consisting of resorcinol derivatives with a 5-methylresorcinol content of at least 48 wt% (VKG Oil AS, Estonia). Honeyol was mixed together with $Mg(NO_3)_2{\cdot}6H_2O$ (98%, Alfa Aesar) using a pestle and mortar, with a mass ratio of Honeyol-to-$Mg(NO_3)_2$ of 1:1. The well-homogenized mixture was then transferred into a ceramic boat and pyrolysed in a nitrogen flow at 800 °C for 1 h with a ramping rate of 10 °C min^{-1}. During the pyrolysis the $Mg(NO_3)_2{\cdot}6H_2O$ acts as a solvent, porogen and nitrogen dopant. The in-situ formed MgO nanoparticles act as the sacrificial template and are removed after the pyrolysis by dispersing the resulting MgO@NC-LT material in a 1 M HCl (Sigma-Aldrich) solution for 2 h, at room temperature. The obtained carbon material (NC-LT) was thoroughly washed with Milli-Q water, filtered and dried overnight in an oven at 60 °C, followed by a final grinding.

In order to obtain the ORR-active electrocatalysts, ion-exchange reaction was used to replace Mg^{2+} in $Mg–N_x$ centers with Fe ions. The materials were dispersed in methanol, to which a certain amount of $FeCl_2{\cdot}4H_2O$ (97%, Sigma-Aldrich) was added to obtain a concentration of 2.5×10^{-2} M. The resulting mixture was refluxed under constant stirring for 24 h. The catalyst was then washed with Milli-Q water and dispersed in a 0.5 M H_2SO_4 solution overnight. The material was then washed with water, filtered, dried in an oven and pyrolyzed at 800 °C for

1 h with a ramping rate of 50 °C min^{-1}, to obtain the final catalyst denoted as FeNC-LT. As a comparison a catalyst was prepared with $FeCl_3$ (98%, Thermo Scientific) instead, denoted as FeNC-LT-$FeCl_3$.

5.2 Physical characterization of PGM-free catalysts

The scanning electron microscopy (SEM) samples were prepared by drop-coating a suspension of the catalyst material onto polished GC disks. The SEM analysis was conducted with Helios TM NanoLab 600 (FEI) microscope. The energy dispersive X-ray spectroscopy (EDS) detector INCA Energy 350 (Oxford Instruments) mounted on the microscope was used for elemental characterization.

For the high-resolution (scanning) transmission electron microscopy (HR-(S)TEM) the samples were deposited onto Lacey carbon supports on Cu 300 mesh grids (Agar Scientific). The TEM measurements were made with Titan 200 (FEI) microscope with accelerated voltage of 200 kV, in scanning mode with both bright field (BF) and high-angle annular dark field (HAADF) detectors. Elemental mapping was taken from the same area as HAADF images with EDS analyzer ChemiSTEM (FEI/Bruker).

For obtaining the N_2 adsorption/desorption isotherms, the materials were vacuum-dried for at least 24 h at 200 °C before the measurement. The measurement was done using NovaTouch LX2 instrument (Quantachrome) at the boiling point of nitrogen (77 K). Specific surface area (S_{BET}) was calculated with Brunauer-Emmett-Teller theory. The total pore volume (V_{tot}) was measured at the saturation pressure of N_2 (P/P_0 = 0.97). Pore size distribution (PSD) was calculated using quenched solid density functional theory (QSDFT) equilibria model for slit-type, slit-cylindrical or slit-cylindrical-spherical pores. All the calculations were done using TouchWin 1.11 software (Quantachrome Instruments).

The X-ray photoelectron spectroscopy (XPS) analysis was conducted at ultra-high vacuum conditions using a non-monochromatic twin anode X-ray tube (Thermo XR3E2) with the characteristic energy of 1253.6 eV (Mg K_α radiation) and an electron energy analyzer SCIENTA SES 100. The survey scan was measured in the energy range from 900 to 0 eV, pass energy of 200 eV, step size of 0.5 eV, step duration 0.2 s and number of scans 5. Detailed spectra were collected with the step size of 0.1 eV and step duration of 0.2 s, with the number of scans being at least 25. The data was processed with CasaXPS (version 2.3.17), during which the K_α and K_β satellites were removed. Gauss–Lorentz hybrid function (GL 70, Gauss 30 %, Lorentz 70 %) and blend of linear and Shirley-type backgrounds were used for peak fitting.

X-ray diffraction (XRD) measurements were performed on Bruker D8 Advance diffractometer with Ni filtered Cu Kα radiation. The diffraction patterns were obtained with scanning steps of 0.0126° 2θ in the range from 5° to 89° and the counting time of 525 s per step. The data was analyzed with Topas 6 (Bruker) software.

Micro-Raman spectra were recorded in the back-scattering geometry on an inVia Renishaw spectrometer in conjugation with a confocal microscope (Leica Microsystems CMS GmbH, Germany), 50x objective and an argon ion laser operated at 514.5 nm. All samples were suspended in water and drop-coated on to silicon substrates. To avoid thermal decomposition of the sample, the laser power density was minimized by decreasing the laser power and defocusing laser spot to about 15 μm. The Raman spectra were normalized to the intensity of the G band. The spectra were fitted following the five-peak model where G peak (~1580 cm^{-1}) corresponds to the ideal graphitic lattice; D1 (~1350 cm^{-1}) to disordered graphitic lattice-graphene layer edge; D2 (~1610 cm^{-1}) to disordered graphitic lattice; D3 (~1500 cm^{-1}) to amorphous carbon and D4 (~1200 cm^{-1}) to disordered graphitic lattice. The Peak Analyser software in OriginPro 9 was used for Raman spectra processing.

The transition metal content in the samples was determined by microwave plasma atomic emission spectroscopy (MP-AES) using Agilent 4210 MP-AES. 10 mg of the catalyst material was dissolved with Anton Paar Multiwave PRO microwave digestion system in NXF100 vessels (PTFE/TFM liner) in a mixture of 4 mL of HNO_3 and 2 mL of H_2O_2. The dissolved samples were digested at 230 °C and at pressures between 45-50 bar. After the dissolution process, the samples were diluted with 2% HNO_3 solution to obtain metal concentrations of around 5 mg/L and measured.

5.3 Electrochemical characterization of PGM-free catalysts

5.3.1 RDE and RRDE experiments

A glassy carbon (GC) electrode (GC20-SS, Tokai Carbon, Japan) with a geometric surface area of 0.196 cm^2 was used as the working electrode. To prepare the electrode it was polished using alumina slurries of 1 μm and 0.3 μm (Buehler). The catalyst powders (4 mg) were ultrasonically dispersed in a 1 mL mixture of 2-propanol and water (1:1 v/v) along with 20 μl Nafion® solution (5 wt.% in lower alcohols, Aldrich) to prepare the catalyst ink. The ink was then drop-coated on the glassy carbon working electrode to achieve a catalyst mass loading of 0.1 [II, III and IV], 0.2 [I, VI] or 0.8 [V] mg cm^{-2}. The same procedure was followed to coat the GC electrodes with a commercial Pt/C catalyst (20 wt.%, E-TEK) and RuO_2 (99.9%, Alfa Aesar) as reference catalysts, with loading of 0.2 mg cm^{-2}.The electrocatalytic ORR activity of the catalysts was investigated by steady-state measurement in O_2-saturated (99.999%, Linde) 0.1 M KOH [I, II, III, IV and VI] or 0.5 M H_2SO_4 [V] solution using the rotating disk electrode method. In work [III], OER measurements in 0.1 M KOH were also done. A continuous gas flow over the solution was retained during the experiments. The background current was registered in Ar-saturated (99.999%, Linde) solution and subtracted from the experimental currents of O_2 reduction. Inhibition of ORR by cyanide ions was

studied in 0.1 M KOH solution containing 10 mM NaCN. Electrochemical measurements were conducted in a 3-electrode glass cell with an Autolab potentiostat/galvanostat PGSTAT30 (Metrohm-Autolab, The Netherlands). Potentials were measured relative to a saturated calomel electrode (SCE) and a carbon rod served as the counter electrode. Potentials vs SCE were converted with respect to the reversible hydrogen electrode (RHE): in acidic 0.5 M H_2SO_4 solution $E_{RHE} = E_{SCE} + 0.258$ V and in alkaline 0.1 M KOH solution $E_{RHE} = E_{SCE} + 1.008$ V. The electrode rotation rate (ω) ranged from 360 to 3100 rpm, controlled by a CTV101 speed control unit connected to an EDI101 rotator (Radiometer). The RDE data was analyzed using the K-L equation (Eq. 9). In publications [III, IV and VI] electrochemical impedance spectroscopy (EIS) was performed to obtain the internal resistance value for the system in O_2-saturated 0.1 M KOH. *iR* correction was automatically applied to the ORR and OER data with Nova software. The durability of the catalyst materials was evaluated by cycling the potential in the range from 1.008 to 0.408 V [I,II] or from 1.008 to 0.608 V [III,IV,VI] in O_2-saturated 0.1 M KOH electrolyte solution for 1000 [I,III], 10000 [VI] or 15000 [II,IV] potential cycles; the RDE polarization curves were recorded before cycling and after a certain number of cycles. In publication [III], for the OER durability test the potential range from 1.008 to 1.708 V vs. RHE for 1000 cycles was used. In publication [V], the accelerated durability testing was conducted by potential cycling from 0.95 to 0.6 V vs RHE in O_2-saturated 0.5 M H_2SO_4 electrolyte solution for 10000 cycles. The potential scan rate (ν) during the cycling was 100 or 200 mV s^{-1}. For the rotating ring-disk electrode (RRDE) measurements, a MSRX speed controller and an AFMSRX rotator (Pine Research, USA) were utilized. The electrode setup consisted of a GC disc/Pt ring electrode (Pine Research, USA). The electrodes and ink were prepared identically to RDE experiments. The catalyst mass loading was 0.8 mg cm^{-2} with a GC disc geometric area of 0.164 cm^2. During the RRDE measurements the Pt ring electrode was maintained at a potential of 1.25 V vs RHE. Before conducting the ORR experiments, the Pt ring electrode was electrochemically cleaned by performing at least three cyclic voltammograms (CV)s in the potential range of 0.06–1.66 V vs RHE. The peroxide percentage yield ($\%H_2O_2$) and electron transfer number (n) were calculated by equations (10) and (11):

$$\%H_2O_2 = \frac{\frac{2I_r}{N}}{I_d + \frac{I_r}{N}} \times 100\% \quad (10)$$

$$n = \frac{4I_d}{I_d + \frac{I_r}{N}} \quad (11)$$

where I_d is the disk current, I_r is the ring current and N is the collection efficiency of the Pt ring (N=0.25, as determined by hexacyanoferrate(III) reduction reaction).

5.3.2 MEA construction and fuel cell tests

In publication [II], catalyst inks with the following composition were made for the cathode: 12.5 mg of the catalyst material was dispersed in 365 µL of Milli-Q water, 1350 µL of methanol and 28 µL of poly[2,2′-(2,2″,4,4″,6,6″-hexamethyl-p-terphenyl-3,3″-diyl)-5,5′-bibenzimidazole] (HMT-PMBI) ionomer solution (10 wt.% in methanol). For the anode commercial Pt-Ru/C catalyst (weight ratio 50:25:25, Alfa Aesar) was dispersed in 145 µL of Milli-Q water, 540 µL of methanol and 11 µL of HMT-PMBI ionomer solution (10 wt.% in methanol). The suspensions were sonicated for 1 h before coating the gas diffusion layers (GDL, Freudenberg H23C4) by pipetting in 200 µL aliquots. The final catalyst loadings were 2 mg cm^{-2} on the cathode and 0.6 mg cm^{-2} on the anode. Before testing the electrodes and HMT-PMBI membrane were soaked in 3 M KOH solution for 48 h. The MEAs were prepared by pressing the electrodes and membrane along with a silicone gasket into 5 cm^2 cell (Fuel Cell Technologies Inc., USA) using a torque of 7 Nm. The single-cell AEMFC performance tests were carried out with a Greenlight Fuel Cell Test Station (G40 Fuel Cell System, Hydrogenics, Canada) using humidified H_2 and O_2 gases (relative humidity 100%) at a flow rate of 0.1 NLPM at 60 °C and a backpressure of 200 kPa. In publication [IV] the anodes were made with PtRu/C catalyst (Alfa Aesar, 40% Pt and 20% Ru on carbon black, HiSPEC 10000). For the anodes, ~19 mg of powdered anion-exchange ionomer (AEI) consisting of cross-linked polystyrene functionalized with trimethylamine (Fumatech) was added to a mortar and ground for 3 min. Following the initial grind, 51 mg of PtRu/C was added to the mortar along with an additional 25 mg of carbon black (Vulcan XC-72) to increase the porosity and hydrophobicity of the catalyst layer and ultimately avoid flooding. One milliliter of deionized water and 9 mL of 2-propanol were added to the solid mixture and further ground for 10 min to create a low viscosity catalyst ink. The FeCoNC and FeCoNC-MgOAc cathode inks were prepared in a similar manner to the anode ink, wherein 12.75 mg of AEI were first added and ground, followed by adding 30 mg of each catalyst and 3.4 mg of Ultraflon MP-25 (FuelCellStore), to optimize the water management. Ten milliliters of total solvents were added to each mortar and ground for an additional 10 min to create low viscosity catalyst inks. For the Pt/C (20 wt.%) cathode ink, 13.2 mg of AEI, together with 15.7 mg of Pt/C catalyst (Alfa Aesar, 40% Pt on carbon black, HiSPEC 4000), 12.5 mg of additional carbon black (Vulcan XC-72), to increase the carbon loading to 80% and dilute the Pt loading to 20%, 3.3 mg of Ultraflon MP-25 and 10 mL of total solvents were used. To further compare the effect of the cathode catalyst layer thickness, an additional cathode ink was made using Pt/C (40 wt.%). The same amounts of AEI and Pt/C catalyst (Alfa Aesar, 40% Pt on carbon black, HiSPEC 4000) were used with no additional carbon black.The catalyst inks were sonicated for 1 h in an ice-cooled ultrasonic bath. Following sonication, the cathode inks were sprayed directly onto 5 cm^2 gas diffusion layers (Toray Carbon Paper 060 with Micro Porous Layer, FuelCellStore) with an Iwata HP-TH professional airbrush. The loadings for the FeCoNC and FeCoNC-MgOAc GDEs were 0.96

$mg_{catalyst}$ cm^{-2}, while the Pt/C GDEs were loaded to 0.97 mg_{Pt} cm^{-2} and 0.56 mg_{Pt} cm^{-2}, respectively. The anode ink was spray deposited onto a 25 cm^2 gas diffusion layer (Toray carbon paper, 060-TGP-H-060 with 5 wt.% PTFE wet proofing) with a 5 µm thick carbon microporous layer. Upon arriving at a PGM loading of 0.57 mg_{PtRu} cm^{-2}, the 25 cm^2 GDE was cut into four smaller 5 cm^2 GDEs. The thicknesses of the anode and cathode catalyst layers were determined by measuring the thickness of the GDEs in 5 different places with a Mitutoyo ABS Digital Thickness Gauge (Item number: 547-526S) and subtracting the average thickness of the pristine gas diffusion layers.The radiation-grafted LDPE-based anion-exchange membrane (Cl^- form ionic conductivity of ~63 mS cm^{-1}), were immersed in 1 M KOH for up to a week before testing. All electrodes were immersed in 1 M KOH aqueous solution for 1 h prior to cell assembly, with solution changes every 20 min. Three different AEMFCs were assembled between two 5 cm^2 single-serpentine graphite bipolar flow field plates with Teflon gaskets and torqued to 4.5 N m to achieve an average gas diffusion layer compression of 35%. The cells were tested under H_2/O_2 gas flows of 1 SLPM without back-pressurization in an 850E Scribner Associates Fuel Cell test station with cell temperature of 55 °C and anode and cathode dewpoints set at 44 and 45 °C, respectively. After acquiring the original polarization curves, the anode and cathode dewpoints were further optimized for the best performance. In publication [V], for the preparation of the cathode inks, 40 mg of a catalyst (FeNC, FeNC-T, or FeMnNC-T) was dispersed in a mixture of Milli-Q water (1 mL), 2-propanol (2 mL) and 0.52 mL of Nafion® ionomer solution (5 wt.%, Sigma-Aldrich) by sonication in an ice bath for 2 h. A commercial Pt/C catalyst (46.1 wt.% Pt, Tanaka Kikinzoku Kogyo K.K., Japan) was used to prepare anode electrode with the ionomer-to-catalyst (I/C) ratio of 1:1. To prepare the MEAs the anode catalyst ink was spray-coated with an airbrush (Paasche®, USA) on a GDL (BB-39, Sigracet) with a loading of 0.25 mg_{Pt} cm^{-2} and dried at 80 °C. Then, the anode GDE was hot-pressed (Carver, USA) with Nafion® NRE-211 membrane at 130 °C for 3 min at 0.3 metric-ton load. After cooling to room temperature, the cathode catalyst layer was spray-coated on the other side of the Nafion membrane until obtaining a cathode catalyst loading of 4.0 mg cm^{-2}. The prepared MEA was assembled along with a Sigracet BB-39 GDL in single cell (Fuel Cell Technologies Inc., USA). The fuel cell polarization curves were recorded using Greenlight Fuel Cell Test Station (G40 Fuel Cell System, Hydrogenics, Canada) at 80 °C and 2.0 bar backpressures on both the anode and cathode side. The flow rate of H_2 and O_2 gases (fully humidified) was 0.3 normal liter per minute (NLPM) in the PEMFC tests. In publication [VI], GDEs with active areas sizes of 5 cm^2 were used. To prepare the cathode, 10 mg of powdered AEI, a cross-linked polystyrene compound functionalized with trimethylamine (Fumatech), was first added to a mortar and ground for 3 minutes. Following that, 25 mg of FeNC-LT and ~10 mL of total solvents (1 mL of deionized water and up to 9 mL of 2-propanol) were added to the mortar containing the AEI, mixed and ground for an additional 10 min to create a low viscosity catalyst ink. A PtRu/C catalyst (Alfa Aesar, 40% Pt and 20% Ru on carbon black HiSPEC 10000) was employed as the catalyst to make the anode.

Approximately 19 mg of AEI, 51 mg of PtRu/C and an additional 25 mg of carbon black (Vulcan XC-72) were added to the mortar and ground in a 1:9 mL deionized water-to-2-propanol solvent ratio to create the ink. Both FeNC-LT and PtRu/C catalyst inks were transferred to individual 50 mL plastic centrifuge tubes and sonicated in an ice-cooled Grant XUBA3 ultrasonic bath at 100% intensity for one hour. Following sonication, the cathode ink was sprayed directly onto a 5 cm^2 GDL (FuelCellStore, Toray Carbon Paper 060 with Micro Porous Layer) with an Iwata HP-TH professional airbrush and dried at 140 ºC on a drying plate. The final loading of the FeNC-LT GDE was 0.89 $mg_{FeNC\text{-}LT}$ cm^{-2}. The anode ink was similarly spray deposited onto a 5 cm^2 GDL (FuelCellStore, Toray Carbon paper 060-TGP-H-060 with 20 wt.% PTFE wet proofing) to a PGM loading of 0.75 mg_{PtRu} cm^{-2}. Before cell assembly, the two GDEs and a 9 cm^2 piece of the FAA-3-05-RF AEM (polymer reinforced with porous ePTFE-film, 7 μm average fully hydrated thickness) were submerged in separate petri dishes containing 1 M KOH aqueous solution. The solution was changed every 20 min to ensure complete ion-exchange. Following the soaking process, the MEA was assembled between two 5 cm^2 single-serpentine graphite bipolar flow field plates with Teflon gaskets and torqued to 4.5 N m to achieve an average gas diffusion layer compression of 35%. The thicknesses of the anode, cathode and AEM were measured with a Mitutoyo ABS Digital Thickness Gauge (Item number: 547-526S) prior to cell assembly to determine the appropriate gaskets. The cell was tested in a Scribner Associates 850E Fuel Cell test station under H_2/O_2 gas flows of 0.5 SLPM at a cell temperature of 60 °C and anode and cathode dewpoints set at 55 and 57 °C, respectively.

6. RESULTS AND DISCUSSION

6.1 Catalysts derived from 5-methylresorcinol-formaldehyde resin

In the first part of the work, two sets of Fe- and Co-containing nitrogen-doped carbon materials were prepared from 5-methylresorcinol-formaldehyde (5MR-FA) resins and different catalyst doping methods are compared [I]. Firstly, carbon nanospheres (CNSs) were obtained by pyrolysis of 5MR-FA nanospheres. Then, the CNS were doped by pyrolyzing them in the presence of nitrogen and transition metal precursors. Another set of materials were prepared by in-situ doping, where the 5MR-FA nanospheres were combined with the precursors and pyrolyzed. The electrocatalytic ORR activity of these materials was characterized and compared.

6.1.1 Physical characterization of catalysts derived from 5MR-FA resin

The morphology of the materials was characterized by SEM (Figure 4). It is evident that the carbon nanospheres produced by the pyrolysis of 5MR-FA nanospheres remain spherical during the second pyrolysis in the presence of nitrogen and metal precursors. The structure of the N-doped carbon nanospheres (NCNS) and transition metal-containing N-doped CNSs (CoNCNS and FeNCNS) is similar, except that some carbon nanotubes (CNTs) were observed in Fe-containing material. It has been demonstrated earlier that Fe-containing seeds catalyse the formation of N-doped CNTs from nitrogen-containing precursors, including DCDA [122]. Based on the SEM images the size of CNSs is in the range of 90-160 nm. The metal content determined by EDS analysis was 1.1 wt.% in CoNCNS and 2.1 wt.% in FeNCNS.

The one-step in-situ synthesis approach, *i.e.* pyrolyzing the mixture of 5MR-FA resin nanospheres, DCDA, and Fe/Co salt, leads to the catalysts of completely different surface morphology (Figure 4d-f). Evidently, the spherical shape of the 5MR-FA precursor is not preserved in this synthesis method and porous carbon materials with irregular structures are formed. It has been suggested that DCDA may function as a cross-linking agent for the phenolic resin by reacting with formaldehyde that can evolve during the suspension of the mixture [123]. The loss of the structure has also been observed when polymer nanospheres were pyrolyzed in the presence of melamine and it was proposed to be due to the vigorous release of the reactive gaseous nitrogen species at high temperatures, which causes swelling of the semi-carbonized nanospheres and changing their pore structure [124]. As the ratio of DCDA to nanospheres is rather high in this work, both of these effects could be the reasons of losing the nanosphere structure. It has also been noted that when nanospheres of phenolic resin are prepared in the presence of DCDA as nitrogen precursor, the carbon nanospheres can only be obtained in case of low amounts of DCDA [125]. According to the EDS

analysis, metal content in CoNC-MRFA and FeNC-MRFA was 3.1 and 3.4 wt.%, respectively. Because the carbon is formed concurrently with the active sites by pyrolyzing a carbon precursor alongside nitrogen and metal sources, it generally allows for a higher concentration of active sites compared to the carbon doping method.

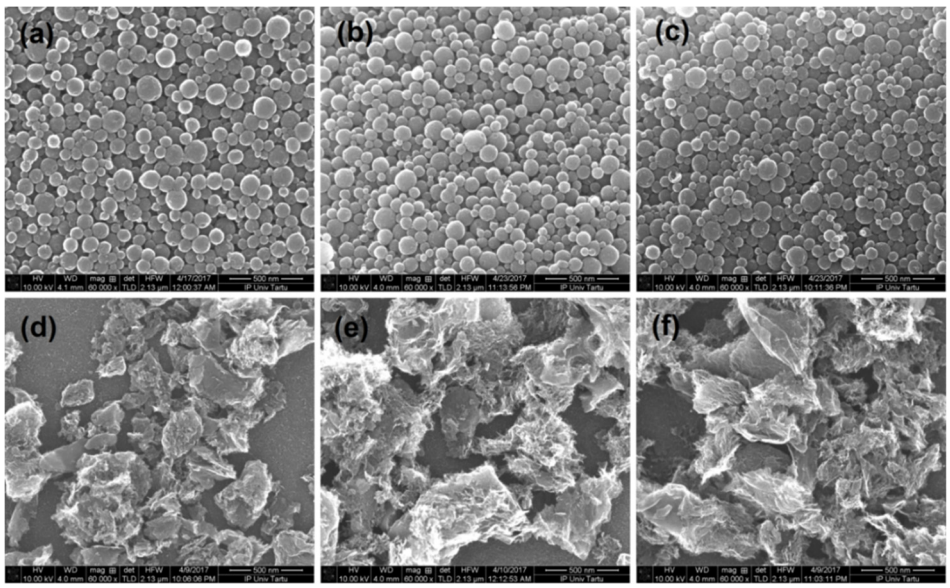

Figure 4. Scanning electron microscopy images of the catalysts: (a) NCNS; (b) CoNCNS; (c) FeNCNS; (d) NC-MRFA; (e) CoNC-MRFA and (f) FeNC-MRFA.

XPS analysis was employed to characterize the surface composition of the electrocatalysts. It is evident that the surface nitrogen content for metal-containing N-doped carbon nanospheres (2.4 at.%) is lower than that of corresponding non-spherical nanomaterials (8.2–8.7 at.%), suggesting that nitrogen doping is more efficient when it occurs simultaneously with carbonization of precursors, as compared to post-doping of carbon spheres (Table 4). The metal content on the surface is rather similar for both materials, being slightly higher in case of cobalt (1.6–1.9 at%) as compared to iron (0.8–1.0 at.%). It is also apparent that the N content is higher for metal-free N-doped materials. To determine the types of N species in the catalysts, the N1s peaks of the high-resolution XPS spectra were deconvoluted into up to five peaks with slightly different binding energies that correspond to pyridinic (398.8 eV), metal-coordinated ($M–N_x$, 399.8 eV), pyrrolic (400.7 eV), graphitic (401.8 eV) and oxidized N (N–O, 403.3 eV). It is evident that pyridinic N, which is often suggested to be one of the most active centres of ORR in N-doped catalysts [126], is the most prevalent nitrogen type in the materials prepared in this work.

Table 4. Surface elemental composition (at.%) and relative surface concentration of N species in the catalyst materials determined by XPS.

Catalyst	Surface elemental composition (at. %)				Relative surface concentration of N species (%)				
	C	Fe or Co	N	O	M–N_x	N–O	pyridinic	pyrrolic	graphitic
NCNS	81.8	-	13.8	4.4	-	8.6	50.0	32.6	8.9
CoNCNS	92.1	1.9	2.4	3.6	12.6	12.1	43.6	26.0	5.7
FeNCNS	92.6	0.8	2.4	4.1	20.8	9.4	42.5	21.6	5.7
NC-MRFA	83.7	-	11.9	4.4	-	6.2	42.3	51.5	-
CoNC-MRFA	85.3	1.6	8.7	4.3	12.6	8.4	41.8	31.8	5.5
FeNC-MRFA	86.8	1.0	8.2	4.0	14.3	7.6	43.0	30.3	4.6

The N_2 physisorption on the materials was studied to describe the porosity of the catalysts. According to IUPAC classification, type II isotherms with a H3 type hysteresis loop were observed (Figure 5a). From this data, the values of specific surface area (S_{BET}) were calculated to be about two times higher for CoNC-MRFA and FeNC-MRFA (214 and 237 $m^2\ g^{-1}$, respectively) than those of the spherical nanomaterials CoNCNS (132 $m^2\ g^{-1}$) and FeNCNS (112 $m^2\ g^{-1}$). Similarly, the total pore volume (V_p) for CoNC-MRFA and FeNC-MRFA was 0.60 $cm^3\ g^{-1}$, whereas for CoNCNS and FeNCNS it was 0.34 and 0.30 $cm^3\ g^{-1}$, respectively. The metal-free undoped and N-doped carbon nanospheres showed higher porosity, $S_{BET} = 453\ m^2\ g^{-1}$ for CNS and $S_{BET} = 421\ m^2\ g^{-1}$ for NCNS. Figure 5b illustrates the pore size distribution in the catalysts that show two maxima for spherical materials, one at about 3 nm and another between 10 and 15 nm. Presumably, the former corresponds to small pores in the nanosphere structure and the latter to the voids between the spheres. The main difference between metal-containing and metal-free CNS is that the latter also contain some micropores. The materials FeNC-MRFA and CoNC-MRFA have characteristic small mesopores with the size of about 4 nm, but also the larger mesopores of various sizes. The much higher porosity of the in-situ doped catalysts could expose more active sites to the electrolyte, thus increasing the electrocatalytic performance.

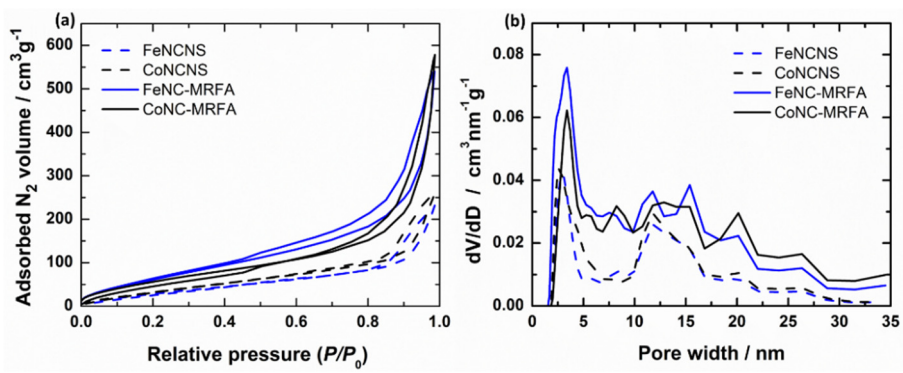

Figure 5. (a) N_2 adsorption isotherms and (b) pore size distribution for the catalysts.

6.1.2 Electrochemical characterization of catalysts derived from 5MR-FA resin

The electrocatalytic activity of the catalysts towards the ORR was studied in 0.1 M KOH solution. A comparison of the RDE polarization curves (Figure 6a) indicates that the ORR performance of the materials greatly depends on their composition, but also on the surface morphology. The undoped CNSs show the lowest ORR activity, the onset potential of O_2 reduction being 0.77 V (Table 5). This is somewhat increased for metal-free N-doped materials, as E_{onset}= 0.81 V for NC-MRFA and 0.84 V for NCNS. Fe- and Co-containing N-doped catalysts, however, show remarkably higher performance, both in terms of E_{onset} and half-wave potential ($E_{1/2}$). With the Co-doped material displaying the highest $E_{1/2}$ of 0.79 V. The most positive E_{onset} can be observed for FeNC-MRFA, however, as the current increase is steeper for CoNC-MRFA, the latter displays the most positive value of $E_{1/2}$. The value of $E_{1/2}$ is only 30 mV more negative for CoNC-MRFA than for 20% Pt/C catalyst. It can be concluded that cobalt-containing catalysts are slightly more active as compared to their iron-containing counterparts. Similarly, higher activity of Co-based materials as compared to Fe-containing catalysts has been observed in previous researches, for instance, for melamine-based carbon aerogels [127] and carbon-supported metal-aminopyrine derived electrocatalysts [128]. However, some other studies of non-precious metal catalysts report higher activity of Fe-containing materials as compared to Co-based catalysts [129,130]. Apparently, there are many factors that could contribute to the ORR activity of the catalysts. However, it is evident that the non-spherical metal-containing N-doped catalysts are more active as compared to those based on CNSs, displaying more positive values of E_{onset} and $E_{1/2}$. Higher activity of catalysts prepared via the in-situ doping can be related to their higher SD, as evidenced by the higher total N content. Additionally, the importance of the microstructure can be seen from these results, as the catalysts prepared via in-situ doping display a much higher surface area and more mesopores, potentially exposing more active sites to the electrolyte.

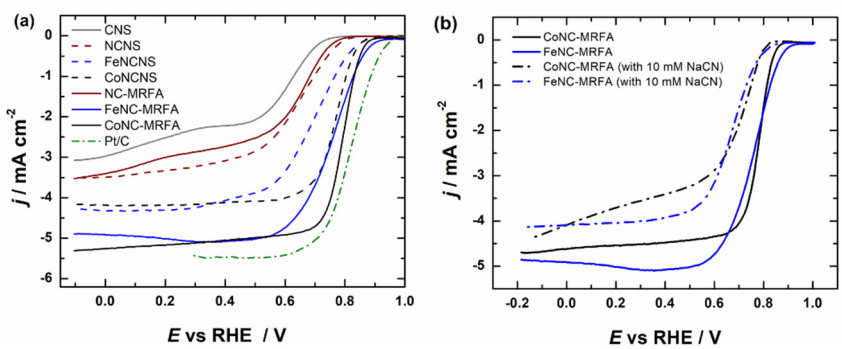

Figure 6. (a) RDE voltammetry curves for O_2 reduction on the catalysts in O_2-saturated 0.1 M KOH at 1900 rpm. v = 10 mV s^{-1}. (b) RDE voltammetry curves for O_2 reduction in the presence of 10 mM NaCN.

To study the ORR pathway in 0.1 M KOH solution for the catalyst materials, sets of ORR polarization curves at various electrode rotation rates were measured and analyzed by the K-L equation to obtain the *n* values (Table 5). The *n* value lower than 4 indicates that the ORR proceeds partly by $2e^-$ and partly by $4e^-$ route. The values of *n* between 3 and 4 were also observed for other metal-containing catalysts and these were slightly lower for Co-based materials as compared to Fe-containing catalysts. Similarly, higher *n* value, but lower activity of Fe-containing catalysts as compared to Co-containing materials has been observed in some other studies [127,128]. For the metal-free materials, the *n* values are still lower ($2<n<3$), as the two-electron pathway is more dominant.

Table 5. Kinetic parameters for O_2 reduction for the catalysts in 0.1 M KOH.

Catalyst	E_{onset} (V)	$E_{1/2}$ (V)	*n*
CNS	0.78	0.58	2.2 - 2.8
NCNS	0.84	0.64	2.4 - 2.5
CoNCNS	0.90	0.77	3.2 - 3.3
FeNCNS	0.89	0.69	3.6 - 3.8
NC-MRFA	0.81	0.62	2.1 - 3.0
CoNC-MRFA	0.90	0.79	3.2 - 3.6
FeNC-MRFA	0.92	0.76	3.8 - 4.0
Pt/C	0.98	0.82	3.9 - 4.0

Based on these results, it is evident that transition metals play a tremendous role in enhancing the ORR performance of the catalysts, as the metal-containing materials display considerably higher ORR activity, despite their lower total N content. The importance of nitrogen-coordinated metal ions as ORR-active centers has been highlighted in many studies, however, as mentioned in Sub-section 4.3.2, it has also been suggested that metal-rich nanoparticles encapsulated in carbon may contribute to the overall ORR activity. To assess the role of the N-coordinated Fe and Co in the ORR, the RDE experiments were carried out in the presence of NaCN in the electrolyte solution. It is well-known that the CN^- anions can strongly coordinate with surface transition metal centers and block these, which leads to inhibition of the ORR process [131,132]. The RDE data in Figure 6b clearly shows that the ORR performance remarkably decreases in the presence of CN^- for all metal-containing catalysts, the E_{onset} shifting negative by up to 120 mV. However, the ORR activity still remains higher as compared to that of the metal-free catalysts. This can be due to the effect of the metal to the structure and composition of the pyrolyzed materials. In addition, it suggests a possible contribution of carbon-encapsulated metal-containing nanoparticles to the ORR activity of the catalysts.

6.2 5-methylresorcinol-derived catalysts prepared via one-pot synthesis

From the first work it was concluded that the in-situ doping method yields catalysts with superior activity by increasing the SD due to the more efficient doping, and the 5MR-FA nanospherical structure is not maintained during this. As such, in the second part of the work the polymerization between 5-methylresorcinol and formaldehyde was not performed, and 5MR was directly used as the carbon precursor in the pyrolysis alongside with DCDA and Fe and/or Co salts. In this work the precursor ratios were optimized to obtain the highest electrocatalytic activity for ORR [II].

6.2.1 Physical characterization of 5MR-derived catalysts

Figure 7 shows the SEM micrographs of the catalyst materials prepared via the one-pot synthesis method. The findings indicate that a nanostructured morphology is effectively created during pyrolysis. It has been proposed that DCDA forms graphitic carbon nitride between 300–600 °C, which acts as a template during carbonization of organic precursors [133]. At higher temperatures, it decomposes into reactive gaseous nitrogen species that contribute both to the porosity and nitrogen-containing active centers in the final catalyst material [134,135]. Acid washing did not change the overall surface morphology of the catalysts as can be seen from Figure 7.

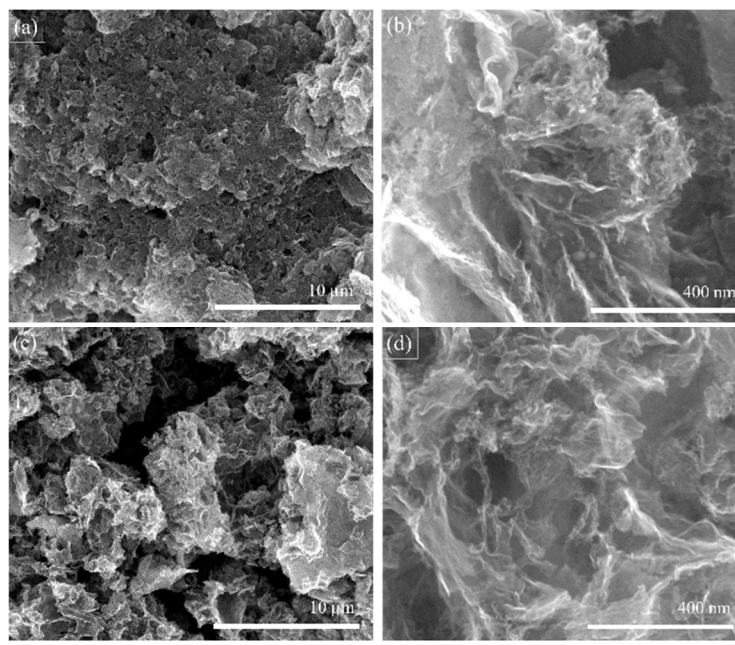

Figure 7. Scanning electron microscopy images of the FeCoNC-OP (a,b) and FeCoNC-OP-at (c,d) catalyst materials.

The STEM images of bimetallic catalysts (Figure 8a–b) show that both materials contain metal-rich nanoparticles with the size of about 5–20 nm that are rather evenly distributed on carbon support. Although it is expected that metal and metal oxide nanoparticles would dissolve during the acid treatment, this is not the case and there is no remarkable decrease in the number of particles. The reason for this is seen in HR-TEM images in Figures 8c, which demonstrate that metal nanoparticles are encapsulated in carbon shells with the variable thickness of about 5–15 graphitic layers. The formation of carbon-covered metallic nanoparticles in pyrolysis of such materials has been noted in several reports [102,136, 137]. As mentioned in Sub-section 4.3.2, while these sites have lower TOF value than M–N_x moieties, they can act as additional active sites increasing the SD and help to modulate the surrounding M–N_x centers boosting their activity. The elemental distribution of the materials is shown in the images of EDS mapping (Figure 8d–f), which reveal that N atoms are evenly distributed on the carbon material. As expected, Fe and Co are both present in nanoparticles, but also distributed all over the carbon support, presumably as M–N_x centers.

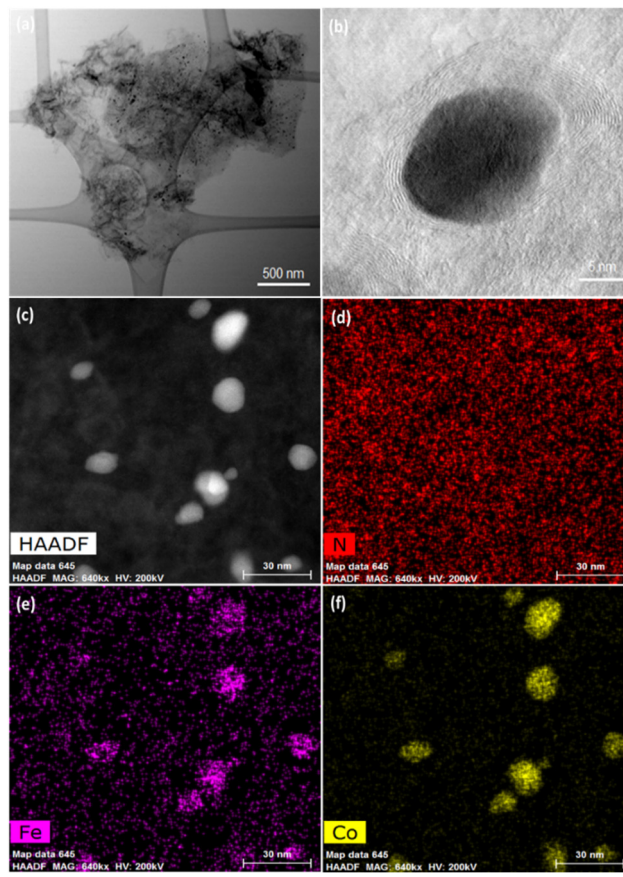

Figure 8. (a, b) TEM, (c) HAADF-STEM, and (d–f) EDS mapping images of FeCoNC-OP-at.

To determine the specific surface area and pore size distribution of the materials, N_2 physisorption on the catalyst samples was studied. Type III isotherms with a H3 type hysteresis loop, according to the IUPAC classification, were observed [II]. The materials are largely mesoporous with some microporosity, between 8–17% of the total pore volume (Table 6). Both Fe and Co doped catalysts have similar S_{BET} values, but the bimetallic material has a comparatively lower S_{BET}. Acid leaching had an observable effect on the S_{BET} and porosity of catalysts doped with one metal, with catalysts that were treated in acid possessing larger S_{BET} and V_{tot}. It is likely that during this process some metal particles that may have been blocking the pores were removed. Interestingly, acid treatment did not have a remarkable effect on the S_{BET} or porosity of the bimetallic material, which has a lower micropore volume compared to the other materials. The PSD curves (Figure 9a) show that the materials have many small mesopores (<5 nm), but also a rather continuous distribution of larger mesopores (<30 nm).

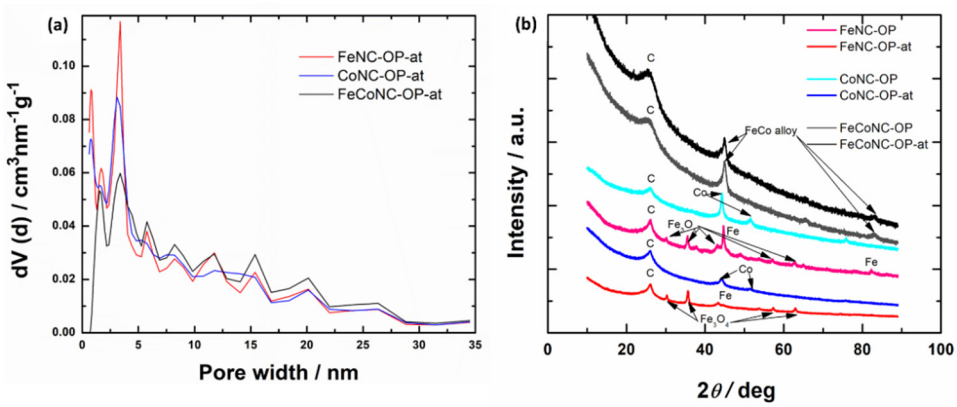

Figure 9. (a) Pore size distribution and (b) XRD patterns of the catalyst materials shown in the legend.

Table 6. Specific surface area (S_{BET}), total pore volume (V_{tot}), and micropore volume (V_{μ}) of the catalysts.

Sample	S_{BET} ($m^2\ g^{-1}$)	V_{tot} ($cm^3\ g^{-1}$)	V_{μ} ($cm^3\ g^{-1}$)
FeNC-OP	310	0.52	0.08
FeNC-OP -at	404	0.60	0.10
CoNC-OP	307	0.60	0.07
CoNC-OP-at	395	0.61	0.09
FeCoNC-OP	297	0.63	0.05
FeCoNC-OP-at	292	0.61	0.05

The crystallographic structure and composition of the catalyst materials was studied using the XRD analysis (Figure 9b). The wide, sharp-tipped peak at 26° (2θ) indicates a heterogeneous structure with both bigger and smaller bundles of graphite and structurally unlinked graphitic layers. The bimetallic material has a more homogenous structure. For Co-containing materials, the XRD analysis confirms the presence of metallic cobalt, with the crystallite size of 15.2±0.3 nm in CoNC-OP and 10.8±0.4 nm in CoNC-OP-at, as determined by Rietveld analysis. The FeNC-OP material contains both iron nanoparticles (crystallite size 28.5±1.0 nm) and Fe_3O_4 (23.9±1.0 nm). Most of the metal in the FeNC-OP-at is in oxide form, with crystallites of 22.6±0.6 nm in size. The bimetallic materials contain FeCo alloy, with the Fe-to-Co ratio of about 1:1 and the crystallite size of 12.0±0.3 and 15.5±0.8 nm for FeCoNC-OP and FeCoNC-OP-at, respectively. These values are in rather good agreement with the particle sizes estimated from the TEM images.

The results of the surface elemental composition of the catalyst materials determined by XPS analysis (Table 7, Figure 10) shows the presence of carbon, nitrogen, oxygen, iron and/or cobalt. Unsurprisingly, the surface metal content was higher for the untreated catalysts, since transition metal-containing nanoparticles that are not encapsulated in carbon are removed during acid leaching. A small decrease in N content with acid leaching and 2nd pyrolysis can also be observed for all materials. Interestingly, the total surface content of metals as well as nitrogen content is nearly twice as high in the bimetallic catalyst as compared to the FeNC-OP or CoNC-OP materials. To assess the presence of different N species in the catalysts, detailed N 1s spectra were deconvoluted into six subpeaks [II].

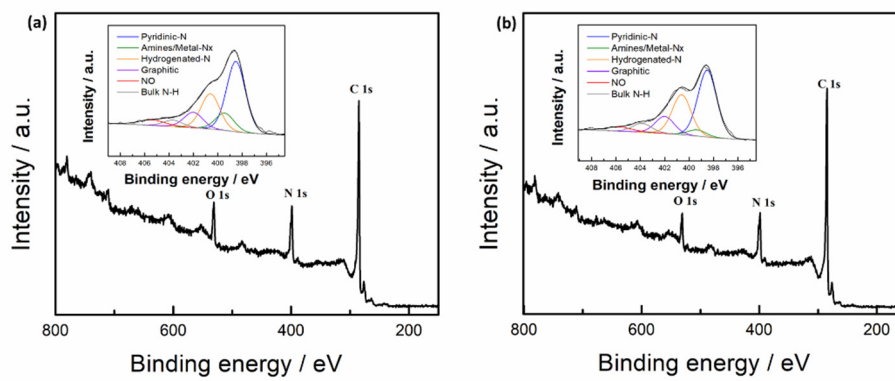

Figure 10. XPS survery spectra with the insets showing detailed N 1s spectra, for (a) FeCoNC-OP and (b) FeCoNC-OP-at

In all catalysts, pyridinic-N (at about 398.5 eV) is the most common surface N species. However, considerable amounts of hydrogenated-N (~400.5 eV, includes pyrrolic-N and hydrogenated pyridine), graphitic-N (~402.0 eV) and metal-co-

ordinated N ($M–N_x$, ~399.4 eV) were also detected. Graphitic-N and pyridinic-N species have been shown to play a key role in the ORR. It has been suggested that graphitic-N groups not only enhance the dissociation of O_2 molecules on the neighboring carbon atoms, but also promote the creation of strong chemical bonds between carbon and oxygen atoms, thus reducing the ORR activation energy [138]. High content of pyridinic-N is often correlated with high ORR activity [46,139]. However, some other studies have reported pyrrolic-N to be responsible for the activity [86,106,140]. The $M–N_x$ centers have been shown to provide the highest ORR activity of such catalysts, especially in acidic solution, but also in alkaline media [139,141]. Still, the chemical nature of nitrogen-containing active sites or which N-functionality is responsible for ORR activity, is as of yet not entirely clear [104]. The bulk transition metal content was determined by MP-AES (Table 7). The analysis revealed that although the metal content in FeNC-OP-at and CoNC-OP-at was significantly lower than that in non-acid treated materials, a rather high amount of transition metals remains in the catalyst. As the metal and metal oxide nanoparticles are expected to dissolve in acid, the remaining part should be either in the form of carbon-encapsulated nanoparticles or atomically dispersed metal centers in carbon structure. Most remarkably, the bulk metal content was least affected by acid treatment for the FeCoNC-OP material. This can be explained by the higher amount of the metal being incorporated into the material as atomically dispersed active sites, which could be the reason for increased ORR electrocatalytic activity of the FeCoNC-OP-at catalyst.

Table 7. Surface elemental composition of materials determined by XPS and bulk metal composition determined by MP-AES.

Catalyst	Surface elemental composition (at.%)					Bulk metal composition (wt.%)	
	C	O	N	Fe	Co	Fe	Co
FeNC-OP	83.3	7.3	8.9	0.5	-	15.0	-
FeNC-OP-at	88.0	5.9	5.8	0.3	-	9.8	-
CoNC-OP	82.7	6.4	9.9	-	1.2	-	20.1
CoNC-OP-at	86.7	4.4	8.2	-	0.8	-	10.0
FeCoNC-OP	72.8	7.3	17.3	1.0	1.6	7.7	8.8
FeCoNC-OP-at	77.4	5.4	15.2	0.7	1.3	5.7	7.7

The detailed 2p photoelectron spectra of Fe and Co [II] consist of multiple peaks corresponding to oxidized forms of the metals, which can be bulk oxides, but also nitrogen-coordinated metal. However, it is not possible to precisely identify these components, as there are probably several different overlapping metal states, consisting of multiple peaks due to multiplet splitting and charge transfer effects [69]. The surface of materials contains only a very low percentage of metallic Fe

and Co, which have slightly lower binding energies than oxidized metals (706.6 and 778.1 eV, respectively). The Raman spectra of the catalysts were normalized to the intensity of the G band [II]. The ratio of the integrated areas of D1 and G peaks I_{D1}/I_G was found to be between 1.5–1.7 for single metal catalysts, but much higher, 2.5–2.7 for bimetallic materials [II]. High width of D1 and G bands and high I_{D1}/I_G ratio both indicate that all six samples have highly amorphous carbon structures, as commonly observed for N-doped carbon materials. The apparent effect of decreasing graphitic lattice disorder is observed for all six samples after the acid treatment and second pyrolysis. This can be explained by increasing the graphitization of these materials during the second pyrolysis and removal of some N- and O-containing surface defects, as indicated by the XPS data (Table 7).

6.2.2. Electrochemical characterization of 5MR-derived catalysts

The main aim of this part of the work was to optimize the ratio of precursors in the catalyst synthesis in order to obtain the materials with highest ORR activity. The results showed that the presence of sufficiently high amount of metal precursor as well as DCDA is necessary to obtain highly active materials [II]. Presumably DCDA exerts a role in both creating optimal nanostructure during pyrolysis, as well as increasing the amount accessible active sites in the catalysts. DCDA forms a layered graphitic carbon nitride template (g–C_3N_4) during the annealing [142]. Li et al. proposed that g-C_3N_4 template then binds with the aromatic carbon intermediates through donor-acceptor interactions; as the temperature rises the carbon nitride decomposes and the final nanocarbon material is obtained [133]. From these results, the materials prepared using the 5MR-to-DCDA ratio of 1:10 and metal-to-5MR ratio of 1:20 were selected for further studies. In addition, the effect of acid treatment on these catalysts was studied. Comparison of the RDE polarization curves of the ORR on the catalyst materials before and after acid treatment [II] reveal that the electrocatalytic performance of the materials is slightly improved by acid leaching. The higher activity likely results from the removal of inactive metal species that may be blocking the pores, thus increasing the amount of accessible active sites. The partial removal of metal during acid treatment is also confirmed by MP-AES analysis (Table 7).

After the synthesis conditions were optimized the role of different transition metals on the ORR activity was studied. We also investigated the potential of a bimetallic catalyst, combining the advantages of both single-metal sites. Comparison ORR activity of these catalysts is given in Figure 11a and Table 8 and compared against a commercial Pt/C catalyst. The onset potential for both FeNC-OP-at and CoNC-OP-at is slightly more negative than that of Pt/C, however the bimetallic FeCoNC-OP-at material shows comparable activity to the Pt-based catalyst with similar ORR onset and half-wave potentials. The K-L plots were used to obtain the *n* value for the catalysts (Table 8 and Figure 11b). The Co-doped catalysts displayed a relatively lower *n* value, while the Fe- and FeCo-containing catalysts had an *n* value close to 4.

Table 8. Kinetic parameters for O_2 reduction on the catalysts in 0.1 M KOH.

Catalyst	E_{onset} (V)	$E_{1/2}$ (V)	n at 0.6 V
FeNC-OP	0.92	0.78	-
CoNC-OP	0.92	0.79	-
FeCoNC-OP	0.92	0.80	-
FeNC-OP-at	0.92	0.80	3.8
CoNC-OP-at	0.92	0.80	3.6
FeCoNC-OP-at	0.94	0.83	4.0
Pt/C	0.96	0.83	4.0

Many other groups have also reported bimetallic catalysts to show better ORR performance than catalysts doped with a single metal [129,143,144]. This can be attributed to a synergistic effect of Fe–N_4 and Co–N_4 centers, as indicated by density-functional theory (DFT) calculations [145]. The calculations have suggested that pre-adsorption of $^{\bullet}$OH boosts the ORR activity of N-coordinated dual metal sites and the lowest ORR overpotential among dual metal sites was predicted for $FeCoN_6$(OH) centers [146]. It is not possible to confirm based on our data if the dual metal sites exist in FeCoNC-OP-at material, but it is evident from the XPS measurements that both metals are present on the surface and are at least partly coordinated to N atoms. However, the higher ORR activity of bimetallic material as compared to both single-metal counterparts can also be explained by the considerably higher total metal and nitrogen contents on the surface, as indicated by XPS analysis (Table 7), which suggests that the amount of the ORR-active centers in this electrocatalyst could also be higher. The Co-doped catalysts show slightly more positive $E_{1/2}$ values compared to Fe-doped catalysts. This implies that both the amount and nature of the M–N_x moieties have a direct impact on determining the overall activity of ORR electrocatalysts. However, there can be other factors at play, for example, metal particles encapsulated in graphitic layers can also be active centers for ORR by modifying the electronic properties of the surface carbon layer [70]. These centers are very sensitive to the thickness of the surrounding carbon shell, which means that the activity of these can be hugely varied depending on the synthesis procedure used [70]. In addition, it has been demonstrated that if the carbon shell is rather thick, then the ORR activity of the materials is mostly related to M–N_x centers and metal nanoparticles encapsulated in nitrogen-doped carbon layers are much less active [147]. It is clear that the final ORR electrocatalytic activity of the catalysts depends on a multitude of aspects in the catalysts structure and composition and possible synergistic effects make the rational design of the catalysts even more complicated. Thus, it is expected that further fine-tuning of the synthesis process and varying the amounts of precursors could allow to further improve the electrocatalytic activity of the materials.

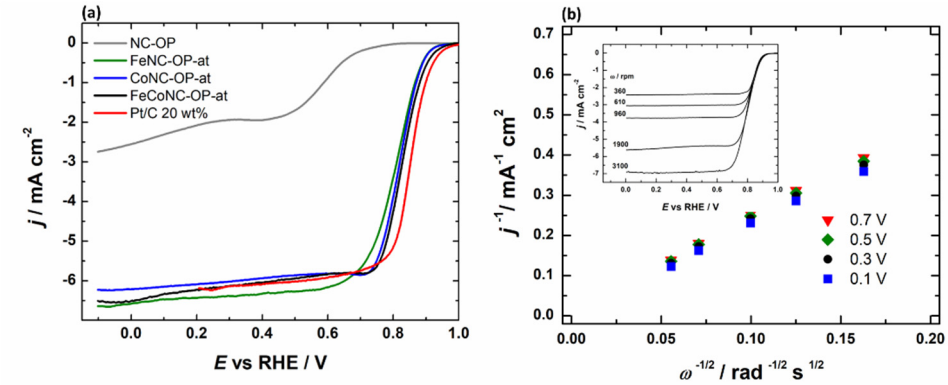

Figure 11. (a) RDE voltammetry curves for O_2 reduction on various catalysts in O_2-saturated 0.1 M KOH at 1900 rpm, and (b) K–L plots for FeCoNC-OP-at with the inset showing RDE voltammetry curves for O_2 reduction at different rotation rates.

Stability of the catalysts is of major concern from practical applicability point of view. There are several explanations for the loss of stability, for example the loss of metallic ions in active sites or the generation of H_2O_2 that may oxidatively degrade the catalyst [148]. In order to test the stability, the catalysts were subjected for 15000 potential cycles between 1 and 0.6 V vs. RHE. Figure 12a shows the RDE results of the FeCoNC-OP-at catalyst before and after the potential cycling. The E_{onset} values for all catalysts were slightly shifted toward more negative potential; by 20 mV for FeNC-OP-at, CoNC-OP-at and 35 mV for FeCoNC-OP-at. For FeCoNC-OP-at and CoNC-OP-at the $E_{1/2}$ value shifted by 20 mV after 15,000 cycles, whereas FeNC-OP-at was less stable ($\Delta E_{1/2}$ = 50 mV). The superior stability of Co-based catalysts could be due to Co–N_x moieties generating less reactive oxygen species through subsequent reactions with H_2O_2 [149]. In general, all the catalysts studied in this work showed high stability after 15000 potential cycles.

In order to further confirm the importance of M–N_x moieties in ORR electrocatalysis, the RDE experiments were also carried out in the presence of CN^- anions, which strongly coordinate to these centers and block them [150]. For all catalysts, the ORR performance decreased in the presence of CN^- anions, as their $E_{1/2}$ value shifted by 60 mV to a more negative potential (Figure 12b). This indicates that the high ORR activity of these materials is largely related to M–N_x centers and by blocking these, the remaining activity can be attributed to metal-free N centers and metal nanoparticles. M–N_x are suggested to be the active sites for ORR in acidic as well as in alkaline solution [151]. However, there are also many examples of metal-free N-doped carbons showing high ORR activity and various N functionalities, such as pyridinic and graphitic N have been proposed as active sites [104]. In addition, it has been reported that metal-containing nanoparticles encapsulated in N-doped carbon enhance the activity of N centers [137,152]. Thus, although the electrocatalytic activity of metal-containing catalysts in the presence of CN^- is still considerably higher as compared to metal-free

catalyst material (NC-OP in Figure 11), it does not necessarily imply that this is due to the direct role of metal not incorporated in M–N_x centers, i.e. metal-containing nanoparticles. It is expected that the presence of transition metal during the pyrolysis has a strong effect on the resulting catalysts morphology, which may also positively affect their ORR performance.

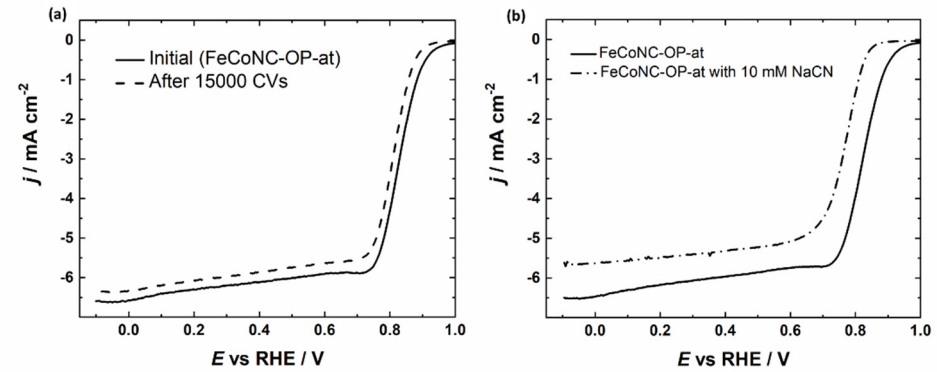

Figure 12. (a) RDE voltammetry curves before and after 15,000 potential cycles for FeCoNC-OP-at and (b) RDE voltammetry curves for O_2 reduction in 0.1 M KOH in the presence of 10 mM NaCN.

6.2.3. AEMFC results of 5MR-derived catalysts

To evaluate the practical applicability of the catalysts, fuel cell tests in a single-cell AEMFC were carried out, using FeCoNC-OP-at and commercial Pt-Ru/C as the cathode and anode catalysts, respectively (Figure 13). A maximum power density (P_{max}) of 415 mW cm^{-2} and current density of 170 mA cm^{-2} at 0.8 V were obtained. The maximum power density obtained in this work with FeCoNC-OP-at as the cathode catalysts is mediocre among Fe–Co based bimetallic electrocatalyst (Table 1). However, it is difficult to directly compare the fuel cell performance due to the large differences in experimental procedures. Most significantly, water management is of critical importance to obtain high performing AEMFC, but the balance between membrane hydration and catalyst flooding is very delicate and may be further affected by the backpressure [66,153]. In addition, the cell components, especially the anion exchange membrane, can have a huge impact on the overall AEMFC performance. The key properties of the membrane influencing water management are ionic conductivity and water diffusivity [154]. In this work HMT–PMBI was used as the AEM because of its favorable properties, especially high ionic conductivity and water permeability [155]. Furthermore, it has been shown that improved methods of ink preparation to optimize catalyst layer porosity and the use of thinner membranes are all important to obtain high maximum power densities [66]. Thus, it is expected that further optimization of the experimental procedures, including MEA preparation and water management, could lead to even higher AEMFC performance.

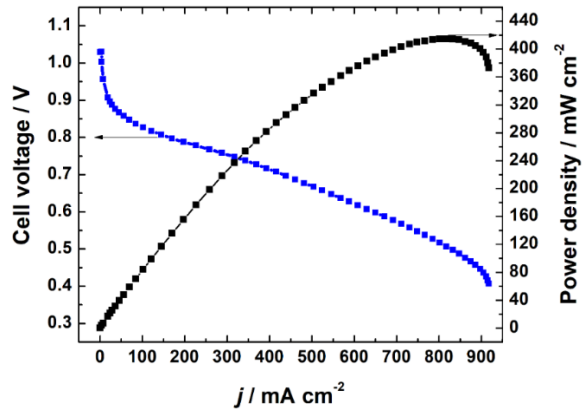

Figure 13. AEMFC polarization and power density curves with FeCoNC-OP-at cathode catalyst. 60 °C, 2 bar backpressure and H_2 and O_2 (fully humidified) flow rate 0.1 NLPM.

6.3 5-methylresorcinol-derived bifunctional catalysts

As a continuation of the work described in previous section, the possibility of preparing bifunctional ORR and OER electrocatalysts using the already optimized synthesis procedure was investigated [III]. These bifunctional catalysts can be used in rechargeable metal-air batteries. However, since Fe and Co doped catalysts show little activity towards OER, Ni was introduced into the catalyst materials, since it is well known that FeNi-based catalysts are considered the best option for water splitting. It is shown that by modifying the morphology and composition ratio of Fe–Ni alloy catalysts, their bifunctional activity can be significantly enhanced.

6.3.1 Physical characterization of bifunctional catalysts

The bifunctional catalysts were investigated by SEM. Similar to publication [II] the results indicate that pyrolysis of 5MR, DCDA and metal salt precursors yields unoriented sheet-like carbon structures (Figure 14a). To further observe the morphology and element distribution of the NiFeCoNC-OP catalyst material, TEM was used. The HAADF image (Figure 14b) shows that the trimetallic material contains metal-rich nanoparticles sized between 10–30 nm. EDS mapping images (Figure 14c-f) reveal homogeneous dispersion of N, Ni, Co and Fe elements throughout the entire material, verifying the uniform doping and dispersion of active sites. It is also revealed that the metal nanoparticles in Figure 14b consist of all three metals, most likely an alloy. FeNi-based catalysts are generally considered to be the best option for OER due to their low cost and high performance [156].

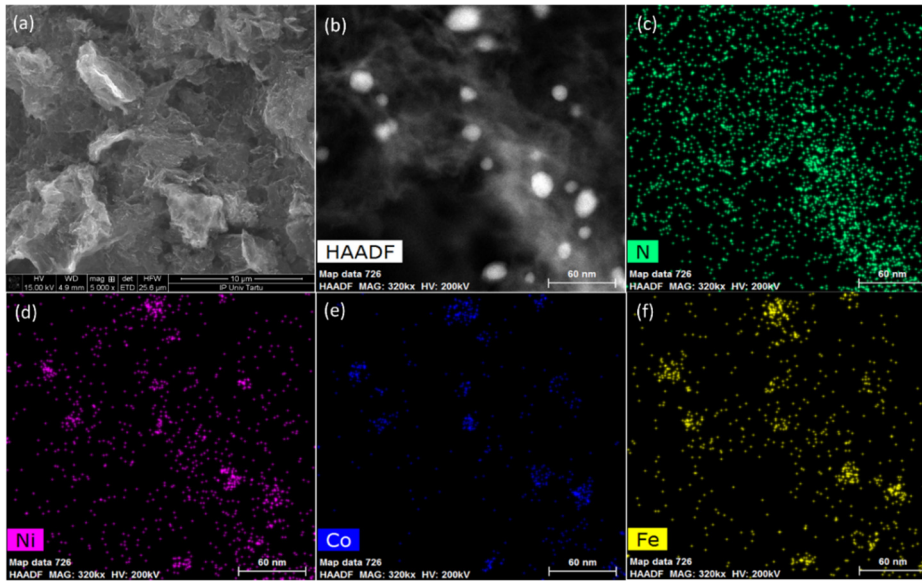

Figure 14. Electron microscopy images of NiFeCoNC: (a) SEM image, (b) HAADF image and (c–f) EDS elemental maps from the same area.

Micro-Raman spectra of the catalysts are presented in Figure 15a, where carbon D and G bands at 1350 and 1586 cm^{-1}, respectively, are observed. The I_D/I_G ratios, where I_D and I_G are integrated areas under the bands, were between 1.5–2.3 [III], indicating disordered and defective graphitic structures [157]. Specifically, for NiFeCoNC-OP the I_D/I_G ratio is 2.3, suggesting that the carbon contains a high number of structural defects, which could be active sites for ORR.

XRD patterns of the catalyst materials exhibit wide diffraction peak at approximately 26°(2θ) (Figure 15b), corresponding to graphitic carbon with the average crystallite size (perpendicular to graphitic layers) of about 2 nm. The rest of the peaks can be indexed to metal alloys, Ni (in NiFeNC-OP) and Fe_2NiO_4 (in NiFeNC-2-OP). The crystallite size of the metal alloys varies between 8 and 29 nm, but the exact composition of alloys cannot be determined from these XRD data. The bulk transition metal (Ni, Fe and Co) content was determined by MP-AES (Table 9). The total metal content in the catalyst materials varies between 13–24 wt.%, being higher than the surface metal content as determined by XPS. Similar results were obtained by SEM-EDS analysis [III]. This suggest that only part of the metal is located in $M–N_x$ sites on the surface, while the remaining is in the form of metal nanoparticles, which may be encapsulated in N-doped carbon sheets that have been shown to improve the electrocatalytic ORR and especially the OER activity [143,158].

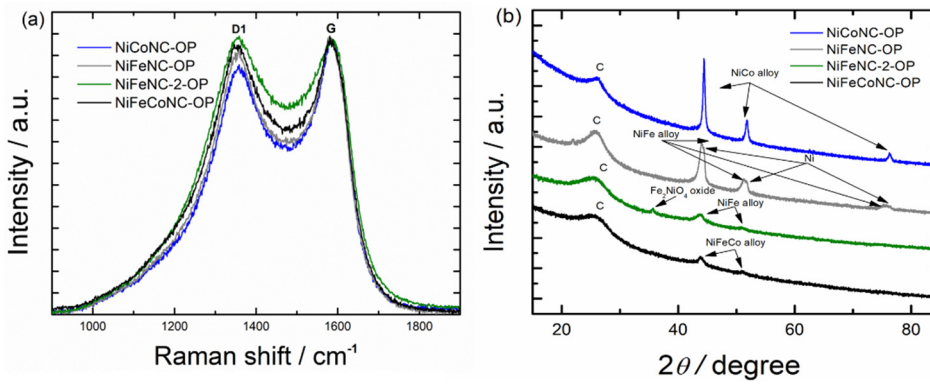

Figure 15. (a) Raman spectra and (b) XRD patterns of the catalyst materials shown in the legend.

Table 9. Bulk metal composition (wt.%) of catalyst samples as determined by MP-AES.

Catalyst	Ni	Fe	Co
NiCoNC-OP	16.73	0.06	8.14
NiFeNC-OP	12.99	5.82	-
NiFeNC-2-OP	4.25	9.02	0.06
NiFeCoNC-OP	4.71	4.80	4.81

6.3.2 Electrochemical characterization of bifunctional catalysts

Bifunctional electrocatalysts as oxygen electrodes in rechargeable metal-air batteries should efficiently catalyze both the oxygen reduction and evolution reactions. The complication is that active ORR catalysts do not necessarily show good electrocatalytic activity toward the OER and vice versa, since the reactions are catalyzed by different active sites.

The ORR and OER electrocatalytic performance of metal-containing N-doped catalysts was evaluated in O_2-saturated 0.1 M KOH and the applicability of bifunctional electrocatalysts was expressed as the potential gap $\Delta E = E_{j10}-E_{1/2}$, where E_{j10} is the potential at j_{OER} = 10 mA cm^{-2}. Figure 16a shows the ORR polarization curves of bi- and trimetallic catalysts prepared using various contents of metal salts. The Ni-containing bimetallic materials display moderate ORR activity, but their performance decreases with increasing Ni content, as can be seen from a comparison of NiFeNC-OP (Ni:Fe = 2:1 by weight) and NiFeNC-2-OP (Ni:Fe = 1:2) materials (Table 10), implying that the ratio of metals in the catalyst has a significant effect on the ORR activity; similar results were obtained by Serov et al. [159]. Among all the prepared materials, NiFeCoNC-OP exhibits the best ORR electrocatalytic activity with $E_{1/2}$ of 0.84 V, nearly reaching that of the commercial Pt/C catalyst ($E_{1/2}$ = 0.85 V). As a comparison, single-metal catalysts were also prepared and tested [III]. From these, FeNC-OP and CoNC-

OP exhibited reasonable ORR activity with similar E_{onset} of 0.93 V vs. RHE and $E_{1/2}$ of 0.82 V, and as expected, NiNC-OP was less active ($E_{1/2}$ = 0.77 V).

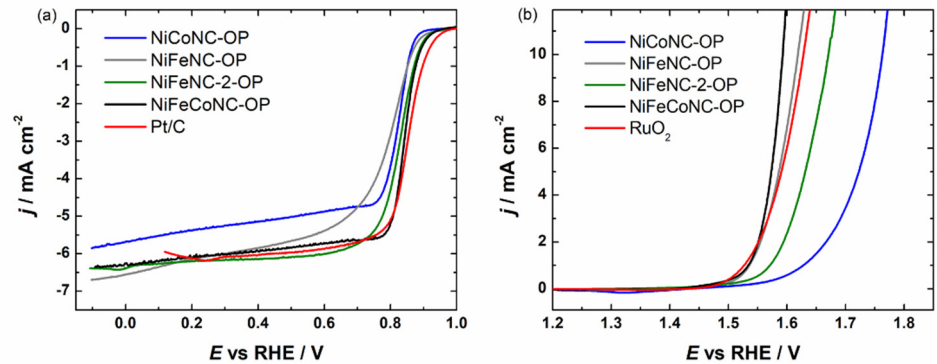

Figure 16. Comparison of RDE voltammetry curves for (a) O_2 reduction and (b) O_2 evolution on various catalysts in O_2-saturated 0.1 M KOH at 1900 rpm. ν = 10 mV s^{-1}.

Table 10. Kinetic parameters for O_2 reduction and evolution for the catalysts.

Catalyst	$E_{1/2}$ (V)	E_{j10} (V)	ΔE (V)
FeNC-OP	0.82	1.75	0.93
CoNC-OP	0.82	1.74	0.93
NiNC-OP	0.77	1.71	0.94
NiCoNC-OP	0.82	1.77	0.95
NiFeNC-OP	0.78	1.62	0.84
NiFeNC-2-OP	0.83	1.67	0.84
NiFeCoNC-OP	0.84	1.59	0.75

The OER activity of various catalysts was also evaluated (Figure 16b). Similar to ORR, the mono-metallic catalysts display lower electrocatalytic activity [III]. A high OER overpotential on FeNC-OP could be explained by the strong adsorption of OER intermediates on the Fe–N_x centers, causing a high activation barrier [160]. The OER performance can be significantly enhanced by incorporation of additional metals. Studies indicate that the coexistence of Fe and Ni can dramatically enhance the OER activity by affecting the electronic structure of the active sites, leading to a reduced activation energy [161]. Indeed, E_{j10} = 1.67 V was obtained with NiFeNC-2-OP catalyst that has the Ni:Fe mass ratio of ca 1:2, while for NiFeNC-OP (Ni:Fe = 2:1) the E_{j10} reaches 1.62 V. The NiFeCoNC-OP catalyst containing all three metals exhibits the best OER activity (E_{j10} = 1.59 V), outperforming the benchmark RuO_2 catalyst (E_{j10} = 1.63 V). NiFeNC-2-OP shows good activity towards the ORR, but the catalyst has relatively poor activity for OER (ΔE = 0.84 V). The opposite is true for NiFeNC-OP (ΔE = 0.84 V),

while NiCoNC-OP has low activity for both reactions (ΔE = 0.95 V). The trimetallic NiFeCoNC displays the best bifunctional activity (ΔE = 0.75 V). Similar results were obtained by Mao et al. with bimetallic catalysts, which generally outperformed monometallic catalysts and the trimetallic electrocatalyst consisting of Ni, Fe and Co showed the highest electrocatalytic activity [162]. Still, the role of each metal in multi-metallic catalysts as well as their synergistic effects are as of yet unclear. Presumably, different components adopt separate key functionality needed for OER and it is this synergy that provides the optimal performance for OER.

The stability of NiFeCoNC-OP was assessed through continuous potential cycling and only a negligible decay in $E_{1/2}$ for ORR is detected after 1000 potential cycles between 1.0 and 0.6 V (Figure 17). On the other hand, the value of E_{j10} experienced a drop of 30 mV after only 1000 CVs between 1.0 and 1.7 V. It is generally accepted that carbon-based catalysts are more unstable at positive potentials due to the highly oxidative conditions that causes significant carbon corrosion and demetallation [163]. While the catalysts show good stability for ORR, the decrease in activity after only 1000 cycles at positive potentials required for efficient OER is too large for any practical application (i.e. in metal-air battery). Thus, further research is needed to increase the durability of these catalyst materials.

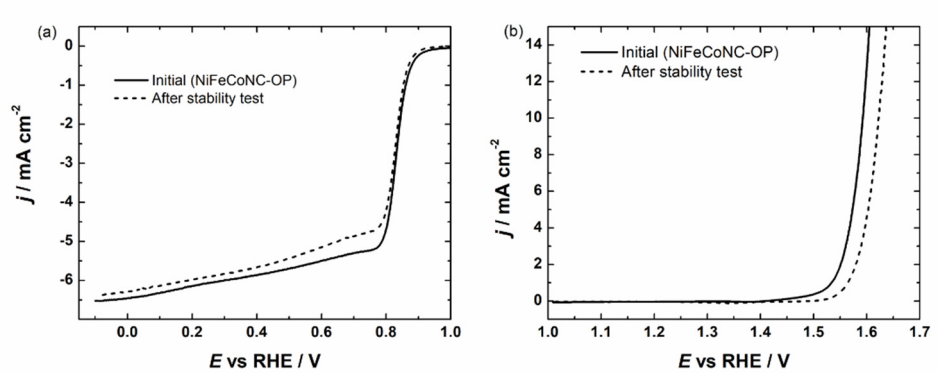

Figure 17. (a) RDE voltammetry curves for O_2 reduction on a NiFeCoNC-OP catalyst before and after 1000 potential cycles and (b) RDE voltammetry curves for O_2 evolution on a NiFeCoNC-OP catalyst before and after 1000 potential cycles. Test conditions: 0.1 M KOH at 1900 rpm, ν = 10 mV s^{-1}.

6.4 Catalysts prepared using magnesium-based templates

In the fourth part of the work, the effect of tuning the catalysts nanostructure by using magnesium-based sacrificial template was investigated [IV and V]. The catalysts were doped with iron or using a combination of Fe-Co or Fe-Mn. Mn was added to improve the durability of the PGM-free catalyst in highly oxidative environments, such as in PEM fuel cells. The addition of the Mg-based template

in catalyst preparation modifies the nanostructure of the catalyst and significantly increases the electrocatalytic performance in fuel cells, thanks to the increased surface area that exposes more active sites and mesoporous structure that allows for more efficient reactant transport through the catalyst layer. The catalysts prepared in the presence of template showed over twice higher maximum power densities in both AEM and PEM fuel cells than non-templated catalysts.

6.4.1 Physical characterization of templated catalysts

The catalysts prepared with Mg-based templates display a layered heterogenous sheet-like morphology, as can be seen from the SEM image in Figure 18a. DCDA serves a dual purpose in the synthesis procedure, acting as the structure directing agent and as the nitrogen dopant. During the pyrolysis between 300–600 °C, DCDA undergoes polymerization forming layers of graphitic carbon nitride (g–C_3N_4) [164]. The carbon precursors will be trapped between these layers. As the temperature increases, g-C_3N_4 decomposes into reactive gaseous nitrogen species, introducing nitrogen into the carbon framework formed [134]. When the template precursor Mg acetate is also present, the preparation process is accompanied by the decomposition of acetate and the evolution of gases. Prior work published by Inagaki's group revealed that acetate is fully decomposed into MgO nanoparticles, whereas other salts such as gluconate or citrate become additional sources of carbon [118]. The SEM images (Figure 18a and [IV, V]) reveal that there are no noticeable differences in morphology between the materials prepared with and without the Mg acetate.

TEM was used to examine the morphology and elemental distribution of the catalyst materials in greater detail. Elemental EDS mapping images (Figures 18d-e, [IV]) indicate homogenous dispersion of N and O elements throughout the material, verifying successful doping. From Figure 18d, e, it is apparent that the transition metals are evenly distributed over the carbon support, presumably as M–N_x centers; however, some metal-rich nanoparticles sized between 5 and 20 nm can also be seen in the HAADF image (Figure 18c). The bimetallic material prepared without the template, FeCoNC, displays far fewer nanoparticles [IV]. It is also revealed that the metal nanoparticles in bimetallic catalysts consist of both iron and cobalt and are encapsulated in graphitic carbon shells (Figure 18b). Such nanoparticles have been noticed in several reports and are thought to be electrocatalytically active toward ORR in alkaline media [137,165]. No large particles containing Mg were found; nonetheless, about 1 wt.% of magnesium is still left in the material even after the acid washing procedure. It has been shown that Mg can also form M–N_x sites, which cannot be removed during the acid washing step [107].

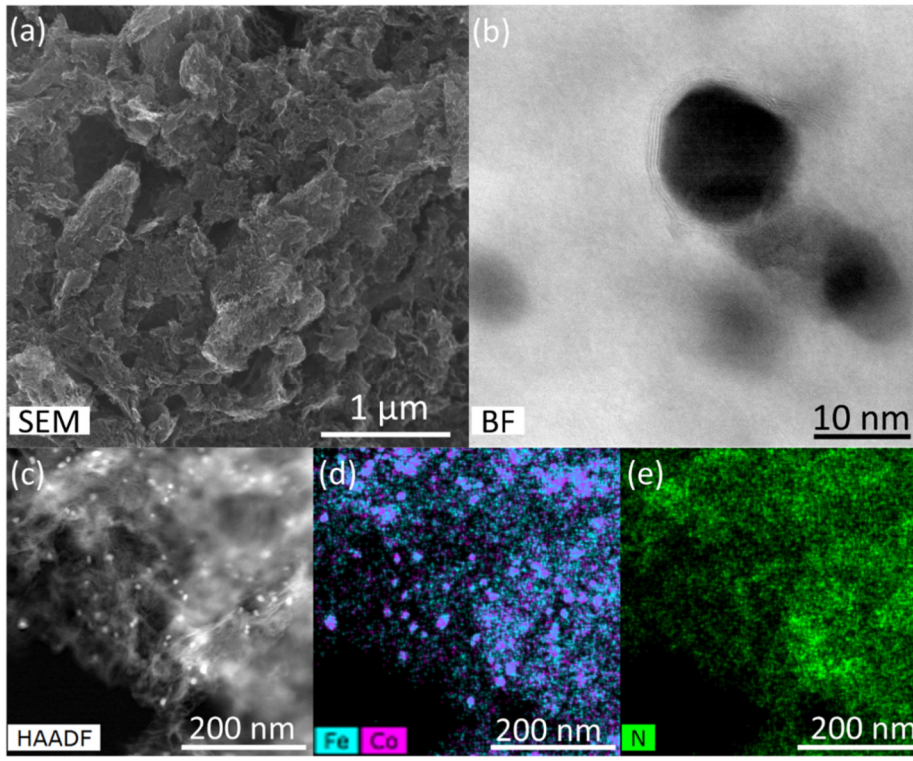

Figure 18. (a) SEM image, (b) STEM BF image, (c) HAADF-STEM, and (d,e) EDS mapping images of FeCoNC-MgOAc.

Similar conclusions were reached in work [V], where TEM images reveal the presence of metal-rich nanoparticles ranging in size from a few nanometers up to approximately 25 nm. Similar to FeCo-doped materials, these nanoparticles are encapsulated in graphitic carbon shells [V]. The addition of manganese helps to prevent agglomeration as the FeMnNC-T catalyst seems to contain less large iron particles compared to FeNC-T. Further EDS mapping images (Figure 19) provide evidence for the existence of finely dispersed metal sites in the carbon structure, possibly as atomically dispersed M–N_x centers (Figure 19b and f). Similar to FeCo-containing catalysts, no large particles containing magnesium were found, but residual amounts of Mg are present in the material even after undergoing the acid washing procedure (Figure 19c and g).

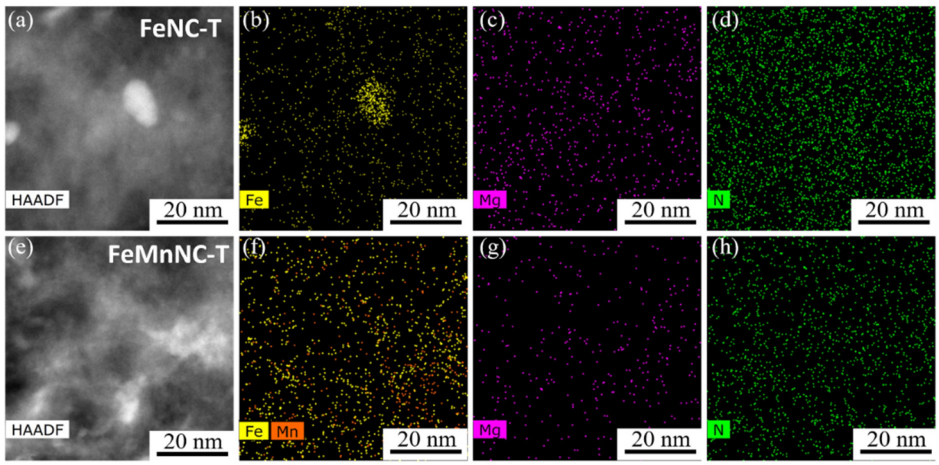

Figure 19. (a, e) HAADF-STEM images and (b, c, d, f, g, h) EDS mapping images of (a-d) FeNC-T, and (e-h) FeMnNC-T catalysts.

The specific surface area and pore size distribution were determined by N_2 physisorption analysis. Type III isotherms with an H3 type hysteresis loop were observed for all the catalysts (Figure 20b). The materials are predominantly mesoporous with a fairly wide pore size distribution (Figure 20a), due to g–C_3N_4 that acts as the structure directing agent, as well as the gradually released gases from thermal decomposition of g-C_3N_4 [164]. The addition of Mg acetate significantly increases the surface area of the materials obtained. During pyrolysis at around 200 °C, $Mg(CH_3COO)_2$ is decomposed to give nanosized particles of MgO and $MgCN_2$ [118]. As the temperature increases, the carbonizing phase covers the nanoparticles as a thin layer. The Mg-based template is dissolved after the pyrolysis to create additional mesoporosity. It has been noted that the morphology of the materials can vary remarkably depending on the synthesis conditions, nature of MgO precursor and carbon precursor/Mg precursor mass ratio [118, 166]. The catalysts prepared without templates have the smallest S_{BET} and V_{tot} and the surface area increases by increasing the amount of Mg acetate (Table 11). The addition of Mg-based templates seems to mainly increase the number of micropores and small mesopores with a diameter of 3–4 nm; however, some larger mesopores, in the range of 5-15 nm, are also created (Figure 20a). Such hierarchical porosity facilitates the mass-transfer of reactants to the active sites, enhancing the overall reaction rate [141]. This leads to an increase in the proportion of electrochemically available active sites, further improving the ORR activity of the catalyst. For oxygen and water to be effectively transported in the cathode layer, macropores are also necessary, however, the presence of these cannot be detected using nitrogen physisorption analysis due to the upper limit of detection of around 50 nm for this method.

Table 11. Specific surface area (S_{BET}), total pore volume (V_{tot}), and micropore volume (V_{μ}) of the catalysts**.**

Catalyst	S_{BET} (m^2 g^{-1})	V_{tot} (cm^3 g^{-1})	V_{μ} (cm^3 g^{-1})
FeNC	334	0.69	0.07
FeNC-MgOAc	561	0.91	0.13
FeCoNC	320	0.81	0.05
FeCoNC-MgOAc	505	0.87	0.11
FeNC-T	720	1.08	0.17
FeMnNC-T	694	0.99	0.16

The crystallographic structure and composition of the catalyst materials were studied using XRD analysis (Figure 20c). The XRD patterns depict a wide, sharp-tipped peak at 26° (2θ) characteristic of a disordered heterogenous carbon structure. Consistent with TEM results, the bimetallic catalyst FeCoNC-MgOAc has peaks that can be indexed to CoFe alloy (PDF 01-071-5029). The iron-doped catalysts display peaks indexed to Fe-carbide (PDF 00-034-0001) that completely cover the Fe peak (PDF 04-007-9753). As can be seen in Figure 20c, in the case of the non-acid treated material, the diffraction peaks for magnesium cyanamide (PDF 04-007-7389) and MgO (PDF 00-045-0946) phase appear, with a crystallite size of 4–5 nm obtained from the integrated width of the peaks, both of which are assumed to be responsible for the increased porosity of the materials. It has been observed in the literature that in the presence of an inorganic templating agent and a nitrogen source like melamine or DCDA, certain inorganic nanoparticles like cyanamides or carbides that act as graphitization catalysts are formed in situ [167,168]. However, magnesium cyanamide and oxide phases are not detected in acid-washed materials, evidencing the effective removal of the cyanamide and MgO nanoparticles. The patterns reveal that before the acid treatment step there can be some crystalline manganese species present, but it is impossible to confirm the exact phase, as the peaks corresponding to different carbide phases (Mn, Fe) and the alloys of the two metals all overlap. However, in good accordance with STEM-EDS mapping images, no agglomerated crystalline phases of manganese were observed after acid-treatment.

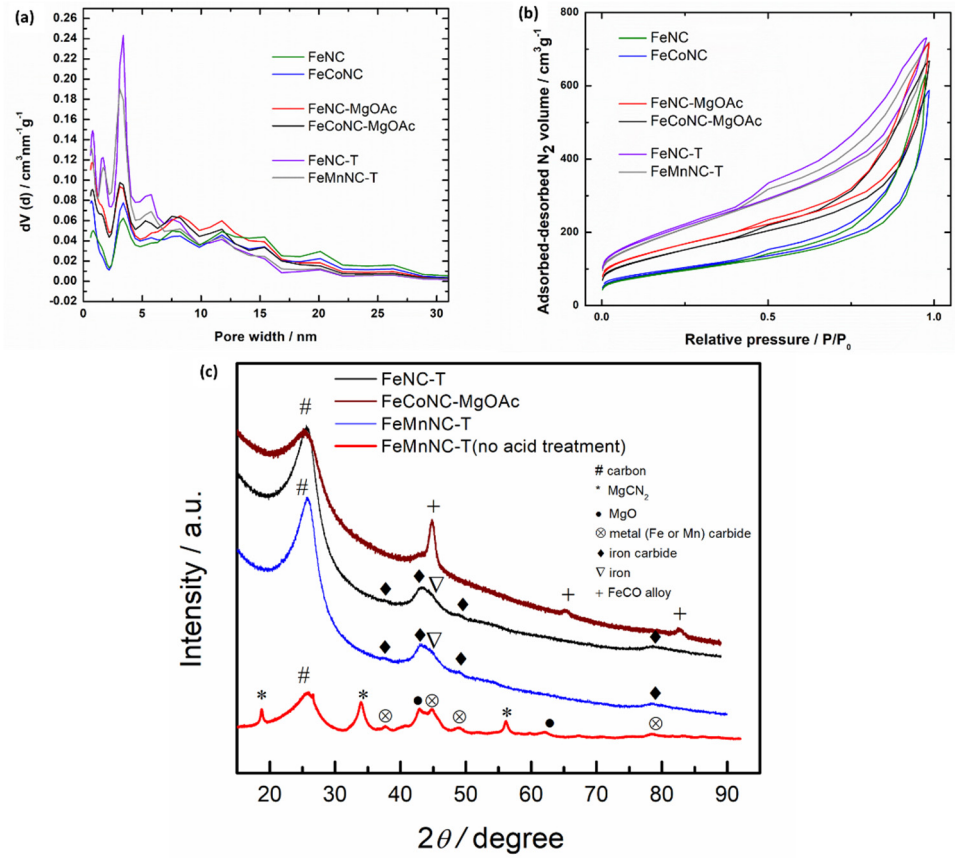

Figure 20. (a) Pore size distribution, (b) N_2 adsorption-desorption isotherms, and (c) XRD patterns of the catalyst materials.

The XPS analysis was performed to determine the surface elemental composition of the catalyst materials (Figures 21a, b and Table 12). Carbon, nitrogen, oxygen, iron, and cobalt were found on the surface of the catalysts. The oxygen content was similar in all the materials; however, the nitrogen amount was almost twice as high in bimetallic FeCo-containing catalysts as compared to Fe and FeMn-containing materials, with the highest being 20 at.% in FeCoNC. The deconvoluted N 1s spectra are displayed in insets of Figures 21a, b. Pyridinic nitrogen (~398.5 eV) is the most common surface species for all the catalysts, followed by hydrogenated nitrogen (~400.5 eV, combination of hydrogenated pyridine and pyrrolic-N). Substantial amounts of graphitic-N (~402.0 eV) and metal-coordinated nitrogen (M–N_x, ~399.4 eV) were also discovered. It is thought that nitrogen atoms provide electrons to carbon's π-orbital, which can then be transferred to O_2 π*-orbital, enabling O=O bond splitting and enhancing the ORR kinetics [169,170]. Even though nitrogen moieties are generally considered not to be very ORR-active in acidic media, it has been shown that highly basic N-groups can enhance the TOF value of nearby M–N_x sites [171,172].

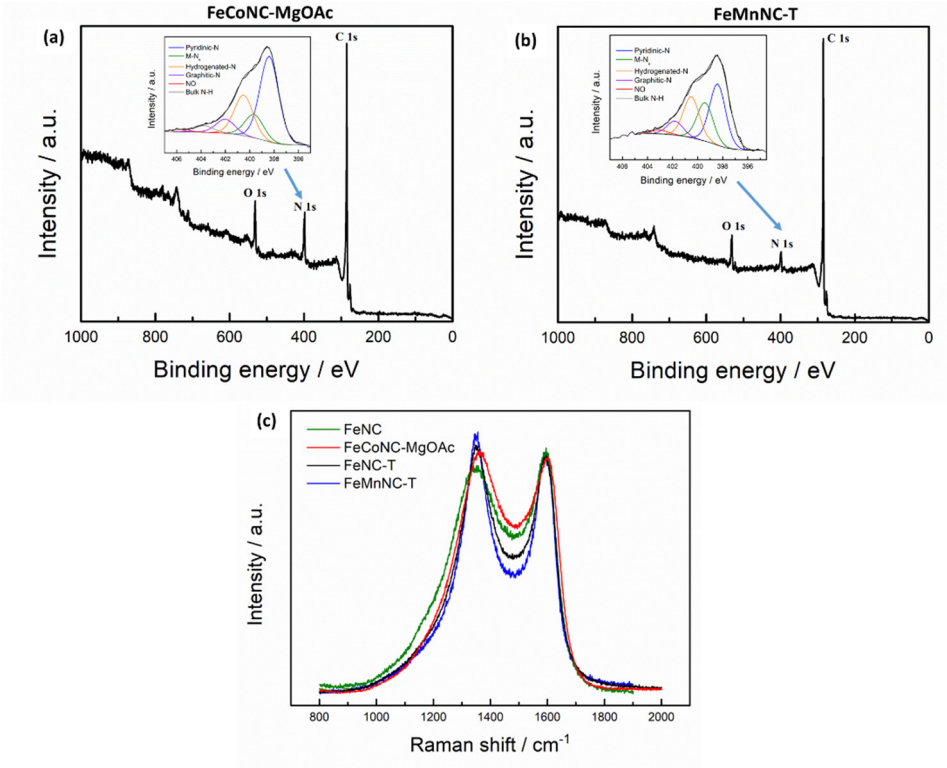

Figure 21. XPS survey spectra of (a) FeCoNC-MgOAc and (b) FeMnNC-T catalysts, with the insets showing detailed N 1s XPS spectra, and (c) Raman spectra of various catalysts.

The first-order Raman spectra of the catalysts normalized to the intensity of the G band are presented in Figure 21c. The widths of the G and especially D_1 band are qualitative measures of structural disorder for defective carbon materials. It can be concluded that all the catalysts are highly disordered, consistent with the XRD results. However, it is apparent that the catalysts prepared with the addition of Mg acetate have a discernibly higher degree of graphitization. The inclusion of manganese seems to exhibit a higher ability to promote the graphitization of carbon. Similar findings have been previously published [95,141], as such using Mn to achieve a higher degree of graphitization represents a promising avenue for designing PGM-free catalysts with improved durability. Previous studies have demonstrated that a higher degree of graphitization is advantageous for ORR catalysts by improving carbon corrosion resistance [173]. Unlike in Pt/C catalysts, where carbon material primarily functions as a conductive support, carbon in PGM-free catalysts directly interacts with and supports the active sites. If the carbon material undergoes corrosion or degradation, it can have severe consequences for the performance of the catalyst via the separation of the M–N_x sites from the carbon planes, resulting in the loss of electrocatalytic activity [141].

Therefore, a highly graphitized carbon support can enhance the overall stability of the catalyst, but it may come at the expense of reducing the number of defects available for anchoring the M–N_x sites. Achieving a balance between the density of active sites and the graphitization degree of the carbon support is essential for optimizing the catalyst performance [141].

Table 12. Surface elemental composition (at.%) of catalysts from the XPS data.

Catalyst	C	N	O	Fe	Co	Mn
FeNC-MgOAc	87.1	5.9	6.8	0.2	-	-
FeCoNC	69.4	19.9	8.9	0.6	1.1	-
FeCoNC-MgOAc	79.5	11.3	8.1	0.4	0.6	-
FeNC-T	85.0	7.3	7.7	0.3	-	-
FeMnNC-T	88.3	5.0	6.2	0.3	-	0.2

SEM-EDS and MP-AES were used to determine the elemental composition of the various catalyst materials [IV and V]. The metal content is around 5–8 wt.% for all catalysts. The high iron and cobalt concentration lead to formation of agglomerated species, i.e. iron carbide, iron and iron-cobalt alloy nanoparticles in addition to atomically dispersed M–N_x sites. These sites form during high-temperature treatment; first the iron precursor is reduced to form iron nanoparticles, which can then further react with the carbon forming iron carbide (carbothermal reduction). During this the carbon structure is recrystallized resulting in the loss of heteroatoms and formation of additional tetrapyridinic Fe–N_4 sites [101]. Around 1 wt.% of Mg is detected in the templated materials, indicating that some Mg is likely in the form of Mg–N_x moieties that are not removed via acid treatment.

6.4.2 Electrochemical characterization of templated catalysts

RDE was used for the initial evaluation of electrocatalytic activity of the nanocarbon-based catalysts toward the ORR in an aqueous 0.1 M KOH and 0.5 M H_2SO_4 electrolyte. The LSVs of the various catalysts are displayed in Figure 22 and Table 13. To find the optimal amount of Mg acetate, catalysts with different precursor ratios were prepared. The highest ORR activity in alkaline solution was achieved with a catalyst prepared using Honeyol to Mg acetate mass ratio of 2:1. The catalysts with a smaller or larger ratio displayed more negative $E_{1/2}$ values, although still superior to the non-templated catalyst [IV]. In acidic media, however, the optimal mass ratio of Honeyol to Mg acetate was 1:1 [V].

Table 13. Kinetic parameters of O_2 reduction of the catalysts in 0.1 M KOH* or 0.5 M H_2SO_4^.

Catalyst	$E_{1/2}$ (V)	n at 0.4 V
FeNC*	0.82	4.1
FeNC-MgOAc*	0.84	4.1
FeCoNC*	0.84	4.0
FeCoNC-MgOAc*	0.87	4.0
FeNC^	0.74	3.8
FeNC-T^	0.75	3.8
FeMnNC-T^	0.75	3.9

In alkaline conditions, the bimetallic FeCoNC-MgOAc catalyst displayed a higher electrocatalytic activity compared to only Fe-doped catalysts, equivalent to the benchmark Pt/C electrocatalyst (Figure 22a). For comparison, catalyst materials without any template precursors were prepared. The non-templated catalyst FeNC displayed a comparatively lower electrocatalytic activity toward ORR, exhibiting an $E_{1/2}$ value of 0.82 V vs. RHE. The bimetallic catalyst FeCoNC showed slightly higher activity, with a more positive $E_{1/2}$ of 0.84 V.

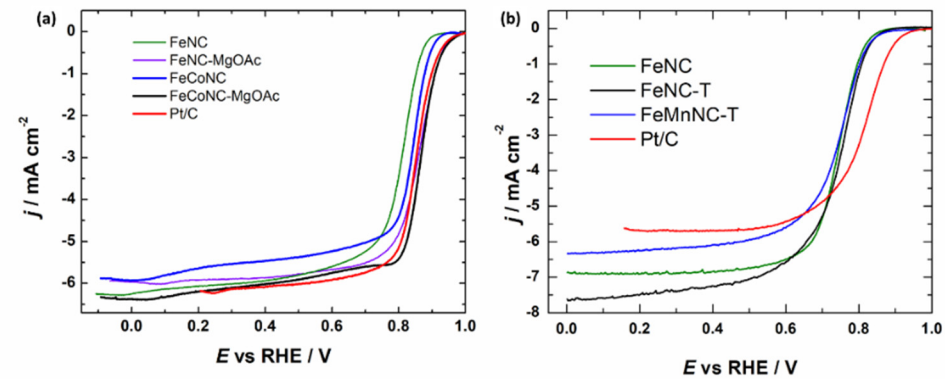

Figure 22. Comparison of RDE voltammetry curves for ORR on various PGM-free catalysts and commercial Pt/C in (a) O_2-saturated 0.1 M KOH solution and (b) O_2-saturated 0.5 M H_2SO_4 solution at 1900 rpm. ν = 10 mV s^{-1}.

The further improved ORR activity of the catalysts created with the Mg-based template could be explained by the higher mesoporosity, leading to increased exposure to electrocatalytically active sites [151]. From the RDE results it is obvious that the bimetallic catalysts show an improvement in electrocatalytic activity, compared to monometallic Fe-doped catalysts, with FeCoNC-MgOAc displaying an $E_{1/2}$ value of 0.87 V. Multi-metal site catalysts are generally agreed to be more active toward ORR [174,175]. It is believed that dual metal doping can increase catalyst performance by altering the electronic structure of active

sites and lowering the O–O cleavage barrier during the ORR process [145]. Although the exact mechanism is as of yet unclear, it is likely dependent on multiple factors such as the electron affinity, the radius of embedded transition metal atoms, heteroatom dopants, and local carbon defects [151]. Some research has also suggested that in addition to M–N_x sites, metal nanoparticles can greatly improve the ORR performance. For example, Peng et al. [176] found that introducing cobalt and iron nanoparticles into nitrogen-doped carbonaceous matrix boosted electrocatalytic activity, implying a synergistic effect between metal nanoparticles and nitrogen-doped carbon. While both bimetallic catalysts include M–N_x sites on the surface, FeCo alloy nanoparticles are more prevalent in FeCoNC-MgOAc, according to the XRD and TEM results, which can be another explanation of higher ORR electrocatalytic activity of this catalyst.

In acidic medium, all of the electrocatalysts prepared in this work displayed similar ORR activities when comparing their E_{onset} and $E_{1/2}$ [V]. FeNC-T and FeMnNC-T achieved the $E_{1/2}$ value of 0.75 V vs. RHE, which is 67 mV lower than that of a commercial Pt/C catalyst. Despite the much higher bulk metal content of the FeNC catalyst (8.1 wt.%), the ORR activity remained very similar, which suggests that a large part of the iron is not coordinated to nitrogen and is susceptible to agglomeration into nanoparticles during the thermal treatment. The number of electrons transferred per O_2 molecule for the iron-containing catalysts during the ORR process is about 3.8, obtained from the K-L analysis of RDE data [V]. The bimetallic FeMnNC-T has a slightly higher *n* value (3.9). A significant issue with FeNC catalysts is the occurrence of Fenton reactions between Fe^{2+} ions and hydrogen peroxide. The oxygen-containing radicals generated through the Fenton processes can cause the degradation of organic components, such as ionomers and membranes, and even the catalysts themselves [177]. When comparing the peroxide yields determined by RRDE method (Figure 23), it is observed that the solely iron-doped carbon material exhibits higher peroxide yields (12–15%). On the other hand, FeMnNC-T catalyst mainly follows a $4e^-$ ORR pathway, with peroxide yields below 10% (Figure 23c).

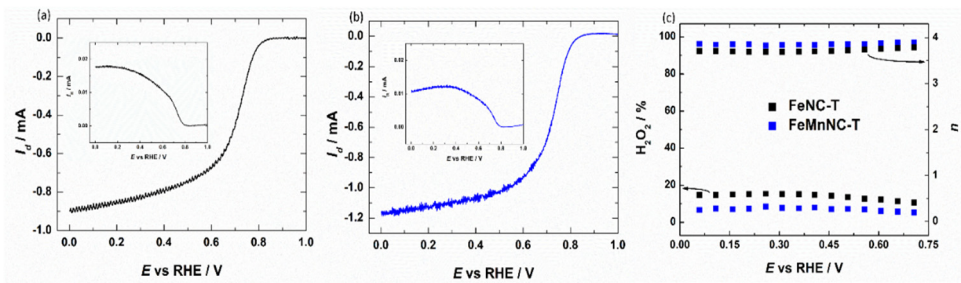

Figure 23. RRDE voltammetry curves for ORR in O_2-saturated 0.5 M H_2SO_4 solution at 960 rpm (insets show the respective ring currents) for (a) FeNC-T and (b) FeMnNC-T catalysts; (c) percentage yield of H_2O_2 formation and the *n* value as a function of potential.

M–N–C catalysts are generally more durable in alkaline media as compared to acidic media due to the lower propensity for 3d metal dissolution, but carbon corrosion is still a concern as it impacts the structure of the carbon framework [105]. The low electrochemical stability of the electrocatalysts is one of the major obstacles to long-term AEMFC operation. To evaluate the durability of FeCoNC and FeCoNC-MgOAc, the catalysts were subjected to accelerated stability tests by potential cycling (Figure 24). Both electrocatalysts demonstrated excellent stability; for FeCoNC a minor decay of 25 mV for both $E_{1/2}$ and E_{onset} was observed after 15000 potential cycles. For FeCoNC-MgOAc, the E_{onset} was shifted to a more negative value by 20 mV, but the $E_{1/2}$ value was only very slightly altered after 15000 potential cycles ($\Delta E_{1/2}$ = 10 mV). The slightly improved stability compared to FeCoNC could be caused by the higher degree of graphitization, as confirmed by both Raman spectroscopy and XRD analysis [IV].

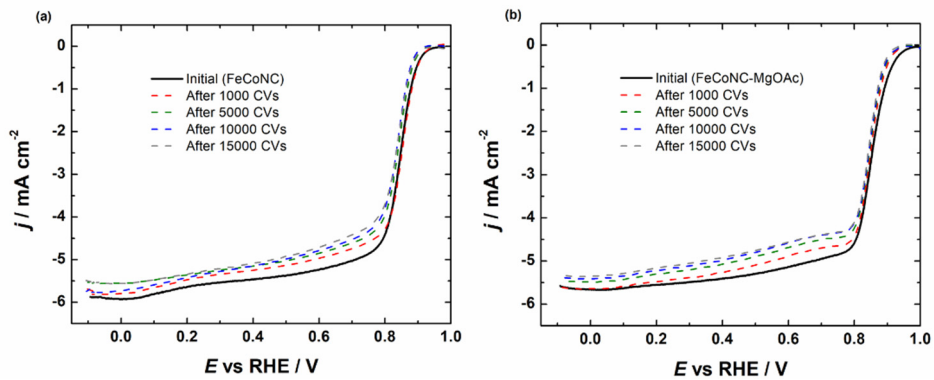

Figure 24. RDE voltammetry curves for O_2 reduction in O_2-saturated 0.1 M KOH before and after repetitive potential cycles for (a) FeCoNC and (b) FeCoNC-MgOAc, respectively

Despite the significantly higher loadings, the materials displayed a relatively lower durability in acidic media, where demetallation of the active sites in a much larger concern. As seen in Figure 25, there is a significant drop in the ORR activity during the first 1000 potential cycles, after which the rate of decrease slows down. After 10000 CVs, for the FeNC-T catalyst the $E_{1/2}$ value shifted negative by 76 mV, and for FeMnNC-T the $\Delta E_{1/2}$ was 66 mV. The initial rapid decrease can be attributed to the demetallation of M–N_x sites, followed by more gradual decrease related to carbon corrosion. Similar trends have been found in multiple studies, where the initial stage of rapid activity decline is followed by the second stage, where the catalyst experiences a gradual decrease in performance, persisting throughout its entire lifespan [173,178,179]. For the untemplated FeNC catalyst, the decrease in activity is quite rapid, eventually the $E_{1/2}$ value shifted by 95 mV in negative direction. Raman spectroscopy studies confirmed the smaller degree of graphitization for FeNC, which can lead to more significant carbon corrosion and is likely behind the larger decrease in the ORR perfor-

mance. The presence of imperfect graphitic carbon shells surrounding the metallic particles could offer an additional explanation for the loss of electrocatalytic activity, due to allowing the acidic electrolyte to reach the metal particles causing additional demetallation [173]. This might be most significant in the case of FeNC catalyst, where the carbon is more disordered, and the overall iron content is very high. It should be highlighted that degradation pathways are often interconnected, affecting both the active sites at the atomic level and the properties of the electrode layer at the macroscale and mesoscale. For example, oxidation of carbon results in the degradation of the carbon structure, followed by demetallation of active sites [82].

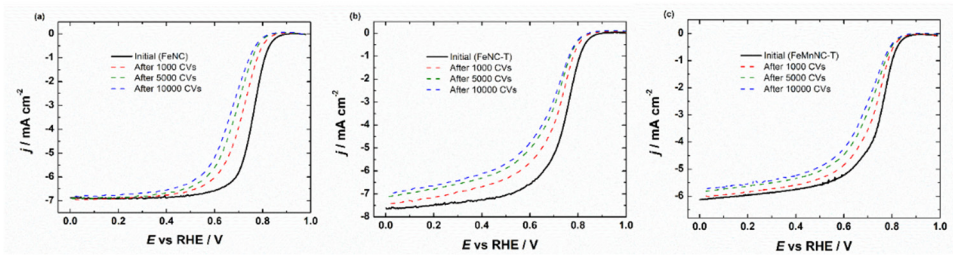

Figure 25. RDE voltammetry curves in 0.5 M H_2SO_4 for O_2 reduction before and after repetitive potential cycles for (a) FeNC; (b) FeNC-T, and (c) FeMnNC-T catalysts.

6.4.3 AEMFC results of catalysts

As mentioned in Sub-section 4.3.3, multiple studies have indicated that besides the intrinsic activity, optimal carbon structure and porosity is required for achieving effective mass and charge transfer, especially in fuel cells where mass-transport issues are largely due to the huge loading that PGM-free catalyst require [114,180]. Reactants, such as hydrogen and oxygen, are delivered to the cell in the vapor phase and transported through GDEs. Catalysts materials must have a large surface area to accommodate high density of active sites, optimal porous structure to facilitate mass transport, and chemical and physical stability under fuel cell working conditions [181,182].

The electrocatalysts were studied in MEAs under H_2-O_2 conditions to investigate both the high voltage current density and maximum power density, which are limited by mass transport in the catalyst layer and cannot be investigated by RDE due to the low concentration of dissolved O_2 in the aqueous electrolyte, which hinders the acquisition of information at high current density and low cell potential [183]. H_2/O_2 polarization curves of AEMFCs based on the FeCoNC and FeCoNC-MgOAc bimetallic ORR electrocatalysts compared to 20 and 40 wt.% Pt/C are shown in Figure 26. The data was acquired at a cell temperature of 55 °C with optimized dewpoint temperatures. The FeCoNC-MgOAc and 20 wt.% Pt/C AEMFCs showed $j_{0.8\ V}$ values of 0.20 and 0.35 A cm^{-2}, while the 40 wt.% Pt/C value was 0.23 A cm^{-2}. All these materials had virtually the same average

area specific resistance (ASR) values of ~0.08 Ω cm^{-2} (see Figure 26b). Interestingly, the untemplated catalysts FeCoNC showed much lower performance ($j_{0.8\,V}$ of 0.08 A cm^{-2}) and higher ASR of ~0.17 Ω cm^{-2}. Based on the available data, it is difficult to determine whether this difference is due to the lower intrinsic activity of the catalyst, or the lower mesoporosity leading to decreased number of TPB sites in the catalyst layer. Since the difference in activity in RDE measurements between FeCoNC and FeCoNC-MgOAc was relatively small, it is likely a combination of both factors. As such, the increased performance can likely be attributed to more accessible active sites within the catalyst layer due to the suitable nanostructure of the catalyst prepared with Mg-based template. Especially at higher current densities, FeCoNC-MgOAc outperformed the cells made with 20 wt.% and 40 wt.% Pt/C in terms of peak power density, by arriving at a value of 0.92 W cm^{-2} compared to 0.85 and 0.69 W cm^{-2}, respectively (see Figure 26a). FeCoNC-MgOAc catalyst also demonstrated a high stability, exhibiting a peak-to-peak voltage degradation of 0.0017 V h^{-1} with no appreciable increase in ASR (Figure 26c).

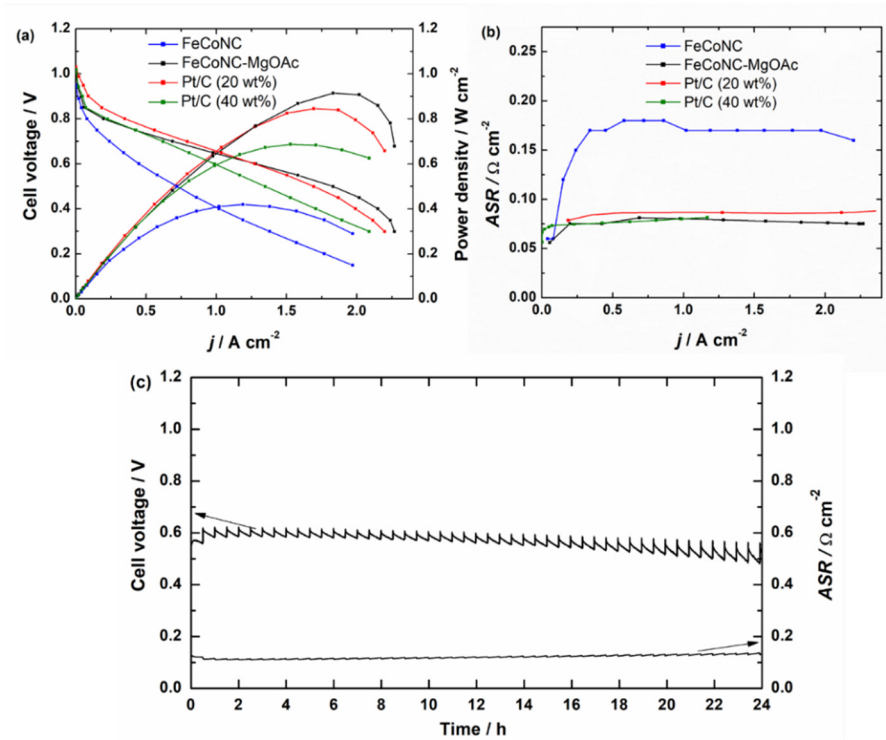

Figure 26. H_2-O_2 AEMFC results with FeCoNC and FeCoNC-MgOAc bimetallic ORR catalysts loaded to 0.96 mg cm^{-2} compared to 20 wt.% and 40 wt.% Pt/C cathode catalyst loaded to 0.97 and 0.56 mg_{Pt} cm^{-2}, respectively. (a) cell voltage and power density versus current density, and corresponding (b) area specific resistance values versus current density. (c) 24 h durability test of AEMFC constructed with FeCoNC-MgOAc bimetallic ORR catalyst, under a constant current density load of 600 mA cm^{-2}.

In comparison to other recently published transition metal (Co and/or Fe) based cathode electrocatalyst reports operated with H_2/O_2, FeCoNC-MgOAc performed quite well (Table 1). The highest report in the literature employed a Fe-N-C catalyst arrived at a P_{max} of 2.05 W cm^{-2}, albeit at a comparatively higher cell temperature of 80 °C [31]. It is well known that higher cell temperatures enhance fuel cell performance [184,185]. At a closer temperature of 60 °C, another report by our group employing a bifunctional CoFe-N-CDC/CNT cathode arrived at a P_{max} of 1.12 W cm^{-2} [37], which is slightly higher than the P_{max} of our MEA based on FeCoNC-MgOAc. It is important to keep in mind that these results are not directly comparable due to the use of very different membrane and ionomer chemistries. The lack of a widely available standard makes the comparison of cathode catalysts in AEMFC much more difficult.

6.4.4 PEMFC results of catalysts

Similar behavior of the catalysts was observed in results obtained with H_2/O_2 PEMFC. Both of the templated catalysts (FeNC-T and FeMnNC-T) showed good fuel cell performance with peak power densities of 514 and 334 mW cm^{-2}, respectively (Figure 27). The MEA prepared with FeNC cathode demonstrated a discernibly lower performance, especially at lower voltages, achieving only a moderate P_{max} value of 188 mW cm^{-2}. The better performance of the catalysts prepared with the Mg-based template at higher current densities can be explained by the improved transport of reactants and products to and from the active sites due to the increased mesoporosity in these catalysts, which could expose additional active sites at three-phase boundaries in the catalyst layer. Multiple studies have indicated that the optimal carbon structure is essential for PGM-free catalyst materials because of the thick catalyst layers due to the high catalyst loading needed. A loading of 4 mg cm^{-2} results in a thickness of about 100 µm [63,141], compared to Pt/C cathodes that are approximately an order of magnitude thinner [186]. Due to the much thinner catalyst layer and higher electrocatalytic activity, the commercial Pt-based cathode is able to achieve much higher current densities (Figure 27). Therefore, even though a hierarchical porous structure that facilitates efficient O_2 transport and even ionomer coverage is helpful in increasing the performance for PGM-free catalyst materials, further improvements in the catalyst design are needed to match the performance of PGM-based cathodes in PEMFC. It is however less clear why the bimetallic FeMnNC-T catalyst shows lower PEMFC performance as compared to FeNC-T catalyst. It cannot be explained by the difference in the carbon material structure, as the STEM and N_2 physisorption measurements show that this is very similar for these two catalysts. A plausible explanation could be that due to slightly different surface composition of the bimetallic catalyst, evidenced by the XPS analysis and EDS mapping, and the higher degree of graphitization, the ionomer interaction with carbon support is different and this alters the ionomer distribution. If the ionomer interacts more intimately with the catalyst surface, a more homogeneous ionomer

distribution across the catalyst layer will be achieved [187]. To ensure good PEMFC results, the cathode ink and MEA preparation was optimized using FeNC-T catalyst and the same formulation was used with the other catalysts in order to lower the number of variables. However, due to the different properties of FeMnNC-T, it may require a slightly different ink formulation for the optimal performance. In order to confirm this theory, a detailed investigation of the ionomer distribution and porosity within the catalyst layer would be needed.

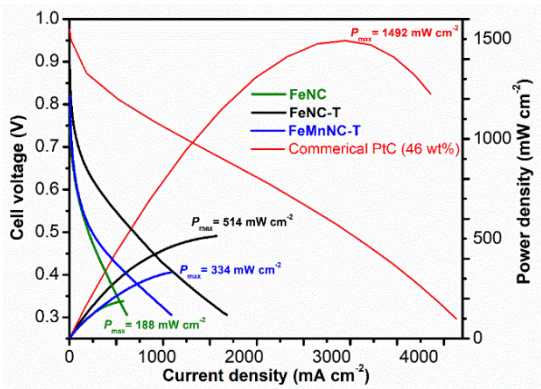

Figure 27. Polarization and power density curves for the PGM-free electrocatalyst based cathodes and as a comparison a commercial Pt/C cathode, with H_2-O_2 PEMFC and 100% relative humidity at 80 °C, 2 bar backpressure, and 0.3 NLPM flow rate of gases on both the anode and cathode side. Cathode loading of 4 mg cm^{-2} (for PGM-free catalysts) or 0.25 mg_{Pt} cm^{-2} (for Pt-based catalyst).

6.5 Catalysts prepared via ionothermal synthesis

In the fifth part of the work, a novel ionothermal synthesis approach coupled with trans-metalation was used to prepare atomically dispersed electrocatalysts. To address the challenges associated with traditional high-temperature synthesis, we used an emerging synthetic approach that decouples the formation of carbon matrix from the active site creation [101]. The active site imprinting strategy leverages specific imprinting metals (such as Zn or Mg) that promote the formation of the desired nitrogen coordination sites. The approach involves initially preparing a Mg–NC or Zn–NC material, followed by a subsequent low-temperature coordination step, during which the Mg ion in the coordinated site is replaced (trans-metalated) by an electrocatalytically active element, such as iron. We utilized Honeyol and $Mg(NO_3)_2$ to prepare the catalysts with a hierarchical porous structure, high surface area and imprinted Mg–N_x sites. The Mg was then replaced with iron via ion-exchange method, to create atomically dispersed Fe–N_x sites. The catalysts were thoroughly characterized and the ORR electrocatalytic activity of the prepared catalysts was evaluated via RDE method to gain insight into the structure-activity relationships.

6.5.1 Physical characterization of catalysts prepared via ionothermal synthesis

In the ionothermal synthesis Honeyol is partially or completely dissolved within the salt melt. $Mg(NO_3)_2 \cdot 6H_2O$ was chosen as the precursor since it has a low melting point (88.9 °C), which is below the onset of carbonization of organic species and can thus acts as ionothermal liquid reaction medium. While a variety of magnesium salts can be used, we specifically selected the nitrate for the secondary purpose of introducing nitrogen moieties into the carbonizing phase. During pyrolysis, the generation of pores occurs through two main effects. Firstly, the mostly macroporous structure is created by the liquid salt droplets inside the carbonizing phase [121]. The SEM images of the materials display a hierarchically porous structure (Figure 28), where both macropores and larger mesopores can be seen. The secondary porosity is created when the carbonizing phase encircles the in-situ formed MgO nanoparticles (so-called hard template) [118,166]. The SEM image of MgO@NC-LT displays numerous MgO nanoparticles that are evenly embedded in the carbon structure (Figure 28a).

The HAADF-STEM image of MgO@NC-LT and elemental mapping by EDS (Figure 29a-c) reveal an even distribution of Mg across the carbon structure with no large MgO agglomerates. STEM-BF images reveal the presence of small spherical nanoparticles embedded in the carbon matrix. Once these nanoparticles are removed via acid-washing, additional mesopores are created within the carbon material, as can be seen from Figures 28b and 29f. These pores seem to range in size from approximately 3 to 20 nm, corresponding to the size of the MgO nanoparticles, with the larger mesopores formed from aggregated clusters (Figure 29d). The STEM images (Figure 29e, f) provide a more detailed look into the carbon structure after removal of MgO nanoparticles. The hierarchically porous morphology of NC-LT is promising for exposing a large number of active sites and enhancing the mass transport of reactants in the catalyst layer [90,153].

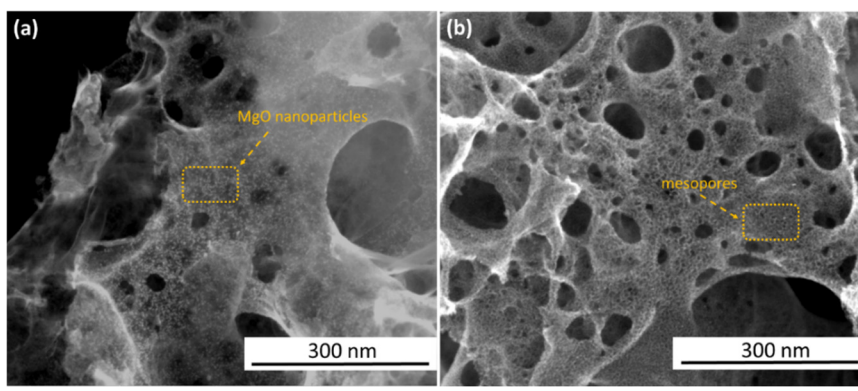

Figure 28. SEM images of (a) MgO@NC-LT, showing the MgO nanoparticles and (b) NC-LT materials, showing the mesopores created after the acid-treatment.

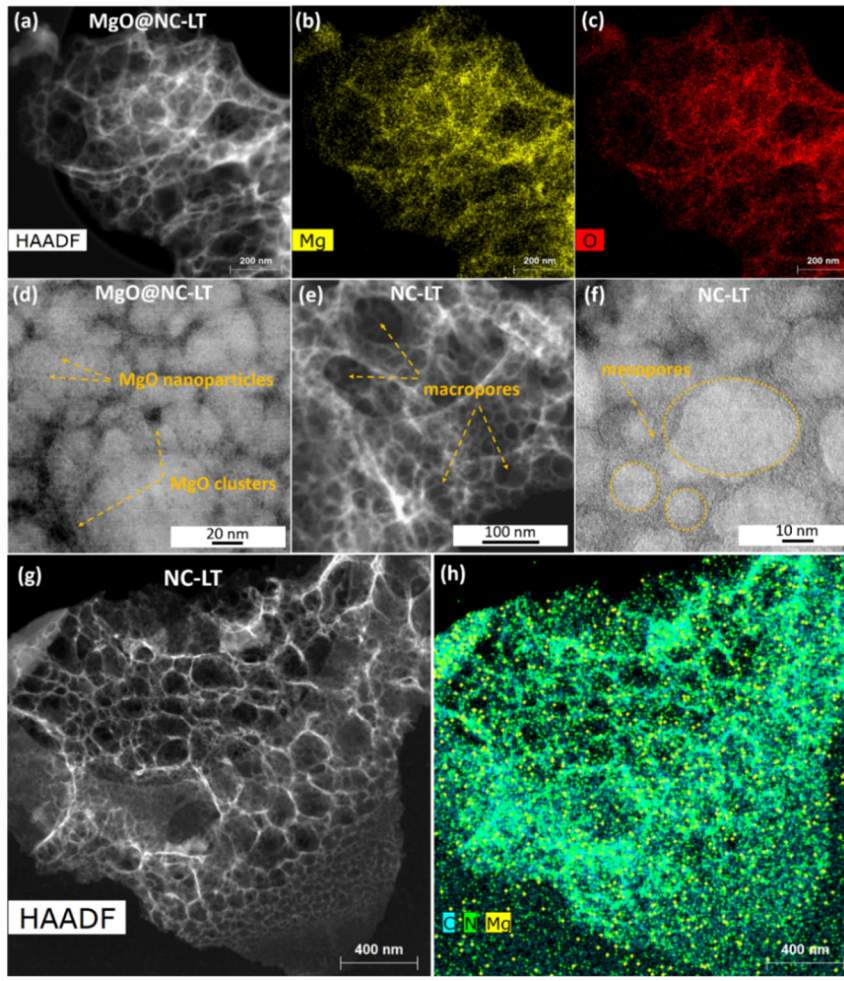

Figure 29. (a) HAADF-STEM image of MgO@NC-LT and (b, c) the overlays of EDS maps of the Mg and O elements. (d and f) BF-STEM images, (e and g) HAADF-STEM images of NC-LT and (h) EDS maps of the C, N and Mg elements.

The nitrogen adsorption isotherm of the catalyst and the PSD graph are shown in Figure 30a. The isotherm displays a steep rise at low pressure, indicating some microporosity in the carbon material, which is caused by the rapidly evolved gases during the decomposition of nitrate. A slope can be seen forming at higher relative pressures, indicating the filling of mesopores. The presence of macro-porosity can be assumed from the PSD graph, however due to the upper limit of detection for this method (50 nm for N_2 physisorption) more precise information about the PSD at larger pore sizes cannot be obtained [72]. However, the presence of macropores and large mesopores that are introduced into the carbonizing precursors by molten salt droplets was confirmed by both SEM and STEM measurements.

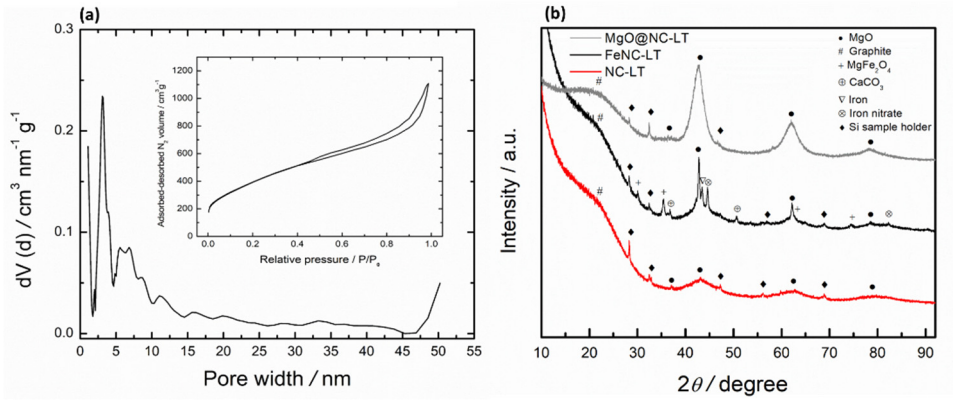

Figure 30. (a) Pore size distribution of FeNC-LT catalysts with the isotherm shown in inset and (b) XRD patterns for various materials.

HAADF-STEM and the EDS mapping overlay (Figure 29g and h) evidence the successful removal of most of the MgO nanoparticles and the formation of mesopores. Although, some MgO is apparently left in the material even after acid treatment, as evidenced by the XRD pattern for NC-LT (Figure 30b), where a MgO phase (PDF-00-045-0946) with an average crystallite size of around 4 nm was detected. This same phase is also observed in the non-acid washed material MgO@NC-LT in much greater quantities. Nitrogen is evenly distributed over the entire carbon structure, indicating successful introduction of the dopant element. Around 2 wt.% of Mg can be detected in the NC-LT material after the acid washing. XPS analysis of the material was conducted to obtain more detailed information about the moieties present on the surface. XPS survey spectra displays peaks at 285, 400, and 532 eV, corresponding to binding energies of C 1s, N 1s, and O 1s (Figure 31). Around 3 at.% of nitrogen is detected on the surface of the NC-LT material. A closer look at the detailed N 1s XPS spectra reveals that hydrogenated or pyrrolic nitrogen is the most common N moiety. This supports the findings from Menga et al. [101] that mainly tetrapyrrolic M–N_x sites are formed during the pyrolysis process in the presence of Zn or Mg salts, as minimal carbothermal reduction will occur. This is supported by the C 1s spectra of NC-LT and FeNC-LT [VI], where most of the carbon is sp^3 with some sp^2 (characteristic of highly defective and disordered carbon material) or present in various oxygen-containing moieties, while the carbide peak is very faintly detected. For the FeNC-LT material, obtained after the trans-metalation procedure and subsequent pyrolysis, the pyrrolic-N remains the most common moiety. As the pyrrolic- N peak remains unaltered following the heat-treatment, the pyrrolic Fe–N bonds seem to be robust against temperatures up to 800 °C, without undergoing decomposition. However, comparison of N 1s spectra of NC-LT and FeNC-LT (Figure 31, insets) reveals that additional pyridinic nitrogen sites are created in the latter. Formation of pyridinic sites require graphitization

of the carbon structure (occurring at above 1300 °C), but it is well known that iron can act as a catalyst for graphitization at lower temperatures. Some smaller iron-containing nanoparticles (most likely in chloride or hydroxide form) are likely present after the trans-metalation even after acid-treatment, and thus catalyze the formation of pyridinic nitrogen sites during the second heat-treatment. The iron-containing nanoparticles can decompose and release Fe atoms, which can then coordinate with nitrogen, leading to increased density of Fe–N_x sites [84]. This was also observed in the work of Menga et al., who observed 90% reduction of oxidized iron by Mössbauer spectroscopy after the second pyrolysis [101]. From the HAADF-STEM image and corresponding EDS maps for FeNC-LT (Figure 32), we observe no change in the morphology of the material after trans-metalation and an even distribution of Fe and Mg, while no large agglomerated metallic iron or carbide nanoparticles can be observed, indicating that Fe is mainly atomically dispersed and likely coordinated to nitrogen. Higher magnification HAADF and BF images (Figure 32d and e) display the M–N_x sites present in the material, while small clusters of presumably iron or magnesium can be observed in some areas. The nature and elemental composition of these clusters as well as whether they are bound to neighboring C/N atoms or not, remains unknown.

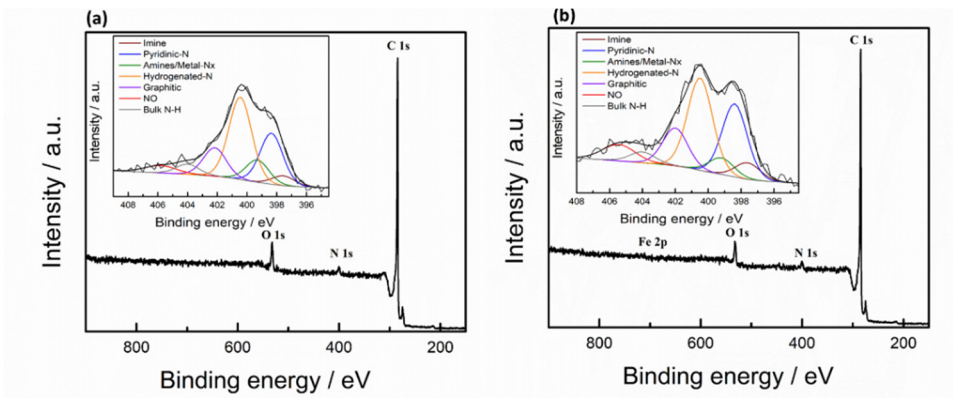

Figure 31. XPS survey spectra for (a) NC-LT and (b) FeNC-LT, with the insets showing detailed XPS N 1s spectra.

From the XRD pattern of FeNC-LT (Figure 30b) we can observe some crystalline iron phases such as metallic iron (PDF-04-002-3692) and iron nitrate (PDF-04-021-9691). In addition to the MgO phase (PDF-00-045-0946) also present in NC-LT, a more agglomerated phase (PDF-04-008-3504), with an average crystallite size of 38 nm was also observed, likely forming during the second pyrolysis. In addition, some $MgFe_2O_4$ (PDF-04-012-0947) XRD peaks were also observed. The carbon material is highly disordered, consistent with the XPS C 1s spectra. Peaks indexed to $CaCO_3$ phase (PDF-01-088-8687) can also be detected in the FeNC-LT material, most likely due to the contamination from the pyrolysis tube or boat. Since Mg can still be detected in the FeNC-LT material, it would suggest that the trans-metalation procedure was not able to convert all of the Mg–N_x sites.

If the site is located deep in the micropores of the carbon matrix, it is unlikely that the Fe ions can reach the sites during the ion-exchange process. We presume that further research is needed to find the right conditions for the ion-exchange step to ensure the highest possible conversion of Mg–N_x sites. The presence of 2.1 wt.% of iron in FeNC-LT is verified through MP-AES analysis, while no Fe can be detected in NC-LT material. Around 2 wt.% of Mg can be detected in both NC-LT and FeNC-LT, however the exact determination of the efficiency of Mg-to-Fe conversion is problematic, since some of the Mg is in the form of MgO and $MgFe_2O_4$ nanoparticles according to XRD analysis. The interpretation is further convoluted if the sample inhomogeneity is considered.

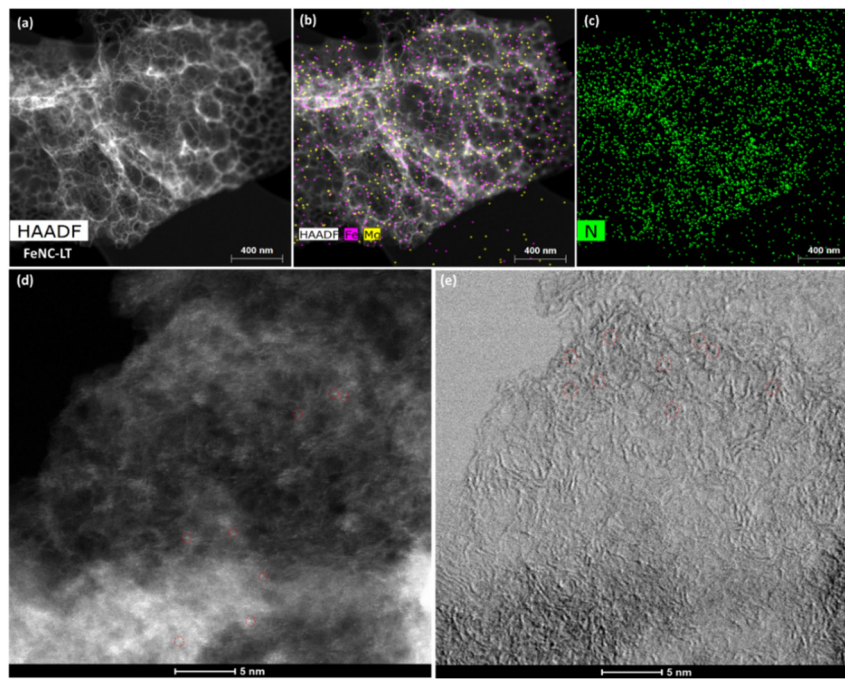

Figure 32. (a) HAADF-STEM image of FeNC-LT and (b, c) overlays of EDS maps of the Fe, Mg, and N elements. (d, e) HAADF-STEM and BF images of FeNC-LT with some of the atomically dispersed sites circled in red.

6.5.2 Electrochemical characterization of catalysts prepared via ionothermal synthesis

The electrocatalytic performance of the catalysts was initially assessed through RDE testing in O_2-saturated 0.1 M KOH (Figure 33a). The NC-LT catalyst exhibited low ORR activity characterized by a large overpotential. This catalyst was prepared without the ion-exchange step, since it does not contain any Fe–N_x sites, the electrocatalytic activity is derived from the nitrogen moieties in the carbon matrix. These sites are generally considered to be ORR-active, however, they

catalyze the ORR mainly via the 2-electron pathway [106,188,189]. Following low-temperature ion exchange from Mg–N_x to Fe–N_x and the acid treatment, the ORR electrocatalytic activity of the catalyst material is significantly increased, exhibiting an $E_{1/2}$ of 0.77 V. Subsequent high-temperature treatment further enhances the catalyst's activity, attributed to the increased density of active sites that are formed during the pyrolysis when agglomerated iron particles decompose and coordinate with either pyridinic nitrogen or left-over Mg–N_x sites. The FeNC-LT catalyst reaches an impressive $E_{1/2}$ value of 0.87 V, comparable to the benchmark Pt/C catalyst.

As mentioned previously, since not all of the Mg in the material was exchanged to Fe, a catalyst was prepared using the Fe^{3+} ions during the ion-exchange (FeNC-LT-$FeCl_3$). However, no noticeable change in the overpotential for ORR was observed. Apparently, the formation of Fe–N_x sites in the catalyst are not dependent on the specific Fe ion source used during trans-metalation.

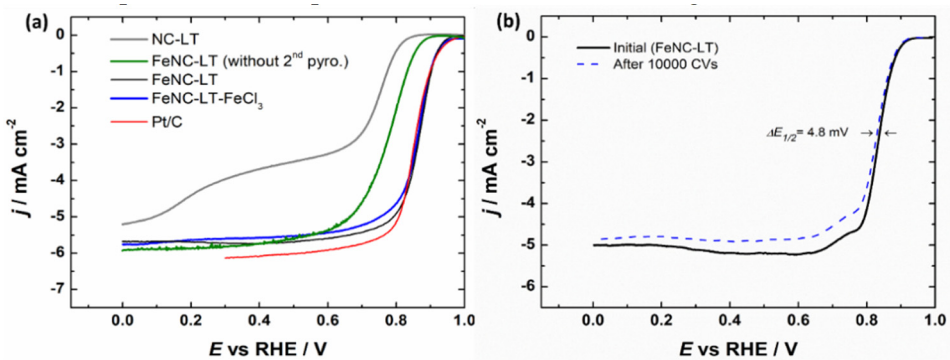

Figure 33. (a) A comparison of RDE voltammetry curves for ORR on various PGM-free catalysts and commercial Pt/C in O_2-saturated 0.1 M KOH solution at 1900 rpm, (b) RDE voltammetry curves for O_2 reduction before and after repetitive potential cycles for FeNC-LT. ν = 10 mV s^{-1}.

In order to investigate the kinetics of the ORR in more detail, the polarization curves were measured using different rotation rates from 360 to 3100 rpm (Figure 34a). We observed well-defined limiting current plateaus, with a consistent onset potential and varying limiting current density. The K–L plots (Figure 34b) exhibit a good linearity indicating the first-order reaction kinetics. The *n* value, calculated from the K–L slopes, reveals that the FeNC-LT catalysts follow predominantly a 4-electron pathway (Figure 32d). The accelerated stability testing of FeNC-LT was conducted by continuous potential cycling in O_2-saturated 0.1 M KOH between 1.0 and 0.6 V vs RHE with a scan rate of 200 mV s^{-1} (Figure 33b). The ORR electrocatalytic activity only slightly decreased after 10000 cycles ($\Delta E_{1/2}$ = 4.8 mV), even with a relatively low loading of 0.2 mg cm^{-2}, indicating excellent stability in the RDE tests.

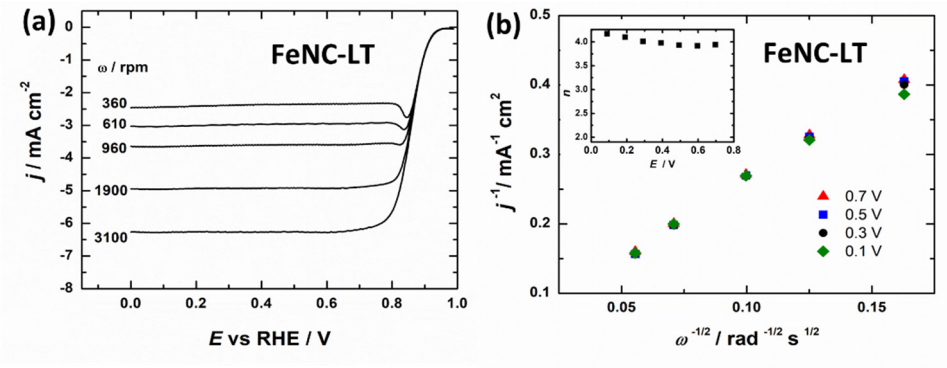

Figure 34. (a) RDE voltammetry curves for oxygen reduction in O_2-saturated 0.1 M KOH solution at different rotation rates for FeNC-LT; (b) K-L plots derived from the RDE data with inset showing the number of electrons transferred per O_2 molecule.

The FeNC-LT catalyst was further tested in single-cell AEMFC measurements, where the catalysts displayed moderate activity as the cathode material with a P_{max} value of 204 mW cm^{-2} (Figure 35a). Compared to the thin catalyst layers of PGM-based catalysts, the CCLs prepared with the FeNC-LT cathode are significantly thicker resulting from the low packing factor (~100 µm mg^{-1} cm^{-2}), consequently the ASR for this catalyst is quite high (see Figure 35b). Applying a backpressure of 100 kPa somewhat alleviated this factor by lowering the ASR, and a P_{max} value of 256 mW cm^{-2} was obtained. Thus, optimizing the synthesis conditions of the carbon-based catalysts and the catalyst layer design is likely necessary to obtain higher performance in AEMFC.

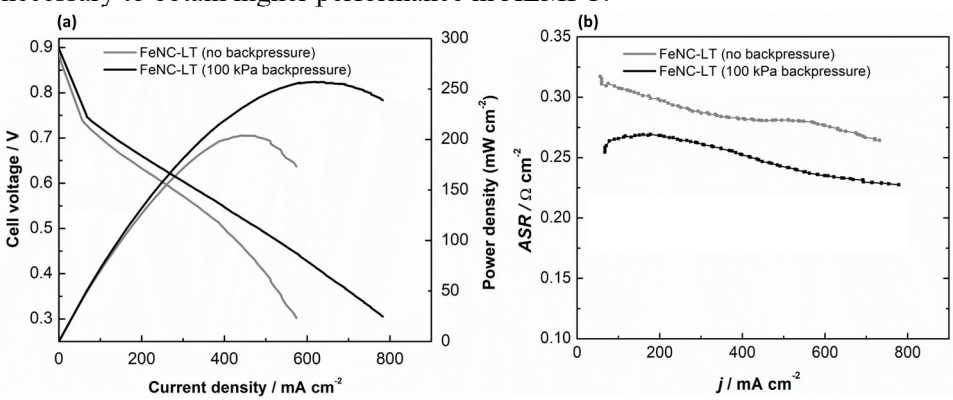

Figure 35. H_2-O_2 AEMFC performance of FeNC-LT cathode catalyst loaded to 0.89 mg cm^{-2} without backpressure and an applied backpressure of 100 kPa on both anode and cathode compartments. (a) Polarization and power density curves and (b) corresponding ASR values versus current density.

7. SUMMARY

The aim of this PhD thesis was to develop PGM-free resorcinol-derived electrocatalysts for the oxygen reduction reaction (ORR) to replace scarce and expensive PGM-based catalysts, for use in polymer electrolyte fuel cells. The prepared catalysts were physicochemically characterized to provide detailed insights into the active sites and microstructure of the catalysts. Their performance was evaluated in half-cell tests and as cathode catalysts in polymer electrolyte fuel cells. During the work, the dependence of the electrocatalytic performance of the catalyst materials on their structure and composition was evaluated and the potential of these PGM-free electrocatalysts in fuel cell applications was demonstrated.

In the first part of the work, Fe- and Co-containing nitrogen-doped carbon materials were prepared from 5-methylresorcinol-formaldehyde (5MR-FA) resins using two different methods [I]. Firstly, carbon nanospheres (CNSs) were obtained by pyrolysis of 5MR-FA nanospheres. Then, the CNSs were doped by pyrolyzing them in the presence of nitrogen and transition metal precursors. The other set of materials was prepared by in-situ doping, where the 5MR-FA nanospheres were combined with the precursors and pyrolyzed. A comparison between the doped CNSs and in-situ doped materials revealed that the latter catalysts exhibited superior ORR activity, although they did not maintain their spherical structure. This higher activity was attributed to a greater surface area and mesoporous structure, enabling the exposure of a higher number of active sites.

In the second and third part of the research, the polymerization reaction was omitted, and 5MR was directly used as the carbon precursor along with DCDA and Fe, Co, and/or Ni salts [II, III]. The precursor ratios and metal content were optimized to achieve the highest electrocatalytic activity toward ORR, as well as test their performance of in oxygen evolution reaction. The resulting bimetallic FeCoNC-OP-at catalyst demonstrated activity comparable to a commercial Pt/C catalyst in half-cell tests and achieved a current density of 170 mA cm^{-2} at 0.8 V and a maximum power density of 415 mW cm^{-2} in AEMFC tests, when used as the cathode catalyst.

In further experiments, a mixture of alkylresorcinols (Honeyol^{TM}) was utilized as a carbon precursor. The fourth part of the research explored the effect of tuning catalyst nanostructure using a sacrificial magnesium-based template [IV and V]. The catalysts were doped with iron or with combinations of Fe-Co or Fe-Mn. Catalysts prepared with the template demonstrated over twice higher maximum power densities in both AEM and PEM fuel cells compared to non-templated catalysts, achieving impressive maximum power densities of 920 mW cm^{-2} in AEMFC and 514 mW cm^{-2} in PEMFC. This improvement was attributed to two main factors: the increased surface area, which exposes more active sites, and the hierarchically porous structure, which facilitates more efficient reactant transport through the catalyst layer.

The fifth part of the thesis demonstrates the potential of the ionothermal synthesis and active-site imprinting approach for preparing electrocatalysts with high density of $M–N_x$ sites [VI]. $Mg(NO_3)_2$ was used to imprint $Mg–N_x$ sites that subsequently underwent trans-metalation with Fe, to obtain $Fe–N_x$ active sites. The Mg nitrate simultaneously produces a hierarchically porous carbon structure through the in-situ formation of MgO nanoparticles that serve as the sacrificial template. The precursor ratios were optimized and the resulting electrocatalyst exhibited excellent electrocatalytic activity for ORR in alkaline conditions ($E_{1/2}$ = 0.87 V), comparable to that of commercial Pt/C catalyst.

This research contributes valuable insights into the development of efficient PGM-free electrocatalysts for oxygen reduction reaction for fuel cell applications, using cheap and abundant precursors. This work emphasizes the importance of tailoring the catalyst structure and composition to obtain the highest possible fuel cell performance. These findings pave the way for sustainable energy solutions by reducing reliance on precious metals.

8. REFERENCES

[1] W. Agnieszka, EU energy infrastructure: Boosting energy security, (accessed April 1, 2024).

[2] I. Staffell, D. Scamman, A.V. Abad, P. Balcombe, P.E. Dodds, P. Ekins, N. Shah, K.R. Ward, The role of hydrogen and fuel cells in the global energy system, Energy Environ. Sci. 12 (2019) 463–491. https://doi.org/10.1039/C8EE01157E.

[3] H. Nazir, N. Muthuswamy, C. Louis, S. Jose, J. Prakash, M.E. Buan, C. Flox, S. Chavan, X. Shi, P. Kauranen, T. Kallio, G. Maia, K. Tammeveski, N. Lymperopoulos, E. Carcadea, E. Veziroglu, A. Iranzo, A.M. Kannan, Is the H2 economy realizable in the foreseeable future? Part II: H2 storage, transportation, and distribution, Int. J. Hydrogen Energy 45 (2020) 20693–20708. https://doi.org/10.1016/j.ijhydene.2020.05.241.

[4] N. Gray, R. O'Shea, D. Wall, B. Smyth, P.N.L. Lens, J.D. Murphy, Batteries, fuel cells, or engines? A probabilistic economic and environmental assessment of electricity and electrofuels for heavy goods vehicles, Adv. Appl. Energy 8 (2022) 100110. https://doi.org/10.1016/j.adapen.2022.100110.

[5] X. Liu, K. Reddi, A. Elgowainy, H. Lohse-Busch, M. Wang, N. Rustagi, Comparison of well-to-wheels energy use and emissions of a hydrogen fuel cell electric vehicle relative to a conventional gasoline-powered internal combustion engine vehicle, Int. J. Hydrogen Energy 45 (2020) 972–983. https://doi.org/10.1016/j.ijhydene.2019.10.192.

[6] D.-Y. Lee, A. Elgowainy, A. Kotz, R. Vijayagopal, J. Marcinkoski, Life-cycle implications of hydrogen fuel cell electric vehicle technology for medium- and heavy-duty trucks, J. Power Sources 393 (2018) 217–229. https://doi.org/10.1016/j.jpowsour.2018.05.012.

[7] Clean Hydrogen Joint Undertaking., The road to net zero: study on the strategic deployment of battery electric vehicles and fuel cell electric vehicles infrastructure., Publications Office, LU, 2022. https://data.europa.eu/doi/10.2843/49044 (accessed April 1, 2024).

[8] T. Yoshizumi, H. Kubo, M. Okumura, T. Yoshizumi, H. Kubo, M. Okumura, Development of High-Performance FC Stack for the New MIRAI, in: SAE International, 2021. https://doi.org/10.4271/2021-01-0740.

[9] K. Jiao, J. Xuan, Q. Du, Z. Bao, B. Xie, B. Wang, Y. Zhao, L. Fan, H. Wang, Z. Hou, S. Huo, N.P. Brandon, Y. Yin, M.D. Guiver, Designing the next generation of proton-exchange membrane fuel cells, Nature 595 (2021) 361–369. https://doi.org/10.1038/s41586-021-03482-7.

[10] B.G. Pollet, S.S. Kocha, I. Staffell, Current status of automotive fuel cells for sustainable transport, Curr. Opin. Electrochem. 16 (2019) 90–95. https://doi.org/10.1016/j.coelec.2019.04.021.

[11] Fuel cell electric vehicles and platinum demand – CME Group, (n.d.). https://www.cmegroup.com/articles/2022/wpic-fuel-cell-electric-vehicles-and-platinum-demand.html (accessed April 1, 2024).

[12] D. Banham, J.-Y. Choi, T. Kishimoto, S. Ye, Integrating PGM-Free Catalysts into Catalyst Layers and Proton Exchange Membrane Fuel Cell Devices, Adv. Mater. 31 (2019) 1804846. https://doi.org/10.1002/adma.201804846.

[13] A. Javed, P. Palafox Gonzalez, V. Thangadurai, A Critical Review of Electrolytes for Advanced Low- and High-Temperature Polymer Electrolyte Membrane Fuel

Cells, ACS Appl. Mater. Interfaces 15 (2023) 29674–29699. https://doi.org/10.1021/acsami.3c02635.
[14] F. Barbir, CHAPTER 10 – Fuel Cell Applications, in: F. Barbir (Ed.), PEM Fuel Cells, Academic Press, Burlington, 2005: pp. 337–397. https://doi.org/10.1016/B978-012078142-3/50011-2.
[15] N.A. Anastasijević, V. Vesović, R.R. Adžić, Determination of the kinetic parameters of the oxygen reduction reaction using the rotating ring-disk electrode: Part I. Theory, J. Electroanal. Chem. Interfacial Electrochem. 229 (1987) 305–316. https://doi.org/10.1016/0022-0728(87)85148-3.
[16] R. Adzic, In: J. Lipowski, P. N. Ross, (Eds.) Electrocatalysis, Wiley, New York (1998) 197-242.
[17] W.E. Mustain, M. Chatenet, M. Page, Y.S. Kim, Durability challenges of anion exchange membrane fuel cells, Energy Environ. Sci. 13 (2020) 2805–2838. https://doi.org/10.1039/D0EE01133A.
[18] J. Hyun, H.-T. Kim, Powering the hydrogen future: current status and challenges of anion exchange membrane fuel cells, Energy Environ. Sci. 16 (2023) 5633–5662. https://doi.org/10.1039/D3EE01768K.
[19] G. Tsotridis, A. Pilenga, M.G. De, T. Malkow, EU harmonised test protocols for pemfc mea testing in single cell configuration for automotive applications, JRC Publications Repository (2016). https://doi.org/10.2790/342959.
[20] F. Barbir, CHAPTER 3 – Fuel Cell Electrochemistry, in: F. Barbir (Ed.), PEM Fuel Cells, Academic Press, Burlington, 2005: pp. 33–72. https://doi.org/10.1016/B978-012078142-3/50004-5.
[21] H.A. Gasteiger, J.E. Panels, S.G. Yan, Dependence of PEM fuel cell performance on catalyst loading, J. Power Sources 127 (2004) 162–171. https://doi.org/10.1016/j.jpowsour.2003.09.013.
[22] D. Banham, J. Zou, S. Mukerjee, Z. Liu, D. Yang, Y. Zhang, Y. Peng, A. Dong, Ultralow platinum loading proton exchange membrane fuel cells: Performance losses and solutions, J. Power Sources 490 (2021) 229515. https://doi.org/10.1016/j.jpowsour.2021.229515.
[23] T. Stein, Y. Ein-Eli, Challenges and Perspectives of Metal-Based Proton Exchange Membrane's Bipolar Plates: Exploring Durability and Longevity, Energy Techno. 8 (2020) 2000007. https://doi.org/10.1002/ente.202000007.
[24] S.J. Peighambardoust, S. Rowshanzamir, M. Amjadi, Review of the proton exchange membranes for fuel cell applications, Int. J. Hydrogen Energy 35 (2010) 9349–9384. https://doi.org/10.1016/j.ijhydene.2010.05.017.
[25] M.M. Hossen, M.S. Hasan, M.R.I. Sardar, J. bin Haider, Mottakin, K. Tammeveski, P. Atanassov, State-of-the-art and developmental trends in platinum group metal-free cathode catalyst for anion exchange membrane fuel cell (AEMFC), Appl. Catal. B 325 (2023) 121733. https://doi.org/10.1016/j.apcatb. 2022.121733.
[26] A. Mehmood, M. Gong, F. Jaouen, A. Roy, A. Zitolo, A. Khan, M.-T. Sougrati, M. Primbs, A.M. Bonastre, D. Fongalland, G. Drazic, P. Strasser, A. Kucernak, High loading of single atomic iron sites in Fe–NC oxygen reduction catalysts for proton exchange membrane fuel cells, Nat. Catal. 5 (2022) 311–323. https://doi.org/10.1038/s41929-022-00772-9.
[27] X. Wan, X. Liu, Y. Li, R. Yu, L. Zheng, W. Yan, H. Wang, M. Xu, J. Shui, Fe–N–C electrocatalyst with dense active sites and efficient mass transport for high-performance proton exchange membrane fuel cells, Nat. Catal. 2 (2019) 259–268. https://doi.org/10.1038/s41929-019-0237-3.

[28] L. Osmieri, J. Park, D.A. Cullen, P. Zelenay, D.J. Myers, K.C. Neyerlin, Status and challenges for the application of platinum group metal-free catalysts in proton-exchange membrane fuel cells, Curr. Opin. Electrochem. 25 (2021) 100627. https://doi.org/10.1016/j.coelec.2020.08.009.
[29] X. Li, G. Liu, B.N. Popov, Activity and stability of non-precious metal catalysts for oxygen reduction in acid and alkaline electrolytes, J. Power Sources 195 (2010) 6373–6378. https://doi.org/10.1016/j.jpowsour.2010.04.019.
[30] P.G. Santori, F.D. Speck, J. Li, A. Zitolo, Q. Jia, S. Mukerjee, S. Cherevko, F. Jaouen, Effect of Pyrolysis Atmosphere and Electrolyte pH on the Oxygen Reduction Activity, Stability and Spectroscopic Signature of FeNx Moieties in Fe-N-C Catalysts, J. Electrochem. Soc. 166 (2019) F3311. https://doi.org/10.1149/2.0371907jes.
[31] H. Adabi, A. Shakouri, N. Ul Hassan, J.R. Varcoe, B. Zulevi, A. Serov, J.R. Regalbuto, W.E. Mustain, High-performing commercial Fe–N–C cathode electrocatalyst for anion-exchange membrane fuel cells, Nat. Energy 6 (2021) 834–843. https://doi.org/10.1038/s41560-021-00878-7.
[32] S. Huang, Z. Qiao, P. Sun, K. Qiao, K. Pei, L. Yang, H. Xu, S. Wang, Y. Huang, Y. Yan, D. Cao, The strain induced synergistic catalysis of FeN4 and MnN3 dual-site catalysts for oxygen reduction in proton- /anion- exchange membrane fuel cells, Appl. Catal. B 317 (2022) 121770. https://doi.org/10.1016/j.apcatb.2022.121770.
[33] P. Sun, K. Qiao, D. Li, X. Liu, H. Liu, L. Yang, H. Xu, Z. Zhuang, Y. Yan, D. Cao, Designing oxygen-doped Fe-N-C oxygen reduction catalysts for proton- and anion-exchange-membrane fuel cells, Chem. Catalysis 2 (2022) 2750–2763. https://doi.org/10.1016/j.checat.2022.09.009.
[34] P. Teppor, R. Jäger, M. Koppel, O. Volobujeva, R. Palm, M. Månsson, E. Härk, Z. Kochovski, J. Aruväli, K. Kooser, S. Granroth, T. Käämbre, J. Nerut, E. Lust, Unlocking the porosity of Fe–N–C catalysts using hydroxyapatite as a hard template en route to eco-friendly high-performance AEMFCs, J. Power Sources 591 (2024) 233816. https://doi.org/10.1016/j.jpowsour.2023.233816.
[35] X. Peng, V. Kashyap, B. Ng, S. Kurungot, L. Wang, J. Varcoe, W. Mustain, High-Performing PGM-Free AEMFC Cathodes from Carbon-Supported Cobalt Ferrite Nanoparticles, Catalysts 9 (2019) 264. https://doi.org/10.3390/catal9030264.
[36] L. Wang, M. Bellini, H.A. Miller, J.R. Varcoe, A high conductivity ultrathin anion-exchange membrane with 500+ h alkali stability for use in alkaline membrane fuel cells that can achieve 2 W cm−2 at 80 °C, J. Mater. Chem. A 6 (2018) 15404–15412. https://doi.org/10.1039/C8TA04783A.
[37] J. Lilloja, E. Kibena-Põldsepp, A. Sarapuu, J.C. Douglin, M. Käärik, J. Kozlova, P. Paiste, A. Kikas, J. Aruväli, J. Leis, V. Sammelselg, D.R. Dekel, K. Tammeveski, Transition-Metal- and Nitrogen-Doped Carbide-Derived Carbon/Carbon Nanotube Composites as Cathode Catalysts for Anion-Exchange Membrane Fuel Cells, ACS Catal. 11 (2021) 1920–1931. https://doi.org/10.1021/acscatal.0c03511.
[38] P.G. Santori, F.D. Speck, S. Cherevko, H.A. Firouzjaie, X. Peng, W.E. Mustain, F. Jaouen, High Performance FeNC and Mn-oxide/FeNC Layers for AEMFC Cathodes, J. Electrochem. Soc. 167 (2020) 134505. https://doi.org/10.1149/1945-7111/abb7e0.
[39] Y. Kumar, E. Kibena-Põldsepp, J. Kozlova, M. Rähn, A. Treshchalov, A. Kikas, V. Kisand, J. Aruväli, A. Tamm, J.C. Douglin, S.J. Folkman, I. Gelmetti, F.A. Garcés-Pineda, J.R. Galán-Mascarós, D.R. Dekel, K. Tammeveski, Bifunctional

Oxygen Electrocatalysis on Mixed Metal Phthalocyanine-Modified Carbon Nanotubes Prepared via Pyrolysis, ACS Appl. Mater. Interfaces 13 (2021) 41507–41516. https://doi.org/10.1021/acsami.1c06737.

[40] U. Sajjad, A. Sarapuu, J.C. Douglin, A. Kikas, A. Treshchalov, M. Käärik, J. Kozlova, J. Aruväli, J. Leis, V. Kisand, K. Kukli, D.R. Dekel, K. Tammeveski, Lignin-Derived Precious Metal-Free Electrocatalysts for Anion-Exchange Membrane Fuel Cell Application, ACS Catal. (2024) 9224–9234. https://doi.org/10.1021/acscatal.4c02136.

[41] H. Ren, Y. Wang, Y. Yang, X. Tang, Y. Peng, H. Peng, L. Xiao, J. Lu, H.D. Abruña, L. Zhuang, Fe/N/C Nanotubes with Atomic Fe Sites: A Highly Active Cathode Catalyst for Alkaline Polymer Electrolyte Fuel Cells, ACS Catal. 7 (2017) 6485–6492. https://doi.org/10.1021/acscatal.7b02340.

[42] J. Lilloja, E. Kibena-Põldsepp, A. Sarapuu, M. Käärik, J. Kozlova, P. Paiste, A. Kikas, A. Treshchalov, J. Leis, A. Tamm, V. Kisand, S. Holdcroft, K. Tammeveski, Transition metal and nitrogen-doped mesoporous carbons as cathode catalysts for anion-exchange membrane fuel cells, Appl. Catal. B 306 (2022) 121113. https://doi.org/10.1016/j.apcatb.2022.121113.

[43] L. Osmieri, C. Zafferoni, L. Wang, A.H.A. Monteverde Videla, A. Lavacchi, S. Specchia, Polypyrrole-Derived Fe−Co−N−C Catalyst for the Oxygen Reduction Reaction: Performance in Alkaline Hydrogen and Ethanol Fuel Cells, ChemElectroChem 5 (2018) 1954–1965. https://doi.org/10.1002/celc.201800420.

[44] S. Ratso, A. Zitolo, M. Käärik, M. Merisalu, A. Kikas, V. Kisand, M. Rähn, P. Paiste, J. Leis, V. Sammelselg, S. Holdcroft, F. Jaouen, K. Tammeveski, Non-precious metal cathodes for anion exchange membrane fuel cells from ball-milled iron and nitrogen doped carbide-derived carbons, Renew. Energy 167 (2021) 800–810. https://doi.org/10.1016/j.renene.2020.11.154.

[45] M. Mooste, E. Kibena-Põldsepp, V. Vassiljeva, A. Kikas, M. Käärik, J. Kozlova, V. Kisand, M. Külaviir, S. Cavaliere, J. Leis, A. Krumme, V. Sammelselg, S. Holdcroft, K. Tammeveski, Electrospun Polyacrylonitrile-Derived Co or Fe Containing Nanofibre Catalysts for Oxygen Reduction Reaction at the Alkaline Membrane Fuel Cell Cathode, ChemCatChem 12 (2020) 4568–4581. https://doi.org/10.1002/cctc.202000658.

[46] R. Sibul, E. Kibena-Põldsepp, S. Ratso, M. Kook, M.T. Sougrati, M. Käärik, M. Merisalu, J. Aruväli, P. Paiste, A. Treshchalov, J. Leis, V. Kisand, V. Sammelselg, S. Holdcroft, F. Jaouen, K. Tammeveski, Iron- and Nitrogen-Doped Graphene-Based Catalysts for Fuel Cell Applications, ChemElectroChem 7 (2020) 1739–1747. https://doi.org/10.1002/celc.202000011.

[47] J. Lilloja, M. Mooste, E. Kibena-Põldsepp, A. Sarapuu, B. Zulevi, A. Kikas, H.-M. Piirsoo, A. Tamm, V. Kisand, S. Holdcroft, A. Serov, K. Tammeveski, Mesoporous iron-nitrogen co-doped carbon material as cathode catalyst for the anion exchange membrane fuel cell, J. Power Sources Adv. 8 (2021) 100052. https://doi.org/10.1016/j.powera.2021.100052.

[48] H.-C. Huang, C.-Y. Su, K.-C. Wang, H.-Y. Chen, Y.-C. Chang, Y.-L. Chen, K.C.-W. Wu, C.-H. Wang, Nanostructured Cementite/Ferrous Sulfide Encapsulated Carbon with Heteroatoms for Oxygen Reduction in Alkaline Environment, ACS Sustainable Chem. Eng. 7 (2019) 3185–3194. https://doi.org/10.1021/acssuschemeng.8b05033.

[49] J. Sanetuntikul, S. Hyun, P. Ganesan, S. Shanmugam, Cobalt and nitrogen co-doped hierarchically porous carbon nanostructure: a bifunctional electrocatalyst for

oxygen reduction and evolution reactions, J. Mater. Chem. A 6 (2018) 24078–24085. https://doi.org/10.1039/C8TA08476A.
[50] R. Praats, M. Käärik, A. Kikas, V. Kisand, J. Aruväli, P. Paiste, M. Merisalu, A. Sarapuu, J. Leis, V. Sammelselg, J.C. Douglin, D.R. Dekel, K. Tammeveski, Electroreduction of oxygen on cobalt phthalocyanine-modified carbide-derived carbon/carbon nanotube composite catalysts, J. Solid State Electrochem. 25 (2021) 57–71. https://doi.org/10.1007/s10008-020-04543-z.
[51] R. Praats, M. Käärik, A. Kikas, V. Kisand, J. Aruväli, P. Paiste, M. Merisalu, J. Leis, V. Sammelselg, J.H. Zagal, S. Holdcroft, N. Nakashima, K. Tammeveski, Electrocatalytic oxygen reduction reaction on iron phthalocyanine-modified carbide-derived carbon/carbon nanotube composite electrocatalysts, Electrochim. Acta 334 (2020) 135575. https://doi.org/10.1016/j.electacta.2019.135575.
[52] J. Lilloja, E. Kibena-Põldsepp, A. Sarapuu, M. Kodali, Y. Chen, T. Asset, M. Käärik, M. Merisalu, P. Paiste, J. Aruväli, A. Treshchalov, M. Rähn, J. Leis, V. Sammelselg, S. Holdcroft, P. Atanassov, K. Tammeveski, Cathode Catalysts Based on Cobalt- and Nitrogen-Doped Nanocarbon Composites for Anion Exchange Membrane Fuel Cells, ACS Appl. Energy Mater. 3 (2020) 5375–5384. https://doi.org/10.1021/acsaem.0c00381.
[53] Y. Kumar, E. Kibena-Põldsepp, M. Mooste, J. Kozlova, A. Kikas, J. Aruväli, M. Käärik, V. Kisand, J. Leis, A. Tamm, S. Holdcroft, J.H. Zagal, K. Tammeveski, Iron and Nickel Phthalocyanine-Modified Nanocarbon Materials as Cathode Catalysts for Anion-Exchange Membrane Fuel Cells and Zinc-Air Batteries, ChemElectroChem 9 (2022) e202200717. https://doi.org/10.1002/celc.202200717.
[54] J. Lilloja, M. Mooste, E. Kibena-Põldsepp, A. Sarapuu, A. Kikas, V. Kisand, M. Käärik, J. Kozlova, A. Treshchalov, P. Paiste, J. Aruväli, J. Leis, A. Tamm, S. Holdcroft, K. Tammeveski, Cobalt-, iron- and nitrogen-containing ordered mesoporous carbon-based catalysts for anion-exchange membrane fuel cell cathode, Electrochim. Acta 439 (2023) 141676. https://doi.org/10.1016/j.electacta.2022.141676.
[55] S. Akula, M. Mooste, J. Kozlova, M. Käärik, A. Treshchalov, A. Kikas, V. Kisand, J. Aruväli, P. Paiste, A. Tamm, J. Leis, K. Tammeveski, Transition metal (Fe, Co, Mn, Cu) containing nitrogen-doped porous carbon as efficient oxygen reduction electrocatalysts for anion exchange membrane fuel cells, Chem. Eng. J. 458 (2023) 141468. https://doi.org/10.1016/j.cej.2023.141468.
[56] R. Kumar, M. Mooste, Z. Ahmed, S. Akula, I. Zekker, M. Marandi, M. Käärik, J. Leis, A. Kikas, A. Treshchalov, M. Otsus, J. Aruväli, V. Kisand, A. Tamm, K. Tammeveski, Highly active ZIF-8@CNT composite catalysts as cathode materials for anion exchange membrane fuel cells, Ind. Chem. Mater. 1 (2023) 526–541. https://doi.org/10.1039/D3IM00081H.
[57] Z. Ahmed, S. Akula, J. Kozlova, H.-M. Piirsoo, K. Kukli, A. Kikas, V. Kisand, M. Käärik, J. Leis, A. Treshchalov, J. Aruväli, K. Tammeveski, Hybrid high-performance oxygen reduction reaction Fe–N–C electrocatalyst for anion exchange membrane fuel cells, Int. J. Hydrogen Energy 62 (2024) 849–858. https://doi.org/10.1016/j.ijhydene.2024.03.055.
[58] I. Palm, R. Sibul, E. Kibena-Põldsepp, M. Mooste, J. Lilloja, M. Käärik, J. Kozlova, A. Kikas, A. Treshchalov, J. Leis, V. Kisand, A. Tamm, N. Bibent, F. Jaouen, S. Holdcroft, K. Tammeveski, ZIF-8 derived iron-, sulphur-, and nitrogen-doped catalysts for anion-exchange membrane fuel cell application, Renew. Energy 228 (2024) 120613. https://doi.org/10.1016/j.renene.2024.120613.

[59] A. J. Bard, L.R. Faulkner, Electrochemical Methods: Fundamentals and Applications 2nd ed., New York: Wiley, 2001
[60] J. Masa, C. Batchelor-McAuley, W. Schuhmann, R.G. Compton, Koutecky-Levich analysis applied to nanoparticle modified rotating disk electrodes: Electrocatalysis or misinterpretation, Nano Res. 7 (2014) 71–78. https://doi.org/10.1007/s12274-013-0372-0.
[61] T. Lazaridis, B.M. Stühmeier, H.A. Gasteiger, H.A. El-Sayed, Capabilities and limitations of rotating disk electrodes versus membrane electrode assemblies in the investigation of electrocatalysts, Nat. Catal. 5 (2022) 363–373. https://doi.org/10.1038/s41929-022-00776-5.
[62] J.-Q. Zhong, K.-J. Yan, J. Yang, W.-H. Yang, X.-D. Yang, Microenvironment Alters the Oxygen Reduction Activity of Metal/N/C Catalysts at the Triple-Phase Boundary, ACS Catal. 12 (2022) 9003–9010. https://doi.org/10.1021/acscatal.2c00362.
[63] J. Barrio, A. Pedersen, S.Ch. Sarma, A. Bagger, M. Gong, S. Favero, C.-X. Zhao, R. Garcia-Serres, A.Y. Li, Q. Zhang, F. Jaouen, F. Maillard, A. Kucernak, I.E.L. Stephens, M.-M. Titirici, FeNC Oxygen Reduction Electrocatalyst with High Utilization Penta-Coordinated Sites, Adv. Mater. 35 (2023) 2211022. https://doi.org/10.1002/adma.202211022.
[64] A. Pedersen, A. Bagger, J. Barrio, F. Maillard, I.E.L. Stephens, M.-M. Titirici, Atomic metal coordinated to nitrogen-doped carbon electrocatalysts for proton exchange membrane fuel cells: a perspective on progress, pitfalls and prospectives, J. Mater. Chem. A 11 (2023) 23211–23222. https://doi.org/10.1039/D3TA04711C.
[65] H.-S. Shiau, I. Zenyuk, A. Weber, Water Management in an Alkaline-Exchange-Membrane Fuel Cell, ECS Trans. 69 (2015) 985–994. https://doi.org/10.1149/06917.0985ecst.
[66] T.J. Omasta, L. Wang, X. Peng, C.A. Lewis, J.R. Varcoe, W.E. Mustain, Importance of balancing membrane and electrode water in anion exchange membrane fuel cells, J. Power Sources 375 (2018) 205–213. https://doi.org/10.1016/j.jpowsour.2017.05.006.
[67] J. Zhang, Q. Huang, J. Wang, J. Wang, J. Zhang, Y. Zhao, Supported dual-atom catalysts: Preparation, characterization, and potential applications, Chinese J. Catal. 41 (2020) 783–798. https://doi.org/10.1016/S1872-2067(20)63536-7.
[68] A. Kozhushner, N. Zion, L. Elbaz, Methods for assessment and measurement of the active site density in platinum group metal–free oxygen reduction reaction catalysts, Curr. Opin. Electrochem. 25 (2021) 100620. https://doi.org/10.1016/j.coelec.2020.08.002.
[69] M.C. Biesinger, B.P. Payne, A.P. Grosvenor, L.W.M. Lau, A.R. Gerson, R.St.C. Smart, Resolving surface chemical states in XPS analysis of first row transition metals, oxides and hydroxides: Cr, Mn, Fe, Co and Ni, Appl. Surf. Sci. 257 (2011) 2717–2730. https://doi.org/10.1016/j.apsusc.2010.10.051.
[70] Q. Jia, N. Ramaswamy, U. Tylus, K. Strickland, J. Li, A. Serov, K. Artyushkova, P. Atanassov, J. Anibal, C. Gumeci, S.C. Barton, M.-T. Sougrati, F. Jaouen, B. Halevi, S. Mukerjee, Spectroscopic insights into the nature of active sites in iron–nitrogen–carbon electrocatalysts for oxygen reduction in acid, Nano Energy 29 (2016) 65–82. https://doi.org/10.1016/j.nanoen.2016.03.025.
[71] D.-W. Wang, D. Su, Heterogeneous nanocarbon materials for oxygen reduction reaction, Energy Environ. Sci. 7 (2014) 576–591. https://doi.org/10.1039/C3EE43463J.

[72] P. Pang, H. Han, L. Hu, C. Guo, Y. Gao, Y. Xie, The calculations of pore structure parameters from gas adsorption experiments of shales: Which models are better?, J. Nat. Gas Sci. Eng. 94 (2021) 104060. https://doi.org/10.1016/j.jngse.2021.104060.
[73] G.Yu. Gor, M. Thommes, K.A. Cychosz, A.V. Neimark, Quenched solid density functional theory method for characterization of mesoporous carbons by nitrogen adsorption, Carbon 50 (2012) 1583–1590. https://doi.org/10.1016/j.carbon.2011.11.037.
[74] A.A.K. King, B.R. Davies, N. Noorbehesht, P. Newman, T.L. Church, A.T. Harris, J.M. Razal, A.I. Minett, A New Raman Metric for the Characterisation of Graphene oxide and its Derivatives, Sci. Rep. 6 (2016) 19491. https://doi.org/10.1038/srep19491.
[75] M. Sforna, M. Zuilen, P. Philippot, Structural characterization by Raman hyperspectral mapping of organic carbon in the 3.46 billion-year-old Apex chert, Western Australia, Geochim. Cosmochim. Acta 124 (2013) 18–33. https://doi.org/10.1016/j.gca.2013.09.031.
[76] L.G. Cançado, A. Jorio, E.H.M. Ferreira, F. Stavale, C.A. Achete, R.B. Capaz, M.V.O. Moutinho, A. Lombardo, T.S. Kulmala, A.C. Ferrari, Quantifying Defects in Graphene via Raman Spectroscopy at Different Excitation Energies, Nano Lett. 11 (2011) 3190–3196. https://doi.org/10.1021/nl201432g.
[77] J. Jankovic, J. Stumper, (Eds.) PEM Fuel Cells: Characterization and Modeling, Berlin, Boston: De Gruyter (2023). https://doi.org/10.1515/9783110622720.
[78] L. Osmieri, L. Pezzolato, S. Specchia, Recent trends on the application of PGM-free catalysts at the cathode of anion exchange membrane fuel cells, Curr. Opin. Electrochem. 9 (2018) 240–256. https://doi.org/10.1016/j.coelec.2018.05.011.
[79] DOE National Clean Hydrogen Strategy and Roadmap, (2022).
[80] R. Jasinski, A New Fuel Cell Cathode Catalyst, Nature 201 (1964) 1212–1213. https://doi.org/10.1038/2011212a0.
[81] S. Gupta, D. Tryk, I. Bae, W. Aldred, E. Yeager, Heat-treated polyacrylonitrile-based catalysts for oxygen electroreduction, J. Appl. Electrochem. 19 (1989) 19–27. https://doi.org/10.1007/BF01039385.
[82] Y. Shao, J.-P. Dodelet, G. Wu, P. Zelenay, PGM-Free Cathode Catalysts for PEM Fuel Cells: A Mini-Review on Stability Challenges, Adv. Mater. 31 (2019) 1807615. https://doi.org/10.1002/adma.201807615.
[83] D. Malko, T. Lopes, E. Symianakis, A.R. Kucernak, The intriguing poison tolerance of non-precious metal oxygen reduction reaction (ORR) catalysts, J. Mater. Chem. A 4 (2015) 142–152. https://doi.org/10.1039/C5TA05794A.
[84] Y. Chen, Y. Huang, M. Xu, T. Asset, X. Yan, K. Artyushkova, M. Kodali, E. Murphy, A. Ly, X. Pan, I.V. Zenyuk, P. Atanassov, Catalysts by pyrolysis: Direct observation of transformations during re-pyrolysis of transition metal-nitrogen-carbon materials leading to state-of-the-art platinum group metal-free electrocatalyst, Mater. Today 53 (2022) 58–70. https://doi.org/10.1016/j.mattod.2022.01.016.
[85] A. Sarapuu, E. Kibena-Põldsepp, M. Borghei, K. Tammeveski, Electrocatalysis of oxygen reduction on heteroatom-doped nanocarbons and transition metal–nitrogen–carbon catalysts for alkaline membrane fuel cells, J. Mater. Chem. A 6 (2018) 776–804. https://doi.org/10.1039/C7TA08690C.
[86] S. Wang, C. Dai, J. Li, L. Zhao, Z. Ren, Y. Ren, Y. Qiu, J. Yu, The effect of different nitrogen sources on the electrocatalytic properties of nitrogen-doped electro-

spun carbon nanofibers for the oxygen reduction reaction, Int. J. Hydrogen Energy 40 (2015) 4673–4682. https://doi.org/10.1016/j.ijhydene.2015.02.031.
[87] A. Sarapuu, J. Lilloja, S. Akula, J.H. Zagal, S. Specchia, K. Tammeveski, Recent Advances in Non-Precious Metal Single-Atom Electrocatalysts for Oxygen Reduction Reaction in Low-Temperature Polymer-Electrolyte Fuel Cells, ChemCatChem 15 (2023) e202300849. https://doi.org/10.1002/cctc.202300849.
[88] S. Ratso, I. Kruusenberg, M. Käärik, M. Kook, L. Puust, R. Saar, J. Leis, K. Tammeveski, Highly efficient transition metal and nitrogen co-doped carbide-derived carbon electrocatalysts for anion exchange membrane fuel cells, J. Power Sources 375 (2018) 233–243. https://doi.org/10.1016/j.jpowsour.2017.08.046.
[89] J. Lilloja, E. Kibena-Põldsepp, A. Sarapuu, M. Kodali, Y. Chen, T. Asset, M. Käärik, M. Merisalu, P. Paiste, J. Aruväli, A. Treshchalov, M. Rähn, J. Leis, V. Sammelselg, S. Holdcroft, P. Atanassov, K. Tammeveski, Cathode Catalysts Based on Cobalt- and Nitrogen-Doped Nanocarbon Composites for Anion Exchange Membrane Fuel Cells, ACS Appl. Energy Mater. 3 (2020) 5375–5384. https://doi.org/10.1021/acsaem.0c00381.
[90] K. Kisand, A. Sarapuu, J.C. Douglin, A. Kikas, A. Treshchalov, M. Käärik, H.-M. Piirsoo, P. Paiste, J. Aruväli, J. Leis, V. Kisand, A. Tamm, D.R. Dekel, K. Tammeveski, Templated Nitrogen-, Iron-, and Cobalt-Doped Mesoporous Nanocarbon Derived from an Alkylresorcinol Mixture for Anion-Exchange Membrane Fuel Cell Application, ACS Catal. 12 (2022) 14050–14061. https://doi.org/10.1021/acscatal.2c03683.
[91] H. Adabi, P.G. Santori, A. Shakouri, X. Peng, K. Yassin, I.G. Rasin, S. Brandon, D.R. Dekel, N.U. Hassan, M.-T. Sougrati, A. Zitolo, J.R. Varcoe, J.R. Regalbuto, F. Jaouen, W.E. Mustain, Understanding how single-atom site density drives the performance and durability of PGM-free Fe–N–C cathodes in anion exchange membrane fuel cells, Mater. Today Adv. 12 (2021) 100179. https://doi.org/10.1016/j.mtadv.2021.100179.
[92] M. Ferrandon, X. Wang, A.J. Kropf, D.J. Myers, G. Wu, C.M. Johnston, P. Zelenay, Stability of iron species in heat-treated polyaniline–iron–carbon polymer electrolyte fuel cell cathode catalysts, Electrochim. Acta 110 (2013) 282–291. https://doi.org/10.1016/j.electacta.2013.03.183.
[93] L. Osmieri, D.A. Cullen, H.T. Chung, R.K. Ahluwalia, K.C. Neyerlin, Durability evaluation of a Fe–N–C catalyst in polymer electrolyte fuel cell environment via accelerated stress tests, Nano Energy 78 (2020) 105209. https://doi.org/10.1016/j.nanoen.2020.105209.
[94] K. Liu, Z. Qiao, S. Hwang, Z. Liu, H. Zhang, D. Su, H. Xu, G. Wu, G. Wang, Mn- and N- doped carbon as promising catalysts for oxygen reduction reaction: Theoretical prediction and experimental validation, Appl. Catal. B 243 (2019) 195–203. https://doi.org/10.1016/j.apcatb.2018.10.034.
[95] J. Li, M. Chen, D.A. Cullen, S. Hwang, M. Wang, B. Li, K. Liu, S. Karakalos, M. Lucero, H. Zhang, C. Lei, H. Xu, G.E. Sterbinsky, Z. Feng, D. Su, K.L. More, G. Wang, Z. Wang, G. Wu, Atomically dispersed manganese catalysts for oxygen reduction in proton-exchange membrane fuel cells, Nat. Catal. 1 (2018) 935–945. https://doi.org/10.1038/s41929-018-0164-8.
[96] K. Kumar, L. Dubau, M. Mermoux, J. Li, A. Zitolo, J. Nelayah, F. Jaouen, F. Maillard, On the Influence of Oxygen on the Degradation of Fe-N-C Catalysts, Angew. Chem. Int. Ed. 59 (2020) 3235–3243. https://doi.org/10.1002/anie.201912451.

[97] Z. Chen, X. Liao, C. Sun, K. Zhao, D. Ye, J. Li, G. Wu, J. Fang, H. Zhao, J. Zhang, Enhanced performance of atomically dispersed dual-site Fe-Mn electrocatalysts through cascade reaction mechanism, Appl. Catal. B 288 (2021) 120021. https://doi.org/10.1016/j.apcatb.2021.120021.
[98] J. Wang, Z. Huang, W. Liu, C. Chang, H. Tang, Z. Li, W. Chen, C. Jia, T. Yao, S. Wei, Y. Wu, Y. Li, Design of N-Coordinated Dual-Metal Sites: A Stable and Active Pt-Free Catalyst for Acidic Oxygen Reduction Reaction, J. Am. Chem. Soc. 139 (2017) 17281–17284. https://doi.org/10.1021/jacs.7b10385.
[99] Q. Ma, H. Jin, J. Zhu, Z. Li, H. Xu, B. Liu, Z. Zhang, J. Ma, S. Mu, Stabilizing Fe–N–C Catalysts as Model for Oxygen Reduction Reaction, Adv. Sci. 8 (2021) 2102209. https://doi.org/10.1002/advs.202102209.
[100] F. Jaouen, D. Jones, N. Coutard, V. Artero, P. Strasser, A. Kucernak, Toward Platinum Group Metal-Free Catalysts for Hydrogen/Air Proton-Exchange Membrane Fuel Cells: Catalyst activity in platinum-free substitute cathode and anode materials, Johnson Matthey Technology Review 62 (2018) 231–255. https://doi.org/10.1595/205651318X696828.
[101] D. Menga, J.L. Low, Y.-S. Li, I. Arčon, B. Koyutürk, F. Wagner, F. Ruiz-Zepeda, M. Gaberšček, B. Paulus, T.-P. Fellinger, Resolving the Dilemma of Fe–N–C Catalysts by the Selective Synthesis of Tetrapyrrolic Active Sites via an Imprinting Strategy, J. Am. Chem. Soc. 143 (2021) 18010–18019. https://doi.org/10.1021/jacs.1c04884.
[102] Y. Hu, J.O. Jensen, W. Zhang, L.N. Cleemann, W. Xing, N.J. Bjerrum, Q. Li, Hollow Spheres of Iron Carbide Nanoparticles Encased in Graphitic Layers as Oxygen Reduction Catalysts, Angew. Chem. Int. Ed. 53 (2014) 3675–3679. https://doi.org/10.1002/anie.201400358.
[103] K. Kumar, L. Dubau, F. Jaouen, F. Maillard, Review on the Degradation Mechanisms of Metal-N-C Catalysts for the Oxygen Reduction Reaction in Acid Electrolyte: Current Understanding and Mitigation Approaches, Chem. Rev. 123 (2023) 9265-9326. https://doi.org/10.1021/acs.chemrev.2c00685.
[104] N. Daems, X. Sheng, I.F.J. Vankelecom, P.P. Pescarmona, Metal-free doped carbon materials as electrocatalysts for the oxygen reduction reaction, J. Mater. Chem. A 2 (2014) 4085–4110. https://doi.org/10.1039/C3TA14043A.
[105] Y. Yang, C.R. Peltier, R. Zeng, R. Schimmenti, Q. Li, X. Huang, Z. Yan, G. Potsi, R. Selhorst, X. Lu, W. Xu, M. Tader, A.V. Soudackov, H. Zhang, M. Krumov, E. Murray, P. Xu, J. Hitt, L. Xu, H.-Y. Ko, B.G. Ernst, C. Bundschu, A. Luo, D. Markovich, M. Hu, C. He, H. Wang, J. Fang, R.A. DiStasio, L.F. Kourkoutis, A. Singer, K.J.T. Noonan, L. Xiao, L. Zhuang, B.S. Pivovar, P. Zelenay, E. Herrero, J.M. Feliu, J. Suntivich, E.P. Giannelis, S. Hammes-Schiffer, T. Arias, M. Mavrikakis, T.E. Mallouk, J.D. Brock, D.A. Muller, F.J. DiSalvo, G.W. Coates, H.D. Abruña, Electrocatalysis in Alkaline Media and Alkaline Membrane-Based Energy Technologies, Chem. Rev. 122 (2022) 6117–6321. https://doi.org/10.1021/acs.chemrev.1c00331.
[106] A.C. Ramírez-Pérez, J. Quílez-Bermejo, J.M. Sieben, E. Morallón, D. Cazorla-Amorós, Effect of Nitrogen-Functional Groups on the ORR Activity of Activated Carbon Fiber-Polypyrrole-Based Electrodes, Electrocatalysis 9 (2018) 697–705. https://doi.org/10.1007/s12678-018-0478-y.
[107] A. Mehmood, J. Pampel, G. Ali, H.Y. Ha, F. Ruiz-Zepeda, T.-P. Fellinger, Facile Metal Coordination of Active Site Imprinted Nitrogen Doped Carbons for the

Conservative Preparation of Non-Noble Metal Oxygen Reduction Electrocatalysts, Adv. Energy Mater. 8 (2018) 1701771. https://doi.org/10.1002/aenm.201701771.
[108] D. Menga, F. Ruiz-Zepeda, L. Moriau, M. Šala, F. Wagner, B. Koyutürk, M. Bele, U. Petek, N. Hodnik, M. Gaberšček, T.-P. Fellinger, Active-Site Imprinting: Preparation of Fe–N–C Catalysts from Zinc Ion–Templated Ionothermal Nitrogen-Doped Carbons, Adv. Energy Mater. 9 (2019) 1902412. https://doi.org/10.1002/aenm.201902412.
[109] Y. Ye, F. Cai, H. Li, H. Wu, G. Wang, Y. Li, S. Miao, S. Xie, R. Si, J. Wang, X. Bao, Surface functionalization of ZIF-8 with ammonium ferric citrate toward high exposure of Fe-N active sites for efficient oxygen and carbon dioxide electroreduction, Nano Energy 38 (2017) 281–289. https://doi.org/10.1016/j.nanoen.2017.05.042.
[110] S.H. Lee, J. Kim, D.Y. Chung, J.M. Yoo, H.S. Lee, M.J. Kim, B.S. Mun, S.G. Kwon, Y.-E. Sung, T. Hyeon, Design Principle of Fe–N–C Electrocatalysts: How to Optimize Multimodal Porous Structures?, J. Am. Chem. Soc. 141 (2019) 2035–2045. https://doi.org/10.1021/jacs.8b11129.
[111] F. Rodríguez-Reinoso, M. Molina-Sabio, M.T. González, The use of steam and CO2 as activating agents in the preparation of activated carbons, Carbon 33 (1995) 15–23. https://doi.org/10.1016/0008-6223(94)00100-E.
[112] F. Rodriguez-Reinoso, Controlled Gasification of Carbon and Pore Structure Development, in: J. Lahaye, P. Ehrburger (Eds.), Fundamental Issues in Control of Carbon Gasification Reactivity, Springer Netherlands, Dordrecht, 1991: pp. 533–571. https://doi.org/10.1007/978-94-011-3310-4_26.
[113] J. Wang, S. Kaskel, KOH activation of carbon-based materials for energy storage, J. Mater. Chem. 22 (2012) 23710–23725. https://doi.org/10.1039/C2JM34066F.
[114] Y. Mun, M.J. Kim, S.-A. Park, E. Lee, Y. Ye, S. Lee, Y.-T. Kim, S. Kim, O.-H. Kim, Y.-H. Cho, Y.-E. Sung, J. Lee, Soft-template synthesis of mesoporous non-precious metal catalyst with Fe-Nx/C active sites for oxygen reduction reaction in fuel cells, Appl. Catal. B 222 (2018) 191–199. https://doi.org/10.1016/j.apcatb.2017.10.015.
[115] N. Díez, M. Sevilla, A.B. Fuertes, Synthesis strategies of templated porous carbons beyond the silica nanocasting technique, Carbon 178 (2021) 451–476. https://doi.org/10.1016/j.carbon.2021.03.029.
[116] M. Inagaki, S. Kobayashi, F. Kojin, N. Tanaka, T. Morishita, B. Tryba, Pore structure of carbons coated on ceramic particles, Carbon 42 (2004) 3153–3158. https://doi.org/10.1016/j.carbon.2004.07.029.
[117] T. Morishita, Y. Soneda, T. Tsumura, M. Inagaki, Preparation of porous carbons from thermoplastic precursors and their performance for electric double layer capacitors, Carbon 44 (2006) 2360–2367. https://doi.org/10.1016/j.carbon.2006.04.030.
[118] T. Morishita, T. Tsumura, M. Toyoda, J. Przepiórski, A.W. Morawski, H. Konno, M. Inagaki, A review of the control of pore structure in MgO-templated nanoporous carbons, Carbon 48 (2010) 2690–2707. https://doi.org/10.1016/j.carbon.2010.03.064.
[119] M. Anzai, T. Morishita, Y. Shodai, Method for producing porous carbon, and electrode and catalyst support containing porous carbon produced by said production method, EP3816105A4, 2021. https://patents.google.com/patent/EP3816105A4/ en (accessed April 6, 2024).

[120] J. Pampel, C. Denton, T.-P. Fellinger, Glucose derived ionothermal carbons with tailor-made porosity, Carbon 107 (2016) 288–296. https://doi.org/10.1016/j.carbon.2016.06.009.
[121] B. Koyuturk, E. M. Farber, F. E. Wagner, T.-P. Fellinger, D. Eisenberg, A simple decagram-scale synthesis of an atomically dispersed, hierarchically porous Fe–N–C catalyst for acidic ORR, J. Mater. Chem. A 10 (2022) 19859–19867. https://doi.org/10.1039/D2TA00925K.
[122] C.H. Choi, S.Y. Lee, S.H. Park, S.I. Woo, Highly active N-doped-CNTs grafted on Fe/C prepared by pyrolysis of dicyandiamide on Fe2O3/C for electrochemical oxygen reduction reaction, Appl. Catal. B 103 (2011) 362–368. https://doi.org/10.1016/j.apcatb.2011.01.043.
[123] C. Chao, M. Gao, Flame retardancy and thermal properties of octavinylsilsesquioxane/polycarbonate composites, J. Therm. Anal. Calorim. 128 (2017) 1125–1133.
[124] L. Zhou, J. Chang, Z. Lin, C. Zhang, D. Chen, J. Zhang, Y. Hao, Investigation of Fe2+-incorporating organic–inorganic hybrid perovskites from first principles and experiments, RSC Adv. 7 (2017) 54586–54593. https://doi.org/10.1039/C7RA11514H.
[125] J. Li, Z. Li, J. Tong, C. Xia, F. Li, Nitrogen-doped ordered mesoporous carbon sphere with short channel as an efficient metal-free catalyst for oxygen reduction reaction, RSC Adv. 5 (2015) 70010–70016. https://doi.org/10.1039/C5RA10484J.
[126] G. Wu, P. Zelenay, Nanostructured Nonprecious Metal Catalysts for Oxygen Reduction Reaction, Acc. Chem. Res. 46 (2013) 1878–1889. https://doi.org/10.1021/ar400011z.
[127] A. Sarapuu, L. Samolberg, K. Kreek, M. Koel, L. Matisen, K. Tammeveski, Cobalt- and iron-containing nitrogen-doped carbon aerogels as non-precious metal catalysts for electrochemical reduction of oxygen, J. Electroanal. Chem. 746 (2015) 9–17. https://doi.org/10.1016/j.jelechem.2015.03.021.
[128] P. Xu, W. Chen, Q. Wang, T. Zhu, M. Wu, J. Qiao, Z. Chen, J. Zhang, Effects of transition metal precursors (Co, Fe, Cu, Mn, or Ni) on pyrolyzed carbon supported metal-aminopyrine electrocatalysts for oxygen reduction reaction, RSC Adv. 5 (2014) 6195–6206. https://doi.org/10.1039/C4RA11643G.
[129] G. Wu, K.L. More, C.M. Johnston, P. Zelenay, High-Performance Electrocatalysts for Oxygen Reduction Derived from Polyaniline, Iron, and Cobalt, Science 332 (2011) 443–447. https://doi.org/10.1126/science.1200832.
[130] G. Wu, C.M. Johnston, N.H. Mack, K. Artyushkova, M. Ferrandon, M. Nelson, J.S. Lezama-Pacheco, S.D. Conradson, K.L. More, D.J. Myers, P. Zelenay, Synthesis–structure–performance correlation for polyaniline–Me–C non-precious metal cathode catalysts for oxygen reduction in fuel cells, J. Mater. Chem. 21 (2011) 11392–11405. https://doi.org/10.1039/C0JM03613G.
[131] K. Ai, Y. Liu, C. Ruan, L. Lu, G. (Max) Lu, Sp2 C-Dominant N-Doped Carbon Sub-micrometer Spheres with a Tunable Size: A Versatile Platform for Highly Efficient Oxygen-Reduction Catalysts, Adv. Mater. 25 (2013) 998–1003. https://doi.org/10.1002/adma.201203923.
[132] U. Tylus, Q. Jia, K. Strickland, N. Ramaswamy, A. Serov, P. Atanassov, S. Mukerjee, Elucidating Oxygen Reduction Active Sites in Pyrolyzed Metal–Nitrogen Coordinated Non-Precious-Metal Electrocatalyst Systems, J. Phys. Chem. C 118 (2014) 8999–9008. https://doi.org/10.1021/jp500781v.

[133] X.-H. Li, S. Kurasch, U. Kaiser, M. Antonietti, Synthesis of Monolayer-Patched Graphene from Glucose, Angew. Chem. Int. Ed. 51 (2012) 9689–9692. https://doi.org/10.1002/anie.201203207.
[134] Q. Li, D. Xu, X. Ou, F. Yan, Nitrogen-Doped Graphitic Porous Carbon Nanosheets Derived from In Situ Formed g-C3N4 Templates for the Oxygen Reduction Reaction, Chem. Asian J. 12 (2017) 1816–1823. https://doi.org/10.1002/asia.201700586.
[135] C. Hu, Y. Zhou, R. Ma, Q. Liu, J. Wang, Reactive template synthesis of nitrogen-doped graphene-like carbon nanosheets derived from hydroxypropyl methylcellulose and dicyandiamide as efficient oxygen reduction electrocatalysts, J. Power Sources 345 (2017) 120–130. https://doi.org/10.1016/j.jpowsour.2017.01.124.
[136] K. Strickland, E. Miner, Q. Jia, U. Tylus, N. Ramaswamy, W. Liang, M.-T. Sougrati, F. Jaouen, S. Mukerjee, Highly active oxygen reduction non-platinum group metal electrocatalyst without direct metal–nitrogen coordination, Nat. Commun. 6 (2015) 7343. https://doi.org/10.1038/ncomms8343.
[137] H.-J. Niu, L. Zhang, J.-J. Feng, Q.-L. Zhang, H. Huang, A.-J. Wang, Graphene-encapsulated cobalt nanoparticles embedded in porous nitrogen-doped graphitic carbon nanosheets as efficient electrocatalysts for oxygen reduction reaction, J. Colloid Interface Sci. 552 (2019) 744–751. https://doi.org/10.1016/j.jcis.2019.05.099.
[138] C.V. Rao, C.R. Cabrera, Y. Ishikawa, In Search of the Active Site in Nitrogen-Doped Carbon Nanotube Electrodes for the Oxygen Reduction Reaction, J. Phys. Chem. Lett. 1 (2010) 2622–2627. https://doi.org/10.1021/jz100971v.
[139] K. Artyushkova, A. Serov, S. Rojas-Carbonell, P. Atanassov, Chemistry of Multitudinous Active Sites for Oxygen Reduction Reaction in Transition Metal–Nitrogen–Carbon Electrocatalysts, J. Phys. Chem. C 119 (2015) 25917–25928. https://doi.org/10.1021/acs.jpcc.5b07653.
[140] M. Mooste, E. Kibena-Põldsepp, V. Vassiljeva, M. Merisalu, M. Kook, A. Treshchalov, V. Kisand, M. Uibu, A. Krumme, V. Sammelselg, K. Tammeveski, Electrocatalysts for oxygen reduction reaction based on electrospun polyacrylonitrile, styrene–acrylonitrile copolymer and carbon nanotube composite fibres, J. Mater. Sci. 54 (2019) 11618–11634. https://doi.org/10.1007/s10853-019-03725-z.
[141] Y. He, S. Liu, C. Priest, Q. Shi, G. Wu, Atomically dispersed metal–nitrogen–carbon catalysts for fuel cells: advances in catalyst design, electrode performance, and durability improvement, Chem. Soc. Rev. 49 (2020) 3484–3524. https://doi.org/10.1039/C9CS00903E.
[142] M. Groenewolt, M. Antonietti, Synthesis of g-C3N4 Nanoparticles in Mesoporous Silica Host Matrices, Adv. Mater. 17 (2005) 1789–1792. https://doi.org/10.1002/adma.200401756.
[143] B. Zhong, L. Zhang, J. Yu, K. Fan, Ultrafine iron-cobalt nanoparticles embedded in nitrogen-doped porous carbon matrix for oxygen reduction reaction and zinc-air batteries, J. Colloid Interface Sci. 546 (2019) 113–121. https://doi.org/10.1016/j.jcis.2019. 03.038.
[144] S. Samad, K.S. Loh, W.Y. Wong, W. Sudarsono, T.K. Lee, W.R. Wan Daud, Effect of various Fe/Co ratios and annealing temperatures on a Fe/Co catalyst supported with nitrogen-doped reduced graphene oxide towards the oxygen reduction reaction, J. Alloys Compd. 816 (2020) 152573. https://doi.org/10.1016/j.jallcom.2019.152573.

[145] L. Chen, Y. Zhang, L. Dong, W. Yang, X. Liu, L. Long, C. Liu, S. Dong, J. Jia, Synergistic effect between atomically dispersed Fe and Co metal sites for enhanced oxygen reduction reaction, J. Mater. Chem. A 8 (2020) 4369–4375. https://doi.org/10.1039/C9TA12516G.
[146] Y. Yang, H. Zhang, Z. Liang, Y. Yin, B. Mei, F. Song, F. Sun, S. Gu, Z. Jiang, Y. Wu, Z. Zhu, Role of local coordination in bimetallic sites for oxygen reduction: A theoretical analysis, J. Energy Chem. 44 (2020) 131–137. https://doi.org/10.1016/j.jechem.2019.08.009.
[147] N.A. Galiote, F.E.R. Oliveira, F.H.B. Lima, FeCo-N-C oxygen reduction electrocatalysts: Activity of the different compounds produced during the synthesis via pyrolysis, Appl. Catal. B 253 (2019) 300–308. https://doi.org/10.1016/j.apcatb.2019.04.057.
[148] M. Shao, Q. Chang, J.-P. Dodelet, R. Chenitz, Recent Advances in Electrocatalysts for Oxygen Reduction Reaction, Chem. Rev. 116 (2016) 3594–3657. https://doi.org/10 1021/acs.chemrev.5b00462.
[149] A. Zitolo, N. Ranjbar-Sahraie, T. Mineva, J. Li, Q. Jia, S. Stamatin, G.F. Harrington, S.M. Lyth, P. Krtil, S. Mukerjee, E. Fonda, F. Jaouen, Identification of catalytic sites in cobalt-nitrogen-carbon materials for the oxygen reduction reaction, Nat. Commun. 8 (2017) 957. https://doi.org/10.1038/s41467-017-01100-7.
[150] M.S. Thorum, J.M. Hankett, A.A. Gewirth, Poisoning the Oxygen Reduction Reaction on Carbon-Supported Fe and Cu Electrocatalysts: Evidence for Metal-Centered Activity, J. Phys. Chem. Lett. 2 (2011) 295–298. https://doi.org/10.-1021/jz1016284.
[151] Y. He, S. Liu, C. Priest, Q. Shi, G. Wu, Atomically dispersed metal–nitrogen–carbon catalysts for fuel cells: advances in catalyst design, electrode performance, and durability improvement, Chem. Soc. Rev. 49 (2020) 3484–3524. https://doi.org/10.1039/C9CS00903E.
[152] Y. Liu, H. Jiang, Y. Zhu, X. Yang, C. Li, Transition metals (Fe, Co, and Ni) encapsulated in nitrogen-doped carbon nanotubes as bi-functional catalysts for oxygen electrode reactions, J. Mater. Chem. A 4 (2016) 1694–1701. https://doi.org/10.1039/C5TA10551J.
[153] B. Britton, S. Holdcroft, The Control and Effect of Pore Size Distribution in AEMFC Catalyst Layers, J. Electrochem. Soc. 163 (2016) F353–F358. https://doi.org/10.1149/2.0421605jes.
[154] A. Serov, I.V. Zenyuk, C.G. Arges, M. Chatenet, Hot topics in alkaline exchange membrane fuel cells, J. Power Sources 375 (2018) 149–157. https://doi.org/10.1016/j.jpowsour.2017.09.068.
[155] X. Luo, A. Wright, T. Weissbach, S. Holdcroft, Water permeation through anion exchange membranes, J. Power Sources 375 (2018) 442–451. https://doi.org/10.1016/j.jpowsour.2017.05.030.
[156] M. Chatenet, B. G. Pollet, D. R. Dekel, F. Dionigi, J. Deseure, P. Millet, R. D. Braatz, M. Z. Bazant, M. Eikerling, I. Staffell, P. Balcombe, Y. Shao-Horn, H. Schäfer, Water electrolysis: from textbook knowledge to the latest scientific strategies and industrial developments, Chem. Soc. Rev. 51 (2022) 4583–4762. https://doi.org/10.1039/D0CS01079K.
[157] A. Sadezky, H. Muckenhuber, H. Grothe, R. Niessner, U. Pöschl, Raman microspectroscopy of soot and related carbonaceous materials: Spectral analysis and structural information, Carbon 43 (2005) 1731–1742. https://doi.org/10.1016/j.carbon.2005.02.018.

[158] Y. Yang, Z. Lin, S. Gao, J. Su, Z. Lun, G. Xia, J. Chen, R. Zhang, Q. Chen, Tuning Electronic Structures of Nonprecious Ternary Alloys Encapsulated in Graphene Layers for Optimizing Overall Water Splitting Activity, ACS Catal. 7 (2017) 469–479. https://doi.org/10.1021/acscatal.6b02573.
[159] A. Serov, M.H. Robson, M. Smolnik, P. Atanassov, Templated bi-metallic non-PGM catalysts for oxygen reduction, Electrochim. Acta 80 (2012) 213–218. https://doi.org/10.1016/j.electacta.2012.07.008.
[160] X. Zhu, D. Zhang, C.-J. Chen, Q. Zhang, R.-S. Liu, Z. Xia, L. Dai, R. Amal, X. Lu, Harnessing the interplay of Fe–Ni atom pairs embedded in nitrogen-doped carbon for bifunctional oxygen electrocatalysis, Nano Energy 71 (2020) 104597. https://doi.org/10.1016/j.nanoen.2020.104597.
[161] T. Liu, M. Li, X. Bo, M. Zhou, Comparison Study toward the Influence of the Second Metals Doping on the Oxygen Evolution Activity of Cobalt Nitrides, ACS Sustain. Chem. Eng. 6 (2018) 11457–11465. https://doi.org/10.1021/acssuschemeng. 8b01510.
[162] H. Mao, X. Guo, Y. Fu, H. Yang, Y. Zhang, R. Zhang, X.-M. Song, Enhanced electrolytic oxygen evolution by the synergistic effects of trimetallic FeCoNi boride oxides immobilized on polypyrrole/reduced graphene oxide, J. Mater. Chem. A 8 (2020) 1821–1828. https://doi.org/10.1039/C9TA10756H.
[163] X. Zheng, X. Cao, Z. Sun, K. Zeng, J. Yan, P. Strasser, X. Chen, S. Sun, R. Yang, Indiscrete metal/metal-N-C synergic active sites for efficient and durable oxygen electrocatalysis toward advanced Zn-air batteries, Appl. Catal. B 272 (2020) 118967. https://doi.org/10.1016/j.apcatb.2020.118967.
[164] C. Hu, Y. Zhou, R. Ma, Q. Liu, J. Wang, Reactive template synthesis of nitrogen-doped graphene-like carbon nanosheets derived from hydroxypropyl methyl-cellulose and dicyandiamide as efficient oxygen reduction electrocatalysts, J. Power Sources 345 (2017) 120–130. https://doi.org/10.1016/j.jpowsour.2017.01.124.
[165] K. Strickland, E. Miner, Q. Jia, U. Tylus, N. Ramaswamy, W. Liang, M.-T. Sougrati, F. Jaouen, S. Mukerjee, Highly active oxygen reduction non-platinum group metal electrocatalyst without direct metal–nitrogen coordination, Nat. Commun. 6 (2015) 7343. https://doi.org/10.1038/ncomms8343.
[166] W. Chen, Y. Zong, Y. Zhou, W. Lu, Y. Zhang, J. Qian, The nature of MgO precursor decomposition and pore-forming in hard-templating of porous carbon derived from cotton, Coll. Surf. A 571 (2019) 160–167. https://doi.org/10.1016/j.colsurfa.2019.03.091.
[167] G. Yang, H. Han, T. Li, C. Du, Synthesis of nitrogen-doped porous graphitic carbons using nano-CaCO3 as template, graphitization catalyst, and activating agent, Carbon 50 (2012) 3753–3765. https://doi.org/10.1016/j.carbon.2012.03.050.
[168] X.-X. Peng, Y.-Q. Lu, L.-L. Zhou, T. Sheng, S.-Y. Shen, H.-G. Liao, L. Huang, J.-T. Li, S.-G. Sun, Graphitized porous carbon materials with high sulfur loading for lithium-sulfur batteries, Nano Energy 32 (2017) 503–510. https://doi.org/10.1016/j.nanoen.2016.12.060.
[169] S. Ratso, I. Kruusenberg, U. Joost, R. Saar, K. Tammeveski, Enhanced oxygen reduction reaction activity of nitrogen-doped graphene/multi-walled carbon nanotube catalysts in alkaline media, Int. J. Hydrogen Energy 41 (2016) 22510–22519. https://doi.org/10.1016/j.ijhydene.2016.02.021.

[170] Q. Liu, H. Zhang, H. Zhong, S. Zhang, S. Chen, N-doped graphene/carbon composite as non-precious metal electrocatalyst for oxygen reduction reaction, Electrochim. Acta 81 (2012) 313–320. https://doi.org/10.1016/j.electacta.2012.07.022.
[171] M. Xiao, J. Zhu, L. Ma, Z. Jin, J. Ge, X. Deng, Y. Hou, Q. He, J. Li, Q. Jia, S. Mukerjee, R. Yang, Z. Jiang, D. Su, C. Liu, W. Xing, Microporous Framework Induced Synthesis of Single-Atom Dispersed Fe-N-C Acidic ORR Catalyst and Its in Situ Reduced Fe-N4 Active Site Identification Revealed by X-ray Absorption Spectroscopy, ACS Catal. 8 (2018) 2824–2832. https://doi.org/10.1021/acscatal.8b00138.
[172] J. Li, M.T. Sougrati, A. Zitolo, J.M. Ablett, I.C. Oğuz, T. Mineva, I. Matanovic, P. Atanassov, Y. Huang, I. Zenyuk, A. Di Cicco, K. Kumar, L. Dubau, F. Maillard, G. Dražić, F. Jaouen, Identification of durable and non-durable FeNx sites in Fe–N–C materials for proton exchange membrane fuel cells, Nat. Catal. 4 (2021) 10–19. https://doi.org/10.1038/s41929-020-00545-2.
[173] K. Kumar, P. Gairola, M. Lions, N. Ranjbar-Sahraie, M. Mermoux, L. Dubau, A. Zitolo, F. Jaouen, F. Maillard, Physical and Chemical Considerations for Improving Catalytic Activity and Stability of Non-Precious-Metal Oxygen Reduction Reaction Catalysts, ACS Catal. 8 (2018) 11264–11276. https://doi.org/10.1021/acscatal.8b02934.
[174] E.F. Holby, C.D. Taylor, Activity of N-coordinated multi-metal-atom active site structures for Pt-free oxygen reduction reaction catalysis: Role of *OH ligands, Sci. Rep. 5 (2015) 9286. https://doi.org/10.1038/srep09286.
[175] D. Zhang, W. Chen, Z. Li, Y. Chen, L. Zheng, Y. Gong, Q. Li, R. Shen, Y. Han, W.-C. Cheong, L. Gu, Y. Li, Isolated Fe and Co dual active sites on nitrogen-doped carbon for a highly efficient oxygen reduction reaction, Chem. Commun. 54 (2018) 4274–4277. https://doi.org/10.1039/C8CC00988K.
[176] H. Peng, F. Liu, X. Liu, S. Liao, C. You, X. Tian, H. Nan, F. Luo, H. Song, Z. Fu, P. Huang, Effect of Transition Metals on the Structure and Performance of the Doped Carbon Catalysts Derived From Polyaniline and Melamine for ORR Application, ACS Catal. 4 (2014) 3797–3805. https://doi.org/10.1021/cs500744x.
[177] X.X. Wang, V. Prabhakaran, Y. He, Y. Shao, G. Wu, Iron-Free Cathode Catalysts for Proton-Exchange-Membrane Fuel Cells: Cobalt Catalysts and the Peroxide Mitigation Approach, Adv. Mater. 31 (2019) 1805126. https://doi.org/10.1002/adma.201805126.
[178] J.-Y. Choi, L. Yang, T. Kishimoto, X. Fu, S. Ye, Z. Chen, D. Banham, Is the rapid initial performance loss of Fe/N/C non precious metal catalysts due to micropore flooding?, Energy Environ. Sci. 10 (2017) 296–305. https://doi.org/10.1039/C6EE03005J.
[179] R. Chenitz, U.I. Kramm, M. Lefèvre, V. Glibin, G. Zhang, S. Sun, J.-P. Dodelet, A specific demetalation of Fe–N4 catalytic sites in the micropores of NC_Ar + NH3 is at the origin of the initial activity loss of the highly active Fe/N/C catalyst used for the reduction of oxygen in PEM fuel cells, Energy Environ. Sci. 11 (2018) 365–382. https://doi.org/10.1039/C7EE02302B.
[180] R. Zhong, Y. Wu, Z. Liang, W. Guo, C. Zhi, C. Qu, S. Gao, B. Zhu, H. Zhang, R. Zou, Fabricating hierarchically porous and Fe3C-embeded nitrogen-rich carbon nanofibers as exceptional electocatalysts for oxygen reduction, Carbon 142 (2019) 115–122. https://doi.org/10.1016/j.carbon.2018.10.040.
[181] P.M. Ejikeme, K. Makgopa, K.I. Ozoemena, Effects of Catalyst-Support Materials on the Performance of Fuel Cells, in: K.I. Ozoemena, S. Chen (Eds.), Nano-

materials for Fuel Cell Catalysis, Springer International Publishing, Cham, 2016: pp. 517–550. https://doi.org/10.1007/978-3-319-29930-3_13.
[182] E. Antolini, Carbon supports for low-temperature fuel cell catalysts, Appl. Catal. B 88 (2009) 1–24. https://doi.org/10.1016/j.apcatb.2008.09.030.
[183] F. Jaouen, V. Goellner, M. Lefèvre, J. Herranz, E. Proietti, J.P. Dodelet, Oxygen reduction activities compared in rotating-disk electrode and proton exchange membrane fuel cells for highly active FeNC catalysts, Electrochim. Acta 87 (2013) 619–628. https://doi.org/10.1016/j.electacta.2012.09.057.
[184] J.C. Douglin, R.K. Singh, S. Haj-Bsoul, S. Li, J. Biemolt, N. Yan, J.R. Varcoe, G. Rothenberg, D.R. Dekel, A high-temperature anion-exchange membrane fuel cell with a critical raw material-free cathode, Chem. Eng. J. Adv. 8 (2021) 100153. https://doi.org/10.1016/j.ceja.2021.100153.
[185] J.C. Douglin, J.R. Varcoe, D.R. Dekel, A high-temperature anion-exchange membrane fuel cell, J. Power Sources Advances 5 (2020) 100023. https://doi.org/10.1016/j.powera.2020.100023.
[186] H.A. Gasteiger, S.S. Kocha, B. Sompalli, F.T. Wagner, Activity benchmarks and requirements for Pt, Pt-alloy, and non-Pt oxygen reduction catalysts for PEMFCs, Appl. Catal. B 56 (2005) 9–35. https://doi.org/10.1016/j.apcatb.2004.06.021.
[187] A. Orfanidi, P.J. Rheinländer, N. Schulte, H.A. Gasteiger, Ink Solvent Dependence of the Ionomer Distribution in the Catalyst Layer of a PEMFC, J. Electrochem. Soc. 165 (2018) F1254. https://doi.org/10.1149/2.1251814jes.
[188] S. Kabir, K. Artyushkova, A. Serov, P. Atanassov, Role of Nitrogen Moieties in N-Doped 3D-Graphene Nanosheets for Oxygen Electroreduction in Acidic and Alkaline Media, ACS Appl. Mater. Interfaces 10 (2018) 11623–11632. https://doi.org/10.1021/acsami.7b18651.
[189] L. Lai, J.R. Potts, D. Zhan, L. Wang, C.K. Poh, C. Tang, H. Gong, Z. Shen, J. Lin, R.S. Ruoff, Exploration of the active center structure of nitrogen-doped graphene-based catalysts for oxygen reduction reaction, Energy Environ. Sci. 5 (2012) 7936–7942. https://doi.org/10.1039/C2EE21802J.

9. SUMMARY IN ESTONIAN

Resortsinoolist valmistatud süsinikupõhised katalüsaatorid polümeerelektrolüüt-kütuseelementide katoodidele

Doktoritöö eesmärgiks oli valmistada väärismetallivabad katalüsaatorid hapniku elektrokeemilise redutseerumisreaktsiooni jaoks, kasutades lähteainena resortsinoole, ning hinnata nende rakendatavust polümeerelektrolüütmembraaniga kütuseelementides kallihinnaliste väärismetallipõhiste katalüsaatorite asemel. Valmistatud katalüsaatorite iseloomustamiseks kasutati füüsikalis-keemilisi uurimismeetodeid, et saada teadmisi nende aktiivtsentrite ja struktuuri kohta. Materjalide elektrokatalüütilist aktiivsust hinnati pöörleva ketaselektroodi (RDE) meetodil ja katoodkatalüsaatoritena nii anioonivahetusmembraaniga kui ka prootonivahetusmembraaniga kütuseelementides.

Töö esimeses osas keskenduti Fe- ja Co-sisaldavate lämmastikuga dopeeritud süsinikmaterjalidele, mis valmistati 5-metüülresortsinool-formaldehüüd (5MR-FA) vaikudest kahel erineval meetodil [I]. Esmalt saadi süsiniknanosfäärid (CNS) 5MR-FA nanosfääride pürolüüsi teel, mis seejärel dopeeriti pürolüüsides neid lämmastiku ja siirdemetalli allikate juuresolekul. Teine materjalide komplekt valmistati in-situ dopeerimise teel, mille käigus 5MR-FA nanosfäärid pürolüüsiti ühes etapis koos dopantide lähteainetega. Materjalide võrdlus näitas, et in-situ dopeeritud katalüsaatoritel oli suurem hapniku redutseerumise aktiivsus, kuigi nad ei säilitanud oma sfäärilist struktuuri. Kõrgemat elektrokatalüütilist aktiivsust seostati suurema eripinna ja mesopoorse struktuuriga, mis hõlbustab hapniku juurdepääsu aktiivtsentritele.

Töö teises ja kolmandas osas jäeti ära polümerisatsioonireaktsioon ning 5MR kasutati otse süsinikmaterjali valmistamiseks koos ditsüaandiamiidi ning Fe, Co ja/või Ni sooladega [II, III]. Eesmärk oli optimeerida lähteainete suhteid, et saavutada kõrgeim elektrokatalüütiline aktiivsus. Valmistatud FeCoNC-OP-at katalüsaator näitas RDE testides võrdset aktiivsust kommertsiaalse Pt/C katalüsaatoriga ja saavutas anioonivahetusmembraaniga kütuseelemendi (AEMFC) testides katoodkatalüsaatorina 0,8 V juures voolutiheduse 170 mA cm^{-2} ning maksimaalse võimsustiheduse 415 mW cm^{-2}.

Edasistes eksperimentides kasutati süsinikuallikana alküülresortsinoolide segu Honeyol ning kujundati süsiniku nanostruktuuri matriitside ja ionotermilise sünteesimeetodi abil. Neljandas osas kasutati magneesiumil põhinevat matriitsi ning katalüsaatorid dopeeriti lämmastiku ja ainult raua või Fe-Co või Fe-Mn kombinatsiooniga [IV ja V]. Matriitsi abil valmistatud katalüsaatorid näitasid üle kahe korra kõrgemaid maksimaalseid võimsustihedusi nii anioonivahetusmembraaniga kui ka prootonivahetusmembraaniga kütuseelementides (PEMFC) võrreldes ilma matriitsita valmistatud katalüsaatoritega, 920 mW cm^{-2} AEMFC-s ja 514 mW cm^{-2} PEMFC-s. Seda seostati kahe peamise teguriga: kõrgema eripinnaga, mis suurendab aktiivtsentrite hulka, ja hierarhiliselt poorse struktuuriga, mis hõlbustab reagentide transporti katalüsaatorikihis. Doktoritöö viiendas osas kasutati süsinikmaterjalide valmistamiseks ionotermilist meetodit, kus lähte-

aineteks olid $Mg(NO_3)_2$ ja Honeyol [VI]. $Mg(NO_3)_2$ kasutati $Mg–N_x$ tsentrite valmistamiseks, millest seejärel saadi trans-metallatsiooni tulemusena elektrokatalüütiliselt aktiivsed $Fe–N_x$ tsentrid. Samaaegselt käitub $Mg(NO_3)_2$ ka matriitsi allikana, kus pürolüüsi käigus moodustuvad MgO nanoosakesed. Töös optimeeriti lähteainete suhteid ning aktiivseima katalüsaatoriga saavutati leeliselises keskkonnas poollainepotentsiaali väärtuseks 0,87 V, mis on võrreldav kommertsiaalse Pt/C katalüsaatoriga.

Doktoritöö annab väärtuslikke teadmisi tõhusate väärismetallivabade elektrokatalüsaatorite arendamiseks kütuseelementide jaoks, kasutades lihtsaid ja odavaid lähteaineid. Töö tulemused näitavad, et kütuseelemendi kõrge jõudluse saavutamiseks on oluline nii katalüsaatori nanostruktuur kui ka koostis ning saadud tulemused panustavad jätkusuutlike energialahenduste kasutuselevõttu.

10. ACKNOWLEDGEMENTS

First and foremost, I would like to extend my sincere gratitude to my supervisors, Associate Professor Ave Sarapuu and Professor Kaido Tammeveski, for their dedication and contributions. Their guidance significantly shaped the work presented in my thesis and more importantly had a notable impact in shaping me as a scientist.

I would like to thank all of my co-workers and lab mates throughout the years, both at the University of Tartu and Technion, for their assistance and interesting discussions, scientific or not.

Additionally, I thank all of my co-authors who all contributed to my work over the years: Helle-Mai Piirsoo, Jaan Aruväli, Dr. Arvo Kikas, Dr. Vambola Kisand, Dr. Srinu Akula, Dr. Maido Merisalu, Dr. Päärn Paiste, Dr. Helina Seemen, Dr. Maike Käärik, Mati Kook, Dr. Anna-Liisa Peikolainen, Dr. Aleksei Treštšalov, Dmytro Danilian, Dr. Jekaterina Kozlova, Dr. Jaan Leis, Dr. Mihkel Rähn, Dr. Aile Tamm, Dr. Prof. Kaupo Kukli, Prof. Väino Sammelselg, Prof. Steven Holdcroft, Dr. Ghenwa El Chawich, Dr. Frédéric Jaouen, Dr. Sara Cavaliere, John C. Douglin and Prof. Dario R. Dekel.

A huge acknowledgement to my parents Kai and Kalle who first inspired me towards science.

The work in this thesis was financially supported by the Estonian Research Council (grant PRG723) and the M-ERA.Net project "C-MOF.cell" (SLTKT 20445) and by institutional research funding (IUT20-16) of the Estonian Ministry of Education and Research. This research was also supported by the EU through the European Regional Development Fund (TK141, "Advanced materials and high-technology devices for energy recuperation systems"), the Estonian Ministry of Education and Research (TK210, Centre of Excellence in Sustainable Green Hydrogen and Energy Technologies). I would like to extend my gratitude to the graduate school „Functional materials and technologies" and to Haridus- ja Noorteamet for providing the Kristjan Jaak scholarship. Finally, I would like to thank Viru Keemia Grupp for generously providing the 5MR and Honeyol.

11. PUBLICATIONS

CURRICULUM VITAE

Name: Kaarel Kisand
Date of birth: December 5, 1994
Citizenship: Estonian
Address: Ravila 14a, 50411 Tartu, Estonia
E-mail: kaarel.kisand@ut.ee

Education:

2020–…	University of Tartu, PhD (Chemistry)
2018–2020	University of Tartu, MSc (Chemistry)
2014–2017	University of Tartu, BSc (Chemistry)

Professional experience:

10.05.2021–31.05.2024	University of Tartu, Institute of Chemistry, chemist
18.09.2023–15.12.2023	Technion – Israel Institute of Technology, Wolfson Department of Chemical Engineering, visiting PhD student
02.05.2024–…	Elcogen AS, research and development engineer

Major scientific publications:

1. Sarapuu, A.; Kreek, K.; Kisand, K.; Kook, M.; Uibu, M.; Koel, M.; Tammeveski, K. Electrocatalysis of oxygen reduction by iron-containing nitrogen-doped carbon aerogels in alkaline solution. Electrochimica Acta 230, 81–88 (2017).
2. Kisand, K.; Sarapuu, A.; Peikolainen, A.-L.; Seemen, H.; Kook, M.; Käärik, M.; Leis, J.; Sammelselg, V.; Tammeveski, K. Oxygen Reduction on Fe- and Co-Containing Nitrogen-Doped Nanocarbons. ChemElectroChem 5, 2002–2009 (2018).
3. Kisand, K.; Sarapuu, A.; Danilian, D.; Kikas, A.; Kisand, V.; Rähn, M.; Treshchalov, A.; Käärik, M.; Merisalu, M.; Paiste, P.; Aruväli, J.; Leis, J.; Sammelselg, V.; Holdcroft, S.; Tammeveski, K. Transition metal-containing nitrogen-doped nanocarbon catalysts derived from 5-methylresorcinol for anion exchange membrane fuel cell application. Journal of Colloid and Interface Science 584, 263–274 (2021).
4. Kisand, K.; Sarapuu, A.; Kikas, A.; Kisand, V.; Rähn, M.; Treshchalov, A.; Käärik, M.; Piirsoo, H.-M.; Aruväli, J.; Paiste, P.; Leis, J.; Sammelselg, V.; Tamm, A.; Tammeveski, K. Bifunctional multi-metallic nitrogen-doped nanocarbon catalysts derived from 5-methylresorcinol. Electrochemistry Communications 124, 106932 (2021).
5. Kisand, K.; Sarapuu, A.; Douglin, J. C.; Kikas, A.; Treshchalov, A.; Käärik, M.; Piirsoo, H.-M.; Paiste, P.; Aruväli, J.; Leis, J.; Kisand, V.; Tamm, A.; Dekel, D. R.; Tammeveski, K. Templated Nitrogen-, Iron-, and Cobalt-Doped Mesoporous Nanocarbon Derived from an Alkylresorcinol Mixture for Anion-Exchange Membrane Fuel Cell Application. ACS Catalysis 12, 14050–14061 (2022).

ELULOOKIRJELDUS

Nimi: Kaarel Kisand
Sünniaeg: 5. detsember 1994
Kodakondsus: Eesti
Aadress: Ravila 14a, 50411 Tartu, Eesti
E-mail: kaarel.kisand@ut.ee

Hariduskäik:

2020–…	Tartu Ülikool, doktorant (keemia)
2018–2020	Tartu Ülikool, MSc (keemia)
2014–2017	Tartu Ülikool, BSc (keemia)

Töökogemus:

10.05.2020–31.05.2024	Tartu Ülikool, Keemia instituut, keemik
18.09.2023–15.12.2023	Technion – Iisraeli Tehnoloogiainstituut, Wolfsoni Keemiatehnika Õppetool, külalisdoktorant
02.05.2024–…	Elcogen AS, teadus- ja arendusinsener

Publikatsioonide loetelu:

1. Sarapuu, A.; Kreek, K.; Kisand, K.; Kook, M.; Uibu, M.; Koel, M.; Tammeveski, K. Electrocatalysis of oxygen reduction by iron-containing nitrogen-doped carbon aerogels in alkaline solution. Electrochimica Acta 230, 81–88 (2017).
2. Kisand, K.; Sarapuu, A.; Peikolainen, A.-L.; Seemen, H.; Kook, M.; Käärik, M.; Leis, J.; Sammelselg, V.; Tammeveski, K. Oxygen Reduction on Fe- and Co-Containing Nitrogen-Doped Nanocarbons. ChemElectroChem 5, 2002–2009 (2018).
3. Kisand, K.; Sarapuu, A.; Danilian, D.; Kikas, A.; Kisand, V.; Rähn, M.; Treshchalov, A.; Käärik, M.; Merisalu, M.; Paiste, P.; Aruväli, J.; Leis, J.; Sammelselg, V.; Holdcroft, S.; Tammeveski, K. Transition metal-containing nitrogen-doped nanocarbon catalysts derived from 5-methylresorcinol for anion exchange membrane fuel cell application. Journal of Colloid and Interface Science 584, 263–274 (2021).
4. Kisand, K.; Sarapuu, A.; Kikas, A.; Kisand, V.; Rähn, M.; Treshchalov, A.; Käärik, M.; Piirsoo, H.-M.; Aruväli, J.; Paiste, P.; Leis, J.; Sammelselg, V.; Tamm, A.; Tammeveski, K. Bifunctional multi-metallic nitrogen-doped nanocarbon catalysts derived from 5-methylresorcinol. Electrochemistry Communications 124, 106932 (2021).
5. Kisand, K.; Sarapuu, A.; Douglin, J. C.; Kikas, A.; Treshchalov, A.; Käärik, M.; Piirsoo, H.-M.; Paiste, P.; Aruväli, J.; Leis, J.; Kisand, V.; Tamm, A.; Dekel, D. R.; Tammeveski, K. Templated Nitrogen-, Iron-, and Cobalt-Doped Mesoporous Nanocarbon Derived from an Alkylresorcinol Mixture for Anion-Exchange Membrane Fuel Cell Application. ACS Catalysis 12, 14050–14061 (2022).

DISSERTATIONES CHIMICAE UNIVERSITATIS TARTUENSIS

1. **Toomas Tamm.** Quantum-chemical simulation of solvent effects. Tartu, 1993, 110 p.
2. **Peeter Burk.** Theoretical study of gas-phase acid-base equilibria. Tartu, 1994, 96 p.
3. **Victor Lobanov.** Quantitative structure-property relationships in large descriptor spaces. Tartu, 1995, 135 p.
4. **Vahur Mäemets.** The ^{17}O and ^{1}H nuclear magnetic resonance study of H_2O in individual solvents and its charged clusters in aqueous solutions of electrolytes. Tartu, 1997, 140 p.
5. **Andrus Metsala.** Microcanonical rate constant in nonequilibrium distribution of vibrational energy and in restricted intramolecular vibrational energy redistribution on the basis of slater's theory of unimolecular reactions. Tartu, 1997, 150 p.
6. **Uko Maran.** Quantum-mechanical study of potential energy surfaces in different environments. Tartu, 1997, 137 p.
7. **Alar Jänes.** Adsorption of organic compounds on antimony, bismuth and cadmium electrodes. Tartu, 1998, 219 p.
8. **Kaido Tammeveski.** Oxygen electroreduction on thin platinum films and the electrochemical detection of superoxide anion. Tartu, 1998, 139 p.
9. **Ivo Leito.** Studies of Brønsted acid-base equilibria in water and non-aqueous media. Tartu, 1998, 101 p.
10. **Jaan Leis.** Conformational dynamics and equilibria in amides. Tartu, 1998, 131 p.
11. **Toonika Rinken.** The modelling of amperometric biosensors based on oxidoreductases. Tartu, 2000, 108 p.
12. **Dmitri Panov.** Partially solvated Grignard reagents. Tartu, 2000, 64 p.
13. **Kaja Orupõld.** Treatment and analysis of phenolic wastewater with microorganisms. Tartu, 2000, 123 p.
14. **Jüri Ivask.** Ion Chromatographic determination of major anions and cations in polar ice core. Tartu, 2000, 85 p.
15. **Lauri Vares.** Stereoselective Synthesis of Tetrahydrofuran and Tetrahydropyran Derivatives by Use of Asymmetric Horner-Wadsworth-Emmons and Ring Closure Reactions. Tartu, 2000, 184 p.
16. **Martin Lepiku.** Kinetic aspects of dopamine D_2 receptor interactions with specific ligands. Tartu, 2000, 81 p.
17. **Katrin Sak.** Some aspects of ligand specificity of P2Y receptors. Tartu, 2000, 106 p.
18. **Vello Pällin.** The role of solvation in the formation of iotsitch complexes. Tartu, 2001, 95 p.
19. **Katrin Kollist.** Interactions between polycyclic aromatic compounds and humic substances. Tartu, 2001, 93 p.

20. **Ivar Koppel.** Quantum chemical study of acidity of strong and superstrong Brønsted acids. Tartu, 2001, 104 p.
21. **Viljar Pihl.** The study of the substituent and solvent effects on the acidity of OH and CH acids. Tartu, 2001, 132 p.
22. **Natalia Palm.** Specification of the minimum, sufficient and significant set of descriptors for general description of solvent effects. Tartu, 2001, 134 p.
23. **Sulev Sild.** QSPR/QSAR approaches for complex molecular systems. Tartu, 2001, 134 p.
24. **Ruslan Petrukhin.** Industrial applications of the quantitative structure-property relationships. Tartu, 2001, 162 p.
25. **Boris V. Rogovoy.** Synthesis of (benzotriazolyl)carboximidamides and their application in relations with *N*- and *S*-nucleophyles. Tartu, 2002, 84 p.
26. **Koit Herodes.** Solvent effects on UV-vis absorption spectra of some solvatochromic substances in binary solvent mixtures: the preferential solvation model. Tartu, 2002, 102 p.
27. **Anti Perkson.** Synthesis and characterisation of nanostructured carbon. Tartu, 2002, 152 p.
28. **Ivari Kaljurand.** Self-consistent acidity scales of neutral and cationic Brønsted acids in acetonitrile and tetrahydrofuran. Tartu, 2003, 108 p.
29. **Karmen Lust.** Adsorption of anions on bismuth single crystal electrodes. Tartu, 2003, 128 p.
30. **Mare Piirsalu.** Substituent, temperature and solvent effects on the alkaline hydrolysis of substituted phenyl and alkyl esters of benzoic acid. Tartu, 2003, 156 p.
31. **Meeri Sassian.** Reactions of partially solvated Grignard reagents. Tartu, 2003, 78 p.
32. **Tarmo Tamm.** Quantum chemical modelling of polypyrrole. Tartu, 2003. 100 p.
33. **Erik Teinemaa.** The environmental fate of the particulate matter and organic pollutants from an oil shale power plant. Tartu, 2003. 102 p.
34. **Jaana Tammiku-Taul.** Quantum chemical study of the properties of Grignard reagents. Tartu, 2003. 120 p.
35. **Andre Lomaka.** Biomedical applications of predictive computational chemistry. Tartu, 2003. 132 p.
36. **Kostyantyn Kirichenko.** Benzotriazole – Mediated Carbon–Carbon Bond Formation. Tartu, 2003. 132 p.
37. **Gunnar Nurk.** Adsorption kinetics of some organic compounds on bismuth single crystal electrodes. Tartu, 2003, 170 p.
38. **Mati Arulepp.** Electrochemical characteristics of porous carbon materials and electrical double layer capacitors. Tartu, 2003, 196 p.
39. **Dan Cornel Fara.** QSPR modeling of complexation and distribution of organic compounds. Tartu, 2004, 126 p.
40. **Riina Mahlapuu.** Signalling of galanin and amyloid precursor protein through adenylate cyclase. Tartu, 2004, 124 p.

41. **Mihkel Kerikmäe.** Some luminescent materials for dosimetric applications and physical research. Tartu, 2004, 143 p.
42. **Jaanus Kruusma.** Determination of some important trace metal ions in human blood. Tartu, 2004, 115 p.
43. **Urmas Johanson.** Investigations of the electrochemical properties of polypyrrole modified electrodes. Tartu, 2004, 91 p.
44. **Kaido Sillar.** Computational study of the acid sites in zeolite ZSM-5. Tartu, 2004, 80 p.
45. **Aldo Oras.** Kinetic aspects of dATPαS interaction with $P2Y_1$ receptor. Tartu, 2004, 75 p.
46. **Erik Mölder.** Measurement of the oxygen mass transfer through the air-water interface. Tartu, 2005, 73 p.
47. **Thomas Thomberg.** The kinetics of electroreduction of peroxodisulfate anion on cadmium (0001) single crystal electrode. Tartu, 2005, 95 p.
48. **Olavi Loog.** Aspects of condensations of carbonyl compounds and their imine analogues. Tartu, 2005, 83 p.
49. **Siim Salmar.** Effect of ultrasound on ester hydrolysis in aqueous ethanol. Tartu, 2006, 73 p.
50. **Ain Uustare.** Modulation of signal transduction of heptahelical receptors by other receptors and G proteins. Tartu, 2006, 121 p.
51. **Sergei Yurchenko.** Determination of some carcinogenic contaminants in food. Tartu, 2006, 143 p.
52. **Kaido Tämm.** QSPR modeling of some properties of organic compounds. Tartu, 2006, 67 p.
53. **Olga Tšubrik.** New methods in the synthesis of multisubstituted hydrazines. Tartu. 2006, 183 p.
54. **Lilli Sooväli.** Spectrophotometric measurements and their uncertainty in chemical analysis and dissociation constant measurements. Tartu, 2006, 125 p.
55. **Eve Koort.** Uncertainty estimation of potentiometrically measured ph and pK_a values. Tartu, 2006, 139 p.
56. **Sergei Kopanchuk.** Regulation of ligand binding to melanocortin receptor subtypes. Tartu, 2006, 119 p.
57. **Silvar Kallip.** Surface structure of some bismuth and antimony single crystal electrodes. Tartu, 2006, 107 p.
58. **Kristjan Saal.** Surface silanization and its application in biomolecule coupling. Tartu, 2006, 77 p.
59. **Tanel Tätte.** High viscosity $Sn(OBu)_4$ oligomeric concentrates and their applications in technology. Tartu, 2006, 91 p.
60. **Dimitar Atanasov Dobchev**. Robust QSAR methods for the prediction of properties from molecular structure. Tartu, 2006, 118 p.
61. **Hannes Hagu**. Impact of ultrasound on hydrophobic interactions in solutions. Tartu, 2007, 81 p.
62. **Rutha Jäger.** Electroreduction of peroxodisulfate anion on bismuth electrodes. Tartu, 2007, 142 p.

63. **Kaido Viht.** Immobilizable bisubstrate-analogue inhibitors of basophilic protein kinases: development and application in biosensors. Tartu, 2007, 88 p.
64. **Eva-Ingrid Rõõm.** Acid-base equilibria in nonpolar media. Tartu, 2007, 156 p.
65. **Sven Tamp.** DFT study of the cesium cation containing complexes relevant to the cesium cation binding by the humic acids. Tartu, 2007, 102 p.
66. **Jaak Nerut.** Electroreduction of hexacyanoferrate(III) anion on Cadmium (0001) single crystal electrode. Tartu, 2007, 180 p.
67. **Lauri Jalukse.** Measurement uncertainty estimation in amperometric dissolved oxygen concentration measurement. Tartu, 2007, 112 p.
68. **Aime Lust.** Charge state of dopants and ordered clusters formation in CaF_2:Mn and CaF_2:Eu luminophors. Tartu, 2007, 100 p.
69. **Iiris Kahn**. Quantitative Structure-Activity Relationships of environmentally relevant properties. Tartu, 2007, 98 p.
70. **Mari Reinik.** Nitrates, nitrites, N-nitrosamines and polycyclic aromatic hydrocarbons in food: analytical methods, occurrence and dietary intake. Tartu, 2007, 172 p.
71. **Heili Kasuk.** Thermodynamic parameters and adsorption kinetics of organic compounds forming the compact adsorption layer at Bi single crystal electrodes. Tartu, 2007, 212 p.
72. **Erki Enkvist.** Synthesis of adenosine-peptide conjugates for biological applications. Tartu, 2007, 114 p.
73. **Svetoslav Hristov Slavov**. Biomedical applications of the QSAR approach. Tartu, 2007, 146 p.
74. **Eneli Härk.** Electroreduction of complex cations on electrochemically polished Bi(*hkl*) single crystal electrodes. Tartu, 2008, 158 p.
75. **Priit Möller.** Electrochemical characteristics of some cathodes for medium temperature solid oxide fuel cells, synthesized by solid state reaction technique. Tartu, 2008, 90 p.
76. **Signe Viggor.** Impact of biochemical parameters of genetically different pseudomonads at the degradation of phenolic compounds. Tartu, 2008, 122 p.
77. **Ave Sarapuu.** Electrochemical reduction of oxygen on quinone-modified carbon electrodes and on thin films of platinum and gold. Tartu, 2008, 134 p.
78. **Agnes Kütt.** Studies of acid-base equilibria in non-aqueous media. Tartu, 2008, 198 p.
79. **Rouvim Kadis.** Evaluation of measurement uncertainty in analytical chemistry: related concepts and some points of misinterpretation. Tartu, 2008, 118 p.
80. **Valter Reedo.** Elaboration of IVB group metal oxide structures and their possible applications. Tartu, 2008, 98 p.
81. **Aleksei Kuznetsov.** Allosteric effects in reactions catalyzed by the cAMP-dependent protein kinase catalytic subunit. Tartu, 2009, 133 p.

82. **Aleksei Bredihhin.** Use of mono- and polyanions in the synthesis of multisubstituted hydrazine derivatives. Tartu, 2009, 105 p.
83. **Anu Ploom.** Quantitative structure-reactivity analysis in organosilicon chemistry. Tartu, 2009, 99 p.
84. **Argo Vonk.** Determination of adenosine A_{2A}- and dopamine D_1 receptor-specific modulation of adenylate cyclase activity in rat striatum. Tartu, 2009, 129 p.
85. **Indrek Kivi.** Synthesis and electrochemical characterization of porous cathode materials for intermediate temperature solid oxide fuel cells. Tartu, 2009, 177 p.
86. **Jaanus Eskusson.** Synthesis and characterisation of diamond-like carbon thin films prepared by pulsed laser deposition method. Tartu, 2009, 117 p.
87. **Marko Lätt.** Carbide derived microporous carbon and electrical double layer capacitors. Tartu, 2009, 107 p.
88. **Vladimir Stepanov.** Slow conformational changes in dopamine transporter interaction with its ligands. Tartu, 2009, 103 p.
89. **Aleksander Trummal.** Computational Study of Structural and Solvent Effects on Acidities of Some Brønsted Acids. Tartu, 2009, 103 p.
90. **Eerold Vellemäe.** Applications of mischmetal in organic synthesis. Tartu, 2009, 93 p.
91. **Sven Parkel.** Ligand binding to 5-HT_{1A} receptors and its regulation by Mg^{2+} and Mn^{2+}. Tartu, 2010, 99 p.
92. **Signe Vahur.** Expanding the possibilities of ATR-FT-IR spectroscopy in determination of inorganic pigments. Tartu, 2010, 184 p.
93. **Tavo Romann**. Preparation and surface modification of bismuth thin film, porous, and microelectrodes. Tartu, 2010, 155 p.
94. **Nadežda Aleksejeva.** Electrocatalytic reduction of oxygen on carbon nanotube-based nanocomposite materials. Tartu, 2010, 147 p.
95. **Marko Kullapere.** Electrochemical properties of glassy carbon, nickel and gold electrodes modified with aryl groups. Tartu, 2010, 233 p.
96. **Liis Siinor.** Adsorption kinetics of ions at Bi single crystal planes from aqueous electrolyte solutions and room-temperature ionic liquids. Tartu, 2010, 101 p.
97. **Angela Vaasa.** Development of fluorescence-based kinetic and binding assays for characterization of protein kinases and their inhibitors. Tartu 2010, 101 p.
98. **Indrek Tulp.** Multivariate analysis of chemical and biological properties. Tartu 2010, 105 p.
99. **Aare Selberg.** Evaluation of environmental quality in Northern Estonia by the analysis of leachate. Tartu 2010, 117 p.
100. **Darja Lavõgina.** Development of protein kinase inhibitors based on adenosine analogue-oligoarginine conjugates. Tartu 2010, 248 p.
101. **Laura Herm.** Biochemistry of dopamine D_2 receptors and its association with motivated behaviour. Tartu 2010, 156 p.

102. **Terje Raudsepp.** Influence of dopant anions on the electrochemical properties of polypyrrole films. Tartu 2010, 112 p.
103. **Margus Marandi.** Electroformation of Polypyrrole Films: *In-situ* AFM and STM Study. Tartu 2011, 116 p.
104. **Kairi Kivirand.** Diamine oxidase-based biosensors: construction and working principles. Tartu, 2011, 140 p.
105. **Anneli Kruve.** Matrix effects in liquid-chromatography electrospray mass-spectrometry. Tartu, 2011, 156 p.
106. **Gary Urb.** Assessment of environmental impact of oil shale fly ash from PF and CFB combustion. Tartu, 2011, 108 p.
107. **Nikita Oskolkov.** A novel strategy for peptide-mediated cellular delivery and induction of endosomal escape. Tartu, 2011, 106 p.
108. **Dana Martin.** The QSPR/QSAR approach for the prediction of properties of fullerene derivatives. Tartu, 2011, 98 p.
109. **Säde Viirlaid.** Novel glutathione analogues and their antioxidant activity. Tartu, 2011, 106 p.
110. **Ülis Sõukand.** Simultaneous adsorption of Cd^{2+}, Ni^{2+}, and Pb^{2+} on peat. Tartu, 2011, 124 p.
111. **Lauri Lipping.** The acidity of strong and superstrong Brønsted acids, an outreach for the "limits of growth": a quantum chemical study. Tartu, 2011, 124 p.
112. **Heisi Kurig.** Electrical double-layer capacitors based on ionic liquids as electrolytes. Tartu, 2011, 146 p.
113. **Marje Kasari.** Bisubstrate luminescent probes, optical sensors and affinity adsorbents for measurement of active protein kinases in biological samples. Tartu, 2012, 126 p.
114. **Kalev Takkis.** Virtual screening of chemical databases for bioactive molecules. Tartu, 2012, 122 p.
115. **Ksenija Kisseljova**. Synthesis of aza-β^3-amino acid containing peptides and kinetic study of their phosphorylation by protein kinase A. Tartu, 2012, 104 p.
116. **Riin Rebane.** Advanced method development strategy for derivatization LC/ESI/MS. Tartu, 2012, 184 p.
117. **Vladislav Ivaništšev.** Double layer structure and adsorption kinetics of ions at metal electrodes in room temperature ionic liquids. Tartu, 2012, 128 p.
118. **Irja Helm.** High accuracy gravimetric Winkler method for determination of dissolved oxygen. Tartu, 2012, 139 p.
119. **Karin Kipper.** Fluoroalcohols as Components of LC-ESI-MS Eluents: Usage and Applications. Tartu, 2012, 164 p.
120. **Arno Ratas.** Energy storage and transfer in dosimetric luminescent materials. Tartu, 2012, 163 p.
121. **Reet Reinart-Okugbeni**. Assay systems for characterisation of subtype-selective binding and functional activity of ligands on dopamine receptors. Tartu, 2012, 159 p.

122. **Lauri Sikk.** Computational study of the Sonogashira cross-coupling reaction. Tartu, 2012, 81 p.
123. **Karita Raudkivi.** Neurochemical studies on inter-individual differences in affect-related behaviour of the laboratory rat. Tartu, 2012, 161 p.
124. **Indrek Saar.** Design of GalR2 subtype specific ligands: their role in depression-like behavior and feeding regulation. Tartu, 2013, 126 p.
125. **Ann Laheäär.** Electrochemical characterization of alkali metal salt based non-aqueous electrolytes for supercapacitors. Tartu, 2013, 127 p.
126. **Kerli Tõnurist.** Influence of electrospun separator materials properties on electrochemical performance of electrical double-layer capacitors. Tartu, 2013, 147 p.
127. **Kaija Põhako-Esko.** Novel organic and inorganic ionogels: preparation and characterization. Tartu, 2013, 124 p.
128. **Ivar Kruusenberg.** Electroreduction of oxygen on carbon nanomaterial-based catalysts. Tartu, 2013, 191 p.
129. **Sander Piiskop.** Kinetic effects of ultrasound in aqueous acetonitrile solutions. Tartu, 2013, 95 p.
130. **Ilona Faustova**. Regulatory role of L-type pyruvate kinase N-terminal domain. Tartu, 2013, 109 p.
131. **Kadi Tamm.** Synthesis and characterization of the micro-mesoporous anode materials and testing of the medium temperature solid oxide fuel cell single cells. Tartu, 2013, 138 p.
132. **Iva Bozhidarova Stoyanova-Slavova.** Validation of QSAR/QSPR for regulatory purposes. Tartu, 2013, 109 p.
133. **Vitali Grozovski**. Adsorption of organic molecules at single crystal electrodes studied by *in situ* STM method. Tartu, 2014, 146 p.
134. **Santa Veikšina**. Development of assay systems for characterisation of ligand binding properties to melanocortin 4 receptors. Tartu, 2014, 151 p.
135. **Jüri Liiv.** PVDF (polyvinylidene difluoride) as material for active element of twisting-ball displays. Tartu, 2014, 111 p.
136. **Kersti Vaarmets.** Electrochemical and physical characterization of pristine and activated molybdenum carbide-derived carbon electrodes for the oxygen electroreduction reaction. Tartu, 2014, 131 p.
137. **Lauri Tõntson**. Regulation of G-protein subtypes by receptors, guanine nucleotides and Mn^{2+}. Tartu, 2014, 105 p.
138. **Aiko Adamson.** Properties of amine-boranes and phosphorus analogues in the gas phase. Tartu, 2014, 78 p.
139. **Elo Kibena**. Electrochemical grafting of glassy carbon, gold, highly oriented pyrolytic graphite and chemical vapour deposition-grown graphene electrodes by diazonium reduction method. Tartu, 2014, 184 p.
140. **Teemu Näykki.** Novel Tools for Water Quality Monitoring – From Field to Laboratory. Tartu, 2014, 202 p.
141. **Karl Kaupmees.** Acidity and basicity in non-aqueous media: importance of solvent properties and purity. Tartu, 2014, 128 p.

142. **Oleg Lebedev**. Hydrazine polyanions: different strategies in the synthesis of heterocycles. Tartu, 2015, 118 p.
143. **Geven Piir.** Environmental risk assessment of chemicals using QSAR methods. Tartu, 2015, 123 p.
144. **Olga Mazina.** Development and application of the biosensor assay for measurements of cyclic adenosine monophosphate in studies of G protein-coupled receptor signalinga. Tartu, 2015, 116 p.
145. **Sandip Ashokrao Kadam.** Anion receptors: synthesis and accurate binding measurements. Tartu, 2015, 116 p.
146. **Indrek Tallo.** Synthesis and characterization of new micro-mesoporous carbide derived carbon materials for high energy and power density electrical double layer capacitors. Tartu, 2015, 148 p.
147. **Heiki Erikson.** Electrochemical reduction of oxygen on nanostructured palladium and gold catalysts. Tartu, 2015, 204 p.
148. **Erik Anderson.** *In situ* Scanning Tunnelling Microscopy studies of the interfacial structure between Bi(111) electrode and a room temperature ionic liquid. Tartu, 2015, 118 p.
149. **Girinath G. Pillai.** Computational Modelling of Diverse Chemical, Biochemical and Biomedical Properties. Tartu, 2015, 140 p.
150. **Piret Pikma.** Interfacial structure and adsorption of organic compounds at Cd(0001) and Sb(111) electrodes from ionic liquid and aqueous electrolytes: an *in situ* STM study. Tartu, 2015, 126 p.
151. **Ganesh babu Manoharan.** Combining chemical and genetic approaches for photoluminescence assays of protein kinases. Tartu, 2016, 126 p.
152. **Carolin Siimenson**. Electrochemical characterization of halide ion adsorption from liquid mixtures at Bi(111) and pyrolytic graphite electrode surface. Tartu, 2016, 110 p.
153. **Asko Laaniste.** Comparison and optimisation of novel mass spectrometry ionisation sources. Tartu, 2016, 156 p.
154. **Hanno Evard.** Estimating limit of detection for mass spectrometric analysis methods. Tartu, 2016, 224 p.
155. **Kadri Ligi.** Characterization and application of protein kinase-responsive organic probes with triplet-singlet energy transfer. Tartu, 2016, 122 p.
156. **Margarita Kagan.** Biosensing penicillins' residues in milk flows. Tartu, 2016, 130 p.
157. **Marie Kriisa.** Development of protein kinase-responsive photoluminescent probes and cellular regulators of protein phosphorylation. Tartu, 2016, 106 p.
158. **Mihkel Vestli.** Ultrasonic spray pyrolysis deposited electrolyte layers for intermediate temperature solid oxide fuel cells. Tartu, 2016, 156 p.
159. **Silver Sepp**. Influence of porosity of the carbide-derived carbon on the properties of the composite electrocatalysts and characteristics of polymer electrolyte fuel cells. Tartu, 2016, 137 p.
160. **Kristjan Haav**. Quantitative relative equilibrium constant measurements in supramolecular chemistry. Tartu, 2017, 158 p.

161. **Anu Teearu**. Development of MALDI-FT-ICR-MS methodology for the analysis of resinous materials. Tartu, 2017, 205 p.
162. **Taavi Ivan**. Bifunctional inhibitors and photoluminescent probes for studies on protein complexes. Tartu, 2017, 140 p.
163. **Maarja-Liisa Oldekop**. Characterization of amino acid derivatization reagents for LC-MS analysis. Tartu, 2017, 147 p.
164. **Kristel Jukk**. Electrochemical reduction of oxygen on platinum- and palladium-based nanocatalysts. Tartu, 2017, 250 p.
165. **Siim Kukk**. Kinetic aspects of interaction between dopamine transporter and *N*-substituted nortropane derivatives. Tartu, 2017, 107 p.
166. **Birgit Viira**. Design and modelling in early drug development in targeting HIV-1 reverse transcriptase and Malaria. Tartu, 2017, 172 p.
167. **Rait Kivi**. Allostery in cAMP dependent protein kinase catalytic subunit. Tartu, 2017, 115 p.
168. **Agnes Heering**. Experimental realization and applications of the unified acidity scale. Tartu, 2017, 123 p.
169. **Delia Juronen**. Biosensing system for the rapid multiplex detection of mastitis-causing pathogens in milk. Tartu, 2018, 85 p.
170. **Hedi Rahnel.** ARC-inhibitors: from reliable biochemical assays to regulators of physiology of cells. Tartu, 2018, 176 p.
171. **Anton Ruzanov.** Computational investigation of the electrical double layer at metal–aqueous solution and metal–ionic liquid interfaces. Tartu, 2018, 129 p.
172. **Katrin Kestav.** Crystal Structure-Guided Development of Bisubstrate-Analogue Inhibitors of Mitotic Protein Kinase Haspin. Tartu, 2018, 166 p.
173. **Mihkel Ilisson.** Synthesis of novel heterocyclic hydrazine derivatives and their conjugates. Tartu, 2018, 101 p.
174. **Anni Allikalt.** Development of assay systems for studying ligand binding to dopamine receptors. Tartu, 2018, 160 p.
175. **Ove Oll.** Electrical double layer structure and energy storage characteristics of ionic liquid based capacitors. Tartu, 2018, 187 p.
176. **Rasmus Palm.** Carbon materials for energy storage applications. Tartu, 2018, 114 p.
177. **Jörgen Metsik.** Preparation and stability of poly(3,4-ethylenedioxythiophene) thin films for transparent electrode applications. Tartu, 2018, 111 p.
178. **Sofja Tšepelevitš.** Experimental studies and modeling of solute-solvent interactions. Tartu, 2018, 109 p.
179. **Märt Lõkov.** Basicity of some nitrogen, phosphorus and carbon bases in acetonitrile. Tartu, 2018, 104 p.
180. **Anton Mastitski**. Preparation of α-aza-amino acid precursors and related compounds by novel methods of reductive one-pot alkylation and direct alkylation. Tartu, 2018, 155 p.
181. **Jürgen Vahter**. Development of bisubstrate inhibitors for protein kinase CK2. Tartu, 2019, 186 p.

182. **Piia Liigand.** Expanding and improving methodology and applications of ionization efficiency measurements. Tartu, 2019, 189 p.
183. **Sigrid Selberg.** Synthesis and properties of lipophilic phosphazene-based indicator molecules. Tartu, 2019, 74 p.
184. **Jaanus Liigand.** Standard substance free quantification for LC/ESI/MS analysis based on the predicted ionization efficiencies. Tartu, 2019, 254 p.
185. **Marek Mooste.** Surface and electrochemical characterisation of aryl film and nanocomposite material modified carbon and metal-based electrodes. Tartu, 2019, 304 p.
186. **Mare Oja.** Experimental investigation and modelling of pH profiles for effective membrane permeability of drug substances. Tartu, 2019, 306 p.
187. **Sajid Hussain.** Electrochemical reduction of oxygen on supported Pt catalysts. Tartu, 2019, 220 p.
188. **Ronald Väli.** Glucose-derived hard carbon electrode materials for sodium-ion batteries. Tartu, 2019, 180 p.
189. **Ester Tee.** Analysis and development of selective synthesis methods of hierarchical micro- and mesoporous carbons. Tartu, 2019, 210 p.
190. **Martin Maide.** Influence of the microstructure and chemical composition of the fuel electrode on the electrochemical performance of reversible solid oxide fuel cell. Tartu, 2020, 144 p.
191. **Edith Viirlaid.** Biosensing Pesticides in Water Samples. Tartu, 2020, 102 p.
192. **Maike Käärik.** Nanoporous carbon: the controlled nanostructure, and structure-property relationships. Tartu, 2020, 162 p.
193. **Artur Gornischeff.** Study of ionization efficiencies for derivatized compounds in LC/ESI/MS and their application for targeted analysis. Tartu, 2020, 124 p.
194. **Reet Link.** Ligand binding, allosteric modulation and constitutive activity of melanocortin-4 receptors. Tartu, 2020, 108 p.
195. **Pilleriin Peets.** Development of instrumental methods for the analysis of textile fibres and dyes. Tartu, 2020, 150 p.
196. **Larisa Ivanova.** Design of active compounds against neurodegenerative diseases. Tartu, 2020, 152 p.
197. **Meelis Härmas.** Impact of activated carbon microstructure and porosity on electrochemical performance of electrical double-layer capacitors. Tartu, 2020, 122 p.
198. **Ruta Hecht.** Novel Eluent Additives for LC-MS Based Bioanalytical Methods. Tartu, 2020, 202 p.
199. **Max Hecht.** Advances in the Development of a Point-of-Care Mass Spectrometer Test. Tartu, 2020, 168 p.
200. **Ida Rahu.** Bromine formation in inorganic bromide/nitrate mixtures and its application for oxidative aromatic bromination. Tartu, 2020, 116 p.
201. **Sander Ratso**. Electrocatalysis of oxygen reduction on non-precious metal catalysts. Tartu, 2020, 371 p.
202. **Astrid Darnell.** Computational design of anion receptors and evaluation of host-guest binding. Tartu, 2021, 150 p.

203. **Ove Korjus.** The development of ceramic fuel electrode for solid oxide cells. Tartu, 2021, 150 p.
204. **Merit Oss.** Ionization efficiency in electrospray ionization source and its relations to compounds' physico-chemical properties. Tartu, 2021, 124 p.
205. **Madis Lüsi**. Electroreduction of oxygen on nanostructured palladium catalysts. Tartu, 2021, 180 p.
206. **Eliise Tammekivi.** Derivatization and quantitative gas-chromatographic analysis of oils. Tartu, 2021, 122 p.
207. **Simona Selberg.** Development of Small-Molecule Regulators of Epi-transcriptomic Processes. Tartu, 2021, 122 p.
208. **Olivier Etebe Nonga.** Inhibitors and photoluminescent probes for in vitro studies on protein kinases PKA and PIM. Tartu, 2021, 189 p.
209. **Riinu Härmas.** The structure and H2 diffusion in porous carbide-derived carbon particles. Tartu, 2022, 123 p.
210. **Maarja Paalo.** Synthesis and characterization of novel carbon electrodes for high power density electrochemical capacitors. Tartu, 2022, 144 p.
211. **Jinfeng Zhao.** Electrochemical characteristics of Bi(hkl) and micro-meso-porous carbon electrodes in ionic liquid based electrolytes. Tartu, 2022, 134 p.
212. **Alar Heinsaar.** Investigation of oxygen electrode materials for high-temperature solid oxide cells in natural conditions. Tartu, 2022, 120 p.
213. **Jaana Lilloja.** Transition metal and nitrogen doped nanocarbon cathode catalysts for anion exchange membrane fuel cells. Tartu, 2022, 202 p.
214. **Maris-Johanna Tahk.** Novel fluorescence-based methods for illuminating transmembrane signal transduction by G-protein coupled receptors. Tartu, 2022, 200 p.
215. **Eerik Jõgi.** Development and Applications of E. coli Immunosensor. Tartu, 2022, 103 p.
216. **Alo Rüütel.** Design principles of synthetic molecular receptors for anion-selective electrodes. Tartu, 2022, 109 p.
217. **Tanel Sõrmus.** Development of stimuli-responsive and covalent bisubstrate inhibitors of protein kinases. Tartu, 2022, 148 p.
218. **Oleg Artemchuk.** Autotrophic nitrogen removal processes for nutrient removal from sidestream and mainstream wastewater. Tartu, 2022, 115 p.
219. **Andre Leesment.** Quantitative studies of Brønsted acidity in biphasic systems and gas-phase. Tartu, 2023, 83 p.
220. **Meeli Arujõe-Sado.** Structural effects in aza-peptide bond formation reaction. Tartu, 2023, 83 p.
221. **Jonas Mart Linge.** Electrochemical reduction of oxygen on silver-based catalysts. Tartu, 2023, 269 p.
222. **Tõnis Laasfeld.** Integrating Image Analysis and Quantitative Modeling for a Holistic View of GPCR Ligand Binding Dynamics. Tartu, 2023, 226 p.
223. **Ernesto de Jesus Zapata Flores.** Derivatization Reagents used in negative mode electrospray LC-MS. Tartu, 2023, 107 p.

224. **Patrick Teppor.** Obtaining platinum-free oxygen reduction catalysts through biomass valorization: a case study of peat. Tartu, 2023, 161 p.
225. **Peeter Valk.** Methanol Oxidation on Platinum-Rare-Earth Metal Oxide Activated Catalysts. Tartu, 2023, 162 p.
226. **Shidong Chen.** Unravelling prehistoric plant exploitation in eastern Baltic: organic residue analysis of plant-based materials by multi-method approach. Tartu, 2023, 245 p.
227. **Yogesh Kumar.** M-N_4 macrocycle-based catalysts for electrocatalysis of oxygen reduction and oxygen evolution. Tartu, 2023, 224 p.
228. **Kerli Martin.** Recognition of carboxylates by synthetic receptors – from structure-affinity studies to solid-contact anion-selective electrode prototyping. Tartu, 2024, 130 p.
229. **Huy Quí Vinh Nguyen.** Development of Carbon Supported Pt–CeO_2 Catalysts for Proton Exchange Membrane Fuel Cells. Tartu, 2024, 198 p.
230. **Heigo Ers**. Adsorption and Structuring Processes at Single Crystal Electrode – Ionic Liquid Interface – Insights from Simulations and *in situ* Studies. Tartu, 2024, 137 p.
231. **Ritums Cepitis.** Modelling Structural and Geometrical Effects in Carbon Dioxide and Oxygen Electrocatalysis. Tartu, 2024, 99 p.